$f(R)$ Gravity and Spherical Collapse

by

Jun-Qi Guo

M.A., The University of Mississippi, 2008

M.Sc., Huazhong University of Science and Technology, 2004

B.Sc., Yantai Normal University, 2001

Thesis Submitted in Partial Fulfillment
of the Requirements for the Degree of

Doctor of Philosophy

in the
Department of Physics
Faculty of Science

© Jun-Qi Guo 2014
SIMON FRASER UNIVERSITY
Summer 2014

All rights reserved.
However, in accordance with the *Copyright Act of Canada*, this work may be reproduced without authorization under the conditions for "Fair Dealing." Therefore, limited reproduction of this work for the purposes of private study, research, criticism, review and news reporting is likely to be in accordance with the law, particularly if cited appropriately.

APPROVAL

Name: Jun-Qi Guo

Degree: Doctor of Philosophy

Title of Thesis: $f(R)$ Gravity and Spherical Collapse

Examining Committee: Dr. Eldon Emberly, Associate Professor
Chair

Dr. Andrei V. Frolov,
Associate Professor, Senior Supervisor

Dr. Levon Pogosian,
Associate Professor, Supervisor

Dr. Howard Trottier,
Professor, Supervisor

Dr. Andrew DeBenedictis,
Senior Lecturer, Internal Examiner

Dr. Dmitri Pogosyan,
Professor, External Examiner,
Department of Physics, University of Alberta

Date Approved: August 15, 2014

Partial Copyright Licence

The author, whose copyright is declared on the title page of this work, has granted to Simon Fraser University the non-exclusive, royalty-free right to include a digital copy of this thesis, project or extended essay[s] and associated supplemental files ("Work") (title[s] below) in Summit, the Institutional Research Repository at SFU. SFU may also make copies of the Work for purposes of a scholarly or research nature; for users of the SFU Library; or in response to a request from another library, or educational institution, on SFU's own behalf or for one of its users. Distribution may be in any form.

The author has further agreed that SFU may keep more than one copy of the Work for purposes of back-up and security; and that SFU may, without changing the content, translate, if technically possible, the Work to any medium or format for the purpose of preserving the Work and facilitating the exercise of SFU's rights under this licence.

It is understood that copying, publication, or public performance of the Work for commercial purposes shall not be allowed without the author's written permission.

While granting the above uses to SFU, the author retains copyright ownership and moral rights in the Work, and may deal with the copyright in the Work in any way consistent with the terms of this licence, including the right to change the Work for subsequent purposes, including editing and publishing the Work in whole or in part, and licensing the content to other parties as the author may desire.

The author represents and warrants that he/she has the right to grant the rights contained in this licence and that the Work does not, to the best of the author's knowledge, infringe upon anyone's copyright. The author has obtained written copyright permission, where required, for the use of any third-party copyrighted material contained in the Work. The author represents and warrants that the Work is his/her own original work and that he/she has not previously assigned or relinquished the rights conferred in this licence.

Simon Fraser University Library
Burnaby, British Columbia, Canada

revised Fall 2013

Abstract

This thesis studies $f(R)$ model building, cosmological dynamics, Solar System tests of $f(R)$ gravity, and spherical collapse in $f(R)$ gravity.

We apply the running coupling idea to gravity. We describe several well-known $f(R)$ models in a simple way in terms of infrared renormalization group flow. We explore two logarithmic models, produced by the flows. These two models generate a large hierarchy between the Planck scale and the cosmological constant scale.

We study the cosmological dynamics of a range of $f(R)$ models, presenting generic features of phase-space dynamics in $f(R)$ cosmology. New techniques to explore phase-space dynamics are developed. These techniques are very general and can be applied to other similar dynamical systems.

We investigate the Solar System tests of $f(R)$ gravity. The metric is rederived by directly focusing on the equations of motion. The chameleon mechanism in the Jordan frame is considered. These approaches provide a more intuitive understanding of the Solar System tests of $f(R)$ gravity.

We explore spherical scalar collapse in $f(R)$ gravity numerically. We study the dynamics throughout the collapse. Mesh refinement and asymptotic analysis are implemented in the vicinity of the singularity of the formed black hole. The Kasner solution for spherical scalar collapse in $f(R)$ gravity is obtained. These results support the Belinskii-Khalatnikov-Lifshitz conjecture well in the context of black hole physics.

Acknowledgments

First and foremost, I would like to thank my Ph.D. supervisor, Dr. Andrei V. Frolov, for his supervision, encouragement, and insightful comments. I am very grateful to Dr. Levon Pogosian and Prof. Howard Trottier for acting as my supervisory committee members, and for many helpful discussions and pieces of advice. I thank Dr. Andrew DeBenedictis and Dr. Valerio Faraoni for helpful discussions.

I benefited from discussions with Dr. Aaron Berndsen. I thank Daoyan Wang for stimulating conversations and sharing knowledge, especially regarding numerical relativity. I would like to thank Yang Liu, Aaron Plahn, and Shaojie Yin for discussions and proofreading the manuscripts. I am grateful to all the SFU cosmology group members for many discussions.

I am supported by the Pacific Century Graduate Scholarship of the Province of British Columbia and the Special Graduate Entrance Scholarship from Simon Fraser University. I am grateful to the Department of Physics, Simon Fraser University, and its staff for providing the conditions which allowed me to conduct research.

Finally, I thank Jiali Yu for her support and for proofreading the manuscripts. I also thank my little Run-Cheng for the fun and joy he brings to me each day.

Contents

Chapter 1

Introduction

1.1 Background

This thesis will discuss $f(R)$ model building, cosmological dynamics, Solar System tests of $f(R)$ gravity, and spherical collapse in $f(R)$ gravity.

General relativity is a milestone in the exploration of spacetime and the Universe. Modern physics stands on general relativity and quantum mechanics. Since general relativity was developed a century ago, it has proven to be a successful gravitational theory, surviving various tests. It also has had important applications, such as the Global Positioning System. Despite its great achievements, general relativity has some inherent problems, such as nonrenormalizability and singularity problems in black hole physics and in the early Universe. These problems imply that general relativity may not be the final gravitational theory.[125] It is largely believed that gravity and quantum mechanics may be unified. Although a viable quantum theory of gravity is still unavailable, effective field theory makes it possible to describe a quantized gravitational theory with an effective action at the low-curvature scale.[46] This is the theoretical origin of modified gravity theories. Since the foundation of general relativity, a large number of modified gravity theories have been discussed. Some typical ones include scalar-tensor theory,[18,25,26,135] massive gravity,[51,111,112] $f(R)$ theory,[72,125,126] and higher dimensional theory,[8,47,80,95,109,110] etc.

A key application of gravitation is cosmology. Modern cosmology is built on general relativity. However, theoretical and observational explorations in cosmology and astrophysics, such as inflation, the orbital velocities of galaxies in clusters, and cosmic acceleration, also

encourage consideration of new gravitational theories. In Ref.,[125] quantum effects in the early Universe were taken into account. The induced R^2 theory could drive inflation—an early-Universe cosmological acceleration—and is well consistent with observations of Cosmic Microwave Background,[1,83] where R is the Ricci scalar. Cosmic acceleration in the late Universe was observed more than a decade ago via measurements of Type Ia supernovae luminosity.[2,87,103,113,114] Various approaches have been generated to address this issue. The simplest approach is to introduce the ΛCDM model, in which 31.7% of the mass-energy density of the Universe is made up of ordinary matter and dark matter, and the rest is constituted by the cosmological constant, Λ.[2] The cosmological constant has large negative pressure, and the equation of state ($w \equiv P/\rho$) is equal to -1, where P and ρ are the pressure and energy density of the cosmological constant, respectively. It is the large negative pressure that functions as a repulsive force field against regular gravity, thus driving cosmic acceleration. The challenge for the ΛCDM model is that the value of the observed cosmological constant is less than the Planck scale by a factor of 120 orders of magnitude.[29] Another possibility is that the cosmic speed-up might be caused within general relativity by a mysterious cosmic fluid with negative pressure, which is usually referred to as "dark energy". However, the nature of dark energy is still unknown. Alternatively, the acceleration could be due to purely gravitational effects. In other words, one may consider modifying current gravitational theory to produce an effective dark energy. A natural approach is to replace the Ricci scalar, R, in the Einstein-Hilbert action with an arbitrary function of the Ricci scalar,[30,72,126]

$$S = \frac{1}{16\pi G}\int d^4x\sqrt{-g}f(R) + S_m, \tag{1.1}$$

where G is the Newtonian gravitational constant, and S_m is the matter term in the action. [See Refs.[50,123] for reviews of $f(R)$ theory.]

Black hole physics and spherical collapse are important platforms for understanding gravity. A black hole is a spacetime region where gravity is so strong that nothing, including light, can escape from it. Historically, some static solutions for black holes have been obtained analytically. The "no-hair" theorem states that a stationary black hole can be described by only a few parameters.[142] Hawking showed that stationary black holes as the final states of Brans-Dicke collapses are identical to those in general relativity.[69] In Ref.,[12] a novel "no-hair" theorem was proven. In this theorem, the scalar field, surrounding an asymptotically flat, static, spherically symmetric black hole, is assumed to be minimally coupled to gravity, and to have a non-negative energy density. In this case, the black hole

must be a Schwarzschild black hole. This result is also valid if the scalar field has a potential whose global minimum is zero. Possible black hole solutions were explored in scalar-tensor gravity, including $f(R)$ gravity, by Sotiriou and Faraoni. If black holes are isolated from the cosmological background, they can be shown to have a Schwarzschild solution.[124]

Studies of collapse processes can test the conclusions regarding static black holes, and reveal some fascinating features, e.g., critical phenomena.[35] Due to the high nonlinearity of the Einstein field equations, numerical approaches are indispensable. In fact, simulation of dynamics related to black holes is a major topic in numerical relativity. Wave templates obtained from numerical simulations of binary black holes are crucial for gravitational wave detection.

1.2 Running gravitational coupling and $f(R)$ model building

In Chapter 3, we explore $f(R)$ model building using a running gravitational coupling idea.

Renormalization group flow is a core concept in quantum field theory. It is natural to consider this idea in the context of gravity. It has long been hoped that the quantum theory of gravity, at least to some extent, allows description in terms of an effective field theory. When the effective field theory of gravity is asymptotically safe, there should be a sensible ultraviolet-complete description. The idea of the renormalization group flow, which has been very fruitful in high energy physics, is applied to the cosmic acceleration issue. Consequently, attention shifts from the ultraviolet cutoff in the effective action to the lower limit of integration. It is interesting to investigate whether it is theoretically possible to generate an anomalously low scale of a cosmological constant by specific running. In high energy physics, the renormalized coupling parameters run as beta functions of the energy scale. In gravity, the basic scale is set by the curvature of spacetime. Assuming that (classical) gravitational coupling varies with the curvature scalar, one is led to $f(R)$ gravity. Several well-known $f(R)$ modified gravity models have remarkably simple descriptions in terms of the infrared renormalization group flow. We analyze two logarithmic $f(R)$ models produced by the renormalization group flow. These two models generate a large hierarchy between the cosmological acceleration scale and the Planck scale.

1.3 Cosmological dynamics in $f(R)$ gravity

Chapter 4 studies the cosmological viability conditions, phase-space dynamics, and cosmological evolution of $f(R)$ gravity.

Any modified gravity model should fit conventional standard cosmology as well as explain the current cosmic speed-up issue. Specifically, in a viable model, the Universe should have a matter domination epoch in the early Universe to enable the formation of large-scale structure, and it should transit from a matter domination epoch into the current dark energy domination epoch. Moreover, in order to be able to drive the cosmic speed-up, the effective dark energy should have sufficiently large negative pressure, and the effective equation of state should be less than $-1/3$.

The conditions for a viable matter domination epoch and late-time acceleration were derived via an analysis in phase space in Ref.[3] In this thesis, in contrast to most previous works in the literature, we proceed by focusing on the equivalent scalar field description of modified gravity, which we believe is a more intuitive way of treating the problem.

In order to study how physical solutions evolve in $f(R)$ cosmology, we explore the cosmological dynamics of a range of $f(R)$ models. We present generic features of phase-space dynamics in $f(R)$ cosmology. We study the global structure of the phase space in $f(R)$ gravity by compactifying the infinite phase space into a finite space via the Poincaré transformation. On the expansion branch of the phase space, the constraint surface has a repeller and a de Sitter attractor. On the contraction branch, the constraint surface has an attractor and a de Sitter repeller. Generally, the phase currents originate from the repeller and terminate at the corresponding attractor in each space. The trajectories between the repeller and the attractor in the presence of matter density are different from those in the vacuum case. The phase analysis techniques developed in this thesis are very general and can be applied to other similar dynamical systems.

1.4 Solar System tests of $f(R)$ gravity

In Chapter 5, we explore the Solar System tests of $f(R)$ gravity. The metric of the spherical spacetime for the Sun predicted by general relativity matches well with the observations. Therefore, general relativity should be recovered from $f(R)$ gravity in the Solar System. However, if the Sun sits in a vacuum, the scalar field f' will be very light, which will generate

a metric considerably different from the observations. We rederive this result in a simpler way by directly considering the equations of motion for $f(R)$ gravity in the Jordan frame.

General relativity could be recovered via the chameleon mechanism.[84,85] In this mechanism, the scalar field f' is coupled to the matter density of the environment. f' acquires a mass from the coupling, and then is suppressed by the mass, such that $f(R)$ gravity can pass the Solar System tests. The chameleon mechanism is usually implemented in the Einstein frame, in which the condition on the existence of a thin shell is obtained in Refs.[84,85] However, the matter density and the transformed scalar field are coupled in a complex way in the Einstein frame. Note that $f(R)$ gravity is defined in the Jordan frame, and the picture is more intuitive in the Jordan frame, in which the coupling between the matter density and the scalar field f' is much simpler than the form in the Einstein frame. In this thesis, we discuss the chameleon mechanism in the Jordan frame, and also explore the implications of this mechanism for the form of the function $f(R)$.

In addition to analytical methods, a numerical approach also provides an efficient way to study how the scalar field f' behaves in the effective potential. Taking the $R\ln R$ model and the Hu-Sawicki model as examples, we run numerical experiments solving the equation of motion for f' in different configurations. The results verify the arguments for the thin-shell condition obtained in the Jordan frame and the thin-wall approximation condition in the false-vacuum decay scenario, and further clarify whether an $f(R)$ model can avoid the Solar System tests or not.

1.5 Spherical collapse in $f(R)$ gravity

In Chapter 6, we simulate spherical scalar collapse in $f(R)$ gravity, and examine the dynamics near the singularity of the formed black hole.

As astrophysical black holes are expected to come from collapses of matter, studying collapse processes, especially spherical collapses, is an instructive way to explore black hole physics, allowing one to verify the results on stationary black holes as well. We take the Hu-Sawicki model as a sample $f(R)$ model, and take a massless scalar field as the matter field for the collapse. In order to make the formalism less complicated, we transform $f(R)$ theory from the Jordan frame into the Einstein frame. We perform the simulations using the double-null coordinates proposed by Christodoulou.[37] These coordinates have been used widely, because they have the horizon-penetration advantage and allow us to

study the global structure of spacetime. In the vicinity of the singularity of a formed black hole, gravity is super strong. Mesh refinement and asymptotic analysis are employed to examine the dynamics near the singularity.

The results show that a black hole can be formed. Before the collapse, the scalar degree of freedom f' is coupled to a physical scalar field, and general relativity is restored. During the collapse, the major energy of the physical scalar field moves to the center of the sphere. As a result, f' loses the coupling and becomes light, and gravity transits from general relativity to $f(R)$ gravity. Due to strong gravity from the singularity of the formed black hole and the low mass of f', f' will cross the minimum of the potential and approach zero. The dynamical solution for collapse is significantly different from the static solution for a black hole in $f(R)$ theory—it is not a de Sitter-Schwarzschild solution as one might have expected. As the singularity is approached, in the equations of motion for the metric components and scalar fields, the metric terms are dominant over other terms. The terms related to the potential are the least important. The scalar fields are intermediate. f' dominates the competition between f' and the physical scalar field. f' contributes more to the dynamics of the metric components than the physical scalar field does. The physical scalar field accelerates the evolution of f'. The influence of f' on the physical field is considerable. f' tries to suppress the evolution of the physical scalar field. This is a dark energy effect.

Neglecting minor terms, one obtains the reduced equations of motion. These, together with numerical solutions, enable us to obtain the asymptotic solutions for the metric components and f'. The Kasner solution for spherical scalar collapse in $f(R)$ theory is then obtained and is confirmed by numerical results. These results support the Belinskii, Khalatnikov, and Lifshitz conjecture well.

In the Kasner solution obtained for spherical scalar collapse in $f(R)$ theory, the physical scalar field is negligible, and only the metric components and f' are present. Thus, this solution is also the Kasner solution for a single-scalar spherical collapse in general relativity.

This thesis is mainly based on the following papers.

4. J.-Q. Guo, D. Wang, and A. V. Frolov, *"Spherical collapse in $f(R)$ gravity and the Belinskii-Khalatnikov-Lifshitz conjecture,"* arXiv:1312.4625 [gr-qc] (Accepted for publication in Physical Review D)

3. J.-Q. Guo, *"Solar system tests of $f(R)$ gravity,"* International Journal of Modern

Physics D **23**, 1450036 (2014). [arXiv:1306.1853 [astro-ph.CO]]

2. J.-Q. Guo and A. V. Frolov, *"Cosmological dynamics in $f(R)$ gravity,"* Physical Review D **88**, 124036 (2013). [arXiv:1305.7290 [astro-ph.CO]]

1. A. V. Frolov and J.-Q. Guo, *"Small cosmological constant from running gravitational coupling,"* arXiv:1101.4995 [astro-ph.CO]

Chapter 2

Modified gravity theories

General relativity has passed a wide range of experimental tests. However, it has the nonrenormalization and singularity problems. Explorations of cosmology, e.g., inflation and late-Universe cosmic speed-up, also encourage consideration of possible deviations from general relativity. Over the past century, various modified gravity theories have been explored in depth. Roughly, modified gravity theories can be classified into four categories.[31,39]

1. Theories with extra gravitational fields.

   People have considered adding extra scalar fields, vectors, tensors, or even higher rank fields to general relativity.[52,133] Scalar-tensor theories fall into this group. Some other theories, such as $f(R)$ theory and extra-dimension theory, can also be taken as effective scalar-tensor theories.

2. Theories with extra spatial dimensions.

   It is possible to modify general relativity by adding extra spatial dimensions. Representative examples include Kaluza-Klein theory, the Braneworld scenario, and Einstein-Gauss-Bonnet Gravity.

3. Higher derivative theories.

   In general relativity, the terms in the equations of motion are at most second-order derivatives of the metric. On some occasions, when the action for general relativity is modified, the new equations of motion can have derivative terms higher than second

order. Some typical theories in this category include $f(R)$ gravity and Horava-Lifshitz gravity.

4. Theories with non-Christoffel connections.

   In these theories, connection is taken as an independent quantity, rather than as being derived from the metric. We can remove the constraint that the connection must be torsion-free. However, since the torsion itself is a tensor, we cannot distinguish it from other non-gravitational tensor fields. Consequently, these theories are equivalent to general relativity (torsion-free theory) plus tensor fields.

This chapter will briefly describe some typical modified gravity theories, including scalar-tensor theories, $f(R)$ theory, and extra-dimension theories. This chapter is primarily based on Refs.[31,39]

2.1 Scalar-tensor theories

Among the most important modified gravity theories are the scalar-tensor theories, in which a scalar field couples to the Ricci scalar. The action for these theories can be written as[18,135]

$$S = \frac{1}{16\pi G}\int d^4x\sqrt{-g}[f(\phi)R - h(\phi)g^{\mu\nu}\phi_{;\mu}\phi_{;\nu} - V(\phi)] + S_m, \tag{2.1}$$

where $f(\phi)$ and $h(\phi)$ are functions of the scalar field ϕ, $V(\phi)$ is a potential term, and S_m is the matter term in the action.

The Brans-Dicke theory is one of the simplest scalar-tensor theories.[25] Its action can be obtained by setting $f(\phi)$ to ϕ, $V(\phi)$ to zero, and $h(\phi)$ to ω/ϕ, where ω is a coupling constant:

$$S = \frac{1}{16\pi G}\int d^4x\sqrt{-g}\left[\phi R - \frac{\omega}{\phi}g^{\mu\nu}\phi_{;\mu}\phi_{;\nu}\right] + S_m. \tag{2.2}$$

In Brans-Dicke theory, the scalar field is massless. When the coupling ω approaches infinity, the scalar field is frozen, and general relativity is restored. Solar System tests place a stringent constraint on ω as $\omega > 40,000$.[21]

Variations of the action by Eq. (2.2) with respect to $g^{\mu\nu}$ and the scalar ϕ yield the equations of motion for the metric components and scalar field:

$$\phi G_{\mu\nu} + \left[\Box\phi + \frac{1}{2}\frac{\omega}{\phi}(\nabla\phi)^2\right]g_{\mu\nu} - \phi_{;\mu\nu} - \frac{\omega}{\phi}\phi_{;\mu}\phi_{;\nu} = 8\pi G T_{\mu\nu}, \tag{2.3}$$

$$(3+2\omega)\Box\phi = 8\pi G T, \tag{2.4}$$

where $\Box$ is the usual notation for the covariant D'Alembert operator $\Box \equiv \nabla_\alpha \nabla^\alpha$. The scalar-tensor theories are conformally equivalent to general relativity. A conformal transformation

$$\tilde{g}_{\mu\nu} = f(\phi) g_{\mu\nu} \tag{2.5}$$

converts the action described by Eq. (2.1) into[31]

$$S = \frac{1}{16\pi G}\int d^4x\sqrt{-\tilde{g}}\left[\frac{\tilde{R}}{16\pi G} - \frac{1}{2}\tilde{g}^{\mu\nu}\psi_{;\mu}\psi_{;\nu} - U(\psi)\right] + S_m, \tag{2.6}$$

where

$$U(\psi) = \frac{V(\phi)}{(16\pi G)^2 f^2(\phi)}. \tag{2.7}$$

The new field ψ is a function of ϕ. In Brans-Dicke theory, the two quantities are related by

$$\ln\phi = \sqrt{\frac{16\pi G}{3+2\omega}}\psi. \tag{2.8}$$

The original frame with metric $g_{\mu\nu}$ is called the Jordan frame, and the new frame with $\tilde{g}_{\mu\nu}$ is called the Einstein frame. As shown in Eq. (2.6), in the Einstein frame we have general relativity with a scalar field. Variations of the action expressed by Eq. (2.6) with respect to $\tilde{g}^{\mu\nu}$ and ψ produce the equations of motion for the metric components and ψ:

$$\tilde{G}_{\mu\nu} = 8\pi G\left[\tilde{T}^{(M)}_{\mu\nu} + \tilde{T}^{(\psi)}_{\mu\nu}\right], \tag{2.9}$$

$$\Box\psi - \frac{dU}{d\psi} = \frac{1}{2f(\phi)}\frac{df(\phi(\psi))}{d\psi}\tilde{T}^{(M)}, \tag{2.10}$$

where

$$\tilde{T}^{(\psi)}_{\mu\nu} = \partial_\mu\psi\partial_\nu\psi - \tilde{g}_{\mu\nu}\left[\frac{1}{2}\tilde{g}^{\alpha\beta}\partial_\alpha\psi\partial_\beta\psi + U(\psi)\right]. \tag{2.11}$$

In Brans-Dicke theory, Eq. (2.10) becomes

$$\Box\psi - \frac{dU}{d\psi} = \sqrt{\frac{4\pi G}{3+2\omega}}\tilde{T}^{(M)}. \tag{2.12}$$

For more details on scalar-tensor theories, please refer to Refs.[39,59]

2.2 $f(R)$ gravity

There are several reasons to study $f(R)$ gravity. It was found that the quantization of matter fields in an unquantized spacetime can lead to $f(R)$ gravity.[132] Some $f(R)$ models can have improved renormalisation properties.[127] The R^2 Starobinsky model, proposed in 1980, can drive inflation,[125] and remains consistent with the observations.[1,83] Recently, due to the possibility of explaining the late-time cosmological acceleration, $f(R)$ theory has become popular. This section will give the basic formalism of $f(R)$ theory, discuss viability conditions, and introduce some representative $f(R)$ models.

2.2.1 Formalism of $f(R)$ gravity

The action for $f(R)$ gravity reads

$$S = \frac{1}{16\pi G}\int d^4x\sqrt{-g}f(R) + S_m. \tag{2.13}$$

Variation with respect to the metric $g_{\mu\nu}$ in this action yields the field equations for $f(R)$ gravity,

$$f'R_{\mu\nu} - \frac{1}{2}fg_{\mu\nu} - (\nabla_\mu\nabla_\nu - g_{\mu\nu}\Box)\,f' = 8\pi G T_{\mu\nu}, \tag{2.14}$$

where f' denotes the derivative of the function f with respect to its argument R. The trace of Eq. (2.14) is

$$\Box f' = \frac{1}{3}(2f - f'R) + \frac{8\pi G}{3}T, \tag{2.15}$$

where T is the trace of the stress-energy tensor $T_{\mu\nu}$. In general relativity, $f' \equiv 1$ and $\Box f' \equiv 0$. However, $\Box f'$ is generally not zero in $f(R)$ gravity. Therefore, compared to general relativity, there is a scalar degree of freedom, f', in $f(R)$ gravity. Identifying f' with a scalar degree of freedom by

$$\chi \equiv \frac{df}{dR}, \tag{2.16}$$

and defining a potential $U(\chi)$ by

$$U'(\chi) \equiv \frac{dU}{d\chi} = \frac{1}{3}(2f - \chi R), \tag{2.17}$$

one can rewrite Eq. (2.15) as

$$\Box\chi = U'(\chi) + \frac{8\pi G}{3}T. \tag{2.18}$$

In order to operate $f(R)$ gravity, it is instructive to cast the formulation of $f(R)$ gravity into a form similar to that of general relativity. We rewrite Eq. (2.14) as

$$G_{\mu\nu} = 8\pi G \left[T_{\mu\nu} + T_{\mu\nu}^{(\text{eff})} \right], \tag{2.19}$$

where

$$8\pi G T_{\mu\nu}^{(\text{eff})} = \frac{f - f'R}{2} g_{\mu\nu} + (\nabla_\mu \nabla_\nu - g_{\mu\nu}\Box) f' + (1 - f') G_{\mu\nu}. \tag{2.20}$$

$T^{\mu\nu}_{(\text{eff})}$ is the energy-momentum tensor of the effective dark energy. It is guaranteed to be conserved, $T^{\mu\nu}_{(\text{eff});\nu} = 0$. Equation (2.20) reveals the definition of the equation of state for the effective dark energy

$$w_{\text{eff}} \equiv \frac{p_{\text{eff}}}{\rho_{\text{eff}}}, \tag{2.21}$$

where

$$8\pi G \rho_{\text{eff}} = \frac{f'R - f}{2} - 3H\dot{f}' + 3H^2(1 - f'), \tag{2.22}$$

$$8\pi G p_{\text{eff}} = \ddot{f}' + 2H\dot{f}' + \frac{f - f'R}{2} + \left(H^2 - \frac{R}{3} \right)(1 - f'). \tag{2.23}$$

In order for an $f(R)$ model to account for the cosmic speed-up, w_{eff} should be less than $-1/3$.

2.2.2 Viability conditions on $f(R)$ gravity

A viable $f(R)$ model should be stable, mimic a cosmological evolution consistent with observations, and satisfy local tests. This places some viability conditions on $f(R)$ gravity as follows.

1. We require f' to be positive to avoid anti-gravity.

2. The function $f(R)$ should be very close to the curvature scalar R at the high-curvature scale so that a matter domination epoch can exist in the early Universe.

3. The f'' should be positive when the curvature scalar R is greater than the cosmological constant Λ, so that the Dolgov-Kawasaki instability can be avoided and the scalaron f' is nontachyonic.[45] Moreover, the potential $V(\phi)$ should have a minimum such that a dark energy domination stage and a consequent cosmic acceleration can be generated in the late Universe.

4. The Big Bang nucleosynthesis, observations of the Cosmic Microwave Background, and local gravity tests imply that general relativity should be recovered as $R \gg \Lambda$: $f(R) \to R$ and $f' \to 1$. This, together with the requirement of $f'' > 0$, implies that f' should be less than 1.[105]

2.2.3 Jordan frame and Einstein frame

There are second-order derivatives of f' in the energy-momentum tensor of effective dark energy $T^{(\text{eff})}_{\mu\nu}$. On some occasions, e.g., spherical collapse that we discuss in Chapter 6, in order to make the formalism less complicated, we transform $f(R)$ gravity from the current frame, which is usually called the Jordan frame, into the Einstein frame. In the latter, the second-order derivatives of f' are absent in the equations of motion for the metric components. The formalism can be treated as Einstein gravity coupled to two scalar fields. Therefore, we can use some results that have been developed in the numerical relativity community.

Rescaling χ by

$$\kappa\phi \equiv \sqrt{\frac{3}{2}} \ln \chi, \tag{2.24}$$

one obtains the corresponding action of $f(R)$ gravity in the Einstein frame,[50]

$$S_E = \int d^4x\sqrt{-\tilde{g}} \left[\frac{1}{2\kappa^2}\tilde{R} - \frac{1}{2}\tilde{g}^{\mu\nu}\partial_\mu\phi\partial_\nu\phi - V(\phi) \right] + \int d^4x \mathcal{L}_M(\tilde{g}_{\mu\nu}/\chi(\phi), \psi), \tag{2.25}$$

where $\kappa = \sqrt{8\pi G}$, $\tilde{g}_{\mu\nu} = \chi \cdot g_{\mu\nu}$, $V(\phi) \equiv (\chi R - f)/(2\kappa^2\chi^2)$, ψ is a matter field, and a tilde denotes that the quantities are in the Einstein frame. The Einstein field equations are

$$\tilde{G}_{\mu\nu} = \kappa^2 \left[\tilde{T}^{(\phi)}_{\mu\nu} + \tilde{T}^{(M)}_{\mu\nu} \right], \tag{2.26}$$

where

$$\tilde{T}^{(\phi)}_{\mu\nu} = \partial_\mu\phi\partial_\nu\phi - \tilde{g}_{\mu\nu} \left[\frac{1}{2}\tilde{g}^{\alpha\beta}\partial_\alpha\phi\partial_\beta\phi + V(\phi) \right], \tag{2.27}$$

$$\tilde{T}^{(M)}_{\mu\nu} = \frac{T^{(M)}_{\mu\nu}}{\chi}. \tag{2.28}$$

$T^{(M)}_{\mu\nu}$ is the ordinary energy-momentum tensor of the physical matter field in terms of $g_{\mu\nu}$ in the Jordan frame. In Chapter 6, we take a massless scalar field ψ as the matter field for

the collapse. Its energy-momentum tensor in the Einstein frame is

$$\tilde{T}^{(M)}_{\mu\nu} = \tilde{T}^{(\psi)}_{\mu\nu} = \frac{1}{\chi}\left(\partial_\mu\psi\partial_\nu\psi - \frac{1}{2}g_{\mu\nu}g^{\alpha\beta}\partial_\alpha\psi\partial_\beta\psi\right) = \frac{1}{\chi}\left(\partial_\mu\psi\partial_\nu\psi - \frac{1}{2}\tilde{g}_{\mu\nu}\tilde{g}^{\alpha\beta}\partial_\alpha\psi\partial_\beta\psi\right), \tag{2.29}$$

which gives

$$\tilde{T}^{(M)} = \tilde{T}^{(\psi)} \equiv \tilde{g}^{\mu\nu}\tilde{T}^{(\psi)}_{\mu\nu} = -\frac{\tilde{g}^{\alpha\beta}\partial_\alpha\psi\partial_\beta\psi}{\chi}.$$

The equations of motion for ϕ and ψ can be derived from Lagrange equations as

$$\tilde{\Box}\phi - V'(\phi) + \kappa Q\tilde{T}^{(M)} = 0, \tag{2.30}$$

$$\tilde{\Box}\psi - \sqrt{\frac{2}{3}}\,\kappa\tilde{g}^{\mu\nu}\partial_\mu\phi\partial_\nu\psi = 0, \tag{2.31}$$

where $Q \equiv -\chi_{,\phi}/(2\kappa\chi) = -1/\sqrt{6}$. In the Einstein frame, the potential for ϕ is written as

$$V(\phi) = \frac{\chi R - f}{2\kappa^2\chi^2}. \tag{2.32}$$

Then we have

$$V'(\phi) = \frac{dV}{d\chi}\cdot\frac{d\chi}{d\phi} = \frac{1}{\sqrt{6}}\frac{2f - \chi R}{\kappa\chi^2}. \tag{2.33}$$

2.2.4 Inflationary $f(R)$ models

Many $f(R)$ models have been proposed and studied. Basically, there are two types of $f(R)$ models. One type of model modifies general relativity at the high-curvature scale, and can be used to drive inflation. The other type modifies general relativity at the low-curvature scale, and is considered to explain the late-time cosmological acceleration.

In the first category, the R^2 Starobinsky model, proposed in Ref.,[125] is the best known. In this scenario, inflation is driven by quantum corrections to vacuum. Vilenkin provided a detailed review of this model in Ref.[134] Based on this reference, we give a brief description of this model below.

The R^2 Starobinsky model is obtained in semiclassical general relativity:

$$R_{\mu\nu} - \frac{1}{2}g_{\mu\nu}R = 8\pi G < T_{\mu\nu} >, \tag{2.34}$$

where $< T_{\mu\nu} >$ is the expectation value of the quantum contributions from the process of regularization.[22,27,44] We consider the Friedmann-Robertson-Walker metric

$$ds^2 = -dt^2 + a^2(t)d\sigma_K^2, \tag{2.35}$$

where $K = 1,\ 0,\ -1$ corresponds to a closed, flat and open Friedmann-Robertson-Walker model, respectively. In the case of free, massless, conformally invariant fields, the quantum corrections can be expressed as follows:

$$< T_{\mu\nu} >= k_1 H^{(1)}_{\mu\nu} + k_2 H^{(2)}_{\mu\nu}, \tag{2.36}$$

where k_1 and k_2 are numerical coefficients, and

$$H^{(1)}_{\mu\nu} = 2R_{;\mu\nu} - 2g_{\mu\nu}R^{;\sigma}_{;\sigma} + 2RR_{\mu\nu} - \frac{1}{2}g_{\mu\nu}R^2, \tag{2.37}$$

$$H^{(2)}_{\mu\nu} = R^{\sigma}_{\mu}R_{\nu\sigma} - \frac{2}{3}RR_{\mu\nu} - \frac{1}{2}g_{\mu\nu}R^{\sigma\tau}R_{\sigma\tau} + \frac{1}{4}g_{\mu\nu}R^2. \tag{2.38}$$

The Starobinsky model in a de Sitter space with $Mm_{\mathsf{pl}} \ll H_0$ is

$$f(R) = R + \frac{R^2}{6M^2 m^2_{\mathsf{pl}}} + \frac{R^2}{R_0}\ln\frac{R}{R_0}, \tag{2.39}$$

where $R_0 = 12H_0^2$, $H_0 = (8\pi k_2 G)^{-1/2}$, $M = (6k_1)^{-1/2}$, and m_{pl} is the Planck mass.

Equation (2.34) with the energy-momentum tensor defined by Eq. (2.36) has a de Sitter solution. Neglecting the trivial solution $R = 0$, we have $R = 12H_0^2$. The corresponding de Sitter solutions are

$$\begin{aligned} a(t) &= H_0^{-1}\cosh(H_0 t), \quad && \text{for } K = 1, \\ a(t) &= a_0 \exp(H_0 t), && \text{for } K = 0, \\ a(t) &= H_0^{-1}\sinh(H_0 t), && \text{for } K = -1. \end{aligned} \tag{2.40}$$

These solutions provide an inflationary stage driven entirely by quantum corrections to Einstein's equations. At the inflationary stage, the logarithmic term in Eq. (2.39) can be neglected, and we have the conventional form

$$f(R) = R + \frac{R^2}{6M^2 m^2_{\mathsf{pl}}}. \tag{2.41}$$

Normalization of the Cosmic Microwave Background anisotropies shows that $M \approx 10^{-5}$.[1,83]

2.2.5 Dark energy $f(R)$ models

Here, we list two typical viable dark energy $f(R)$ models. One is the Starobinsky model,[126]

$$f(R) = R + CR_0 \left[\left(1 + \frac{R^2}{R_0^2} \right)^{-n} - 1 \right], \tag{2.42}$$

where C and n are positive parameters, and R_0 has the same order of magnitude as the currently observed effective cosmological constant. In this model, $f(R = 0) = 0$. $R^\mu_\nu = 0$ is always a solution to Eq. (2.19). However, $f''(R = 0)$ is negative. Therefore, the flat spacetime is unstable. For $R \gg R_0$, $f(R) \approx R - CR_0$, and one obtains the ΛCDM model.

The other typical viable $f(R)$ model is the Hu-Sawicki $f(R)$ model. This model reads[72]

$$f(R) = R - R_0 \frac{C_1 R^n}{C_2 R^n + R_0^n}, \tag{2.43}$$

where n is a positive parameter, C_1 and C_2 are dimensionless parameters, $R_0 = 8\pi G\bar{\rho}_0/3$, and $\bar{\rho}_0$ is the average matter density of the current Universe. It is noticeable that the $n = 1$ case of the Starobinsky model and the $n = 2$ case of the Hu-Sawicki model are essentially the same. We consider one of the simplest versions of the Hu-Sawicki model, i.e., $n = 1$,

$$f(R) = R - \frac{CR_0 R}{R + R_0}. \tag{2.44}$$

In this model,

$$f' = 1 - \frac{CR_0^2}{(R + R_0)^2}, \tag{2.45}$$

$$R = R_0 \left[\sqrt{\frac{C}{1 - f'}} - 1 \right], \tag{2.46}$$

$$V(\phi) = \frac{CR_0 R^2}{2\kappa^2 f'^2 (R + R_0)^2}, \tag{2.47}$$

$$V'(\phi) = \frac{R^3}{\sqrt{6}\kappa f'^2 (R + R_0)^2} \left[1 + (1 - C)\frac{R_0}{R} \left(2 + \frac{R_0}{R} \right) \right]. \tag{2.48}$$

Equations (2.45) and (2.48) show that as long as the matter density is much greater than R_0, the curvature R will trace the matter density well, f' will be close to 1 but not cross 1, and general relativity will be restored. As implied in Eq. (2.48), in order to make sure that the de Sitter curvature, for which $V'(\phi) = 0$, has a positive value, the parameter C needs to be greater than 1.

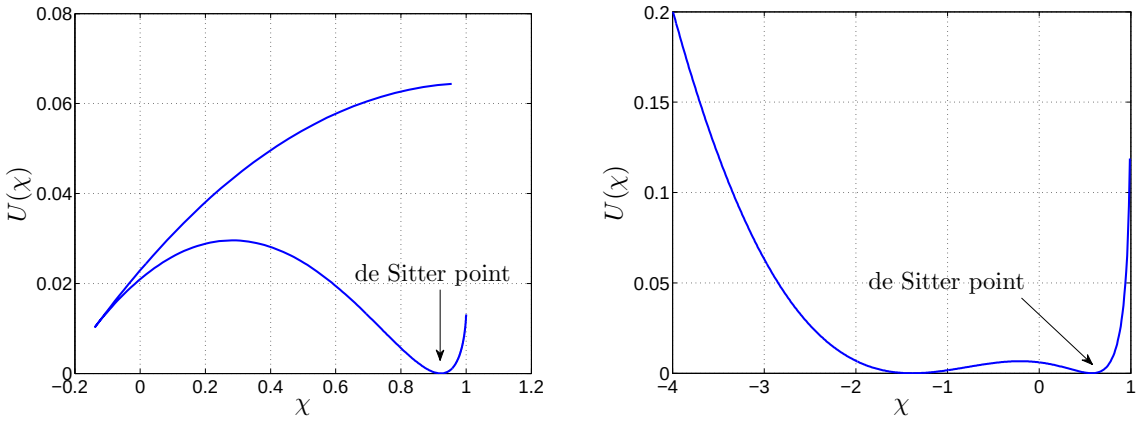

(a) Potential for Starobinsky model

(b) Potential for Hu-Sawicki model

Figure 2.1: Potentials for two dark energy $f(R)$ models. (a) Potential for the Starobinsky model, described by (2.42), with $C = 1.1$, $n = 2$, and $R_0 = 5 \times 10^{-6}$. (b) Potential for the Hu-Sawicki model, expressed by (2.44), with $C = 1.2$ and $R_0 = 5 \times 10^{-6}$.

The features of $f(R)$ gravity are largely defined by the shape of the potential. Therefore, we plot the potentials for the Starobinsky and Hu-Sawicki models in Fig. 2.1.

2.3 Higher dimensional gravity theories

Higher dimensional theories are another set of popular alternative modified gravity theories. Major examples include Kaluza-Klein theory, Randall-Sundrum gravity, Dvali-Gabadadze-Porrati gravity, and Einstein-Gauss-Bonnet gravity.

Historically, Kaluza-Klein theory was proposed toward unifying gravity with electrodynamics.[80,86] In this theory, general relativity is extended to a five-dimensional spacetime. The fourth spatial dimension is curled up in a circle of very small radius. The equations are separated into three sets. One set is equivalent to the Einstein field equations, another set to Maxwell's equations for the electromagnetic field, and the third set is for an extra field known as the dilaton. By implementing a harmonic expansion of all fields along the extra dimension, one obtains an effective $3 + 1$ dimensional theory. When the extra dimensions have been stabilized, the late-time dynamics of Kaluza-Klein theory can be understood as a four-dimensional effective theory.

In the Kaluza-Klein scenario, the extra dimensions are small and compact. However, in the Braneworld scenario, the extra dimensions can be much larger. The Standard Model

fields are confined to stay on a $3+1$ dimensional hypersurface embedded in some higher dimensional spacetime. The $3+1$ dimensional hypersurface and the higher dimensional spacetime are usually called brane and bulk, respectively. Some typical Braneworld models include the ADD model (named after Arkani-Hamed, Dimopoulos, and Dvali[4]), Randall-Sundrum gravity,[109,110] and Dvali-Gabadadze-Porrati gravity.[47]

Einstein-Gauss-Bonnet gravity is another interesting modified gravity theory.[95] In this theory, the Gauss-Bonnet term is added to the action of general relativity:

$$S = \frac{1}{16\pi G}\int d^D x\sqrt{-g}R + \alpha\mathcal{G} + S_m, \tag{2.49}$$

where $\mathcal{G}$ is the Gauss-Bonnet term,

$$\mathcal{G} = R^2 - 4R^{\mu\nu}R_{\mu\nu} + R^{\mu\nu\rho\sigma}R_{\mu\nu\rho\sigma}. \tag{2.50}$$

More generally, one can replace $\mathcal{G}$ by a function of $\mathcal{G}$. The Gauss-Bonnet term makes contributions only in $4+1$ dimensions or greater. In $3+1$ dimensions and lower, it becomes a topological surface term. Consequently, there are no additional dynamical degrees of freedom.

In summary, in this chapter, we provide a general picture of modified gravity theories. The rest of this thesis will focus on $f(R)$ gravity. It will discuss $f(R)$ model building, cosmological dynamics, Solar System tests of $f(R)$ gravity, and spherical collapse in $f(R)$ gravity.

Chapter 3

Running gravitational coupling

In this chapter, we study how to construct viable $f(R)$ gravity models. We apply the renormalization group flow idea to gravity in order to address the cosmological acceleration issue. Several well-known $f(R)$ modified gravity models have remarkably simple descriptions in terms of the infrared renormalization group flow. We discuss two logarithmic $f(R)$ models generated by the flows. This chapter is mainly based on Ref.[58]

3.1 Running gravitational coupling and $f(R)$ models

Renormalization group flow plays a crucial role in quantum field theory and statistical physics. It shows how a physical system changes as viewed at different distance scales. In quantum field theory, the renormalization group flow comes from removing the infinities of the correlation functions. Under the renormalization conditions, the coupling constant λ runs with respect to the renormalization scale M as a beta function:

$$\beta \equiv \frac{d\lambda}{d\ln M}. \tag{3.1}$$

In statistical physics, the renormalization group was introduced to explain the universality properties of continuous phase transitions.[104, 146]

Given the great successes of the renormalization group flow in quantum field theory and statistical physics, it is natural to consider this idea in the context of gravity. It has long been hoped that the quantum theory of gravity, at least in some limit, allows description in terms of an effective field theory.[140, 141] The usual Einstein-Hilbert action is merely the first

two terms of an effective action

$$S[\lambda] = \int \left\{ \sum_{n=0}^{\infty} \lambda^{4-2n} g^{(n)}(\lambda)\, \mathcal{R}^{(n)} + \dots \right\} \sqrt{-g}\, d^4x, \tag{3.2}$$

expanded in local n-th order curvature invariants $\mathcal{R}^{(n)}$, where λ is the ultraviolet cutoff. If the effective field theory of gravity is asymptotically safe, this would allow a sensible ultraviolet-complete description.[98,102] On the other hand, the observations of current cosmic acceleration indicate a tiny but nonvanishing cosmological constant. This introduces a hierarchy problem between the (infrared) cosmological acceleration scale and the (ultraviolet) Planck scale.[101,139]

It is interesting to investigate whether it is theoretically possible to generate an anomalously low scale of cosmological constant by specific gravitational coupling running. We apply the renormalization group flow idea, which has been very fruitful in high energy physics, to the cosmic acceleration issue. This obviously shifts our attention from the ultraviolet cutoff in the effective action (3.2) to the lower energy scale. In high energy physics, the renormalized coupling parameters run as beta functions of the energy scale. In gravity, the basic scale is set by the curvature of the spacetime. Assuming that the (classical) gravitational coupling varies with the curvature scalar, R, one is led to $f(R)$ gravity.

Considering that Newton's gravitational constant runs with the Ricci scalar, we introduce a dimensionless coupling α,

$$8\pi G = \alpha m_{\mathsf{pl}}^{-2}, \tag{3.3}$$

where m_{pl} is the Planck mass. If the renormalization group flow is autonomous, the running of the dimensionless coupling α can be described by a beta function,

$$\mu \frac{d\alpha}{d\mu} = \beta(\alpha), \tag{3.4}$$

where $\mu \equiv R/R_0$, and R_0 is a positive constant parameter. The integration of the above equation yields an α as a function of the curvature scalar. Then, by replacing $8\pi G$ in the Lagrangian density of general relativity $\mathcal{L}_{GR} = R/(16\pi G)$ with $\alpha m_{\mathsf{pl}}^{-2}$ [refer to Eq. (3.3)], one obtains $f(R)$ gravity with the Lagrangian density

$$\mathcal{L}_{f(R)} = \frac{m_{\mathsf{pl}}^2}{2} \frac{R}{\alpha}. \tag{3.5}$$

For a viable $f(R)$ model, f' has to be positive to avoid ghosts,[99] and f'' has to be positive to avoid the Dolgov-Kawasaki instability.[45] These conditions can be expressed in

terms of the flow equation quantities:

$$f' = \frac{\alpha - \beta}{\alpha^2} > 0, \tag{3.6}$$

$$Rf'' = -\left(1 - 2\frac{\beta}{\alpha} + \frac{d\beta}{d\alpha}\right)\frac{\beta}{\alpha^2} > 0. \tag{3.7}$$

Moreover, with Eq. (2.17), an $f(R)$ model would have a vacuum (anti-) de Sitter solution if

$$2f - f'R = \frac{\alpha + \beta}{\alpha^2}R = 0. \tag{3.8}$$

At the de Sitter point, $\beta = -\alpha < 0$. Then Eq. (3.7) implies that the de Sitter point is unstable if $d\beta/d\alpha$ is less than -3. In order to have an asymptotically safe theory with an effective cosmological constant, the renormalization group flow should connect the $\alpha + \beta = 0$ line at the infrared scale to the $\beta = 0$ fixed point at the ultraviolet scale.

3.2 Power-law $f(R)$ models

With the arguments in the above section, the power-law corrections to the Einstein-Hilbert action

$$f(R) = R\left[1 + \lambda\left(\frac{R}{R_0}\right)^n\right] \tag{3.9}$$

can be generated by an autonomous flow,

$$\beta(\alpha) = n\alpha(\alpha - 1), \tag{3.10}$$

with

$$\alpha \equiv \frac{R}{f(R)} = \frac{1}{1 + \lambda\mu^n}. \tag{3.11}$$

The solutions to $\beta(\alpha) = 0$ are called fixed points of the autonomous flow.

When $n = -1$, 1, and -2, one can achieve general relativity with a cosmological constant, the R^2 Starobinsky model,[125] and the $1/R$ model,[30] respectively. The corresponding flows are plotted in Fig. 3.1(a).

Combining Eqs. (3.4), (3.10), and (3.11), one obtains the description of β as a function of the scale μ,

$$\beta = -\frac{n\lambda\mu^n}{(1 + \lambda\mu^n)^2}. \tag{3.12}$$

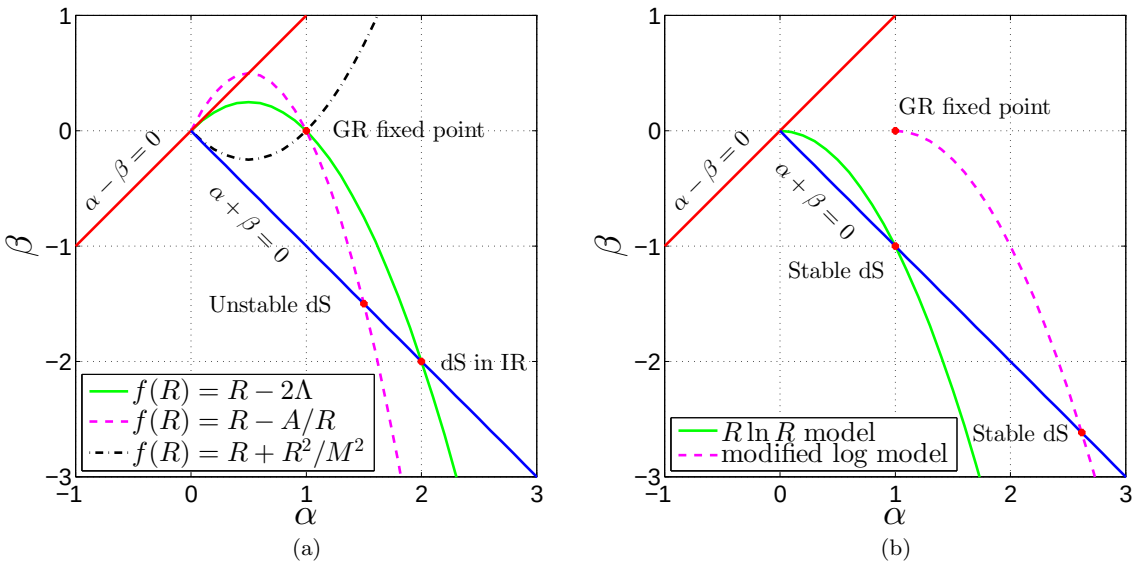

Figure 3.1: Renormalization group flows for some $f(R)$ models. (a) Power-law $f(R)$ models. (b) Two logarithmic models. The $R\ln R$ and modified logarithmic models are described by Eqs. (3.15) or (3.17), and (3.25), respectively.

At the high-curvature scale, where $\mu \gg 1$, we have

$$\beta \approx -\frac{n}{\lambda \mu^n}. \tag{3.13}$$

Therefore, the separation of the orders of magnitude for the beta function is comparable to that for curvature. In other words, in the power-law $f(R)$ models, a big gap in the beta function corresponds to a big gap in curvature between the Planck scale and the local environment on Earth. This is also true for some other $f(R)$ models (e.g., the Hu-Sawicki model[72]). However, as will be discussed below, a reasonable gap in the beta function can make a big hierarchy of curvature when the linear term in the beta function is absent.

3.3 The $R\ln R$ model

We consider a quadratic beta function,

$$\beta = -\alpha^2, \tag{3.14}$$

which leads to the following model with interesting features.

$$f(R) = \frac{R}{\alpha_0}\left(1+\alpha_0 \ln\frac{R}{R_0}\right), \tag{3.15}$$

where α_0 is a dimensionless constant parameter. In this model, the coupling constant runs as

$$\alpha = \frac{\alpha_0}{1 + \alpha_0 \ln \frac{R}{R_0}}. \tag{3.16}$$

Due to the logarithmic relation between α and R, a small change in the orders of magnitude for α can generate a large hierarchy for R. As discussed below, this property can be used to generate small numbers to address the hierarchy problem, which is related to the big gap between the Planck scale and the cosmological constant scale.

For ease of operation, one can absorb the constant α_0 in the denominator of Eq. (3.15) into the definition of the Planck mass m_{pl}, and rewrite Eq. (3.15) as

$$f(R) = R\left(1 + \alpha_0 \ln \frac{R}{R_0}\right). \tag{3.17}$$

Therefore, in this model, the scalar degree of freedom is

$$\phi \equiv f' = 1 + \alpha_0 + \alpha_0 \ln \frac{R}{R_0}, \tag{3.18}$$

and the potential is determined by

$$V'(\phi) = \frac{2f - f'R}{3} = \frac{1}{3}\Lambda e^{\frac{\phi}{\alpha_0} - 2}(\phi - 2\alpha_0). \tag{3.19}$$

Then, at the de Sitter point where $V'(\phi) = 0$, ϕ is equal to $2\alpha_0$. The corresponding curvature, which is usually called the de Sitter curvature,

$$\Lambda \equiv R_0 e^{-\frac{1}{\alpha_0} + 1}, \tag{3.20}$$

is exponentially suppressed compared to R_0. f' has to be positive to avoid ghosts[99] and f'' has to be positive to avoid the Dolgov-Kawasaki instability.[45] For the $R \ln R$ model, given Eqs. (3.18) and (3.20), the first requirement that f' be positive can be satisfied as long as the Ricci scalar is not too much less than the de Sitter curvature. For the $R \ln R$ model, f'' is equal to α_0/R and α_0 is a positive constant, and we only consider the positive Ricci scalar. Then, the second requirement of f'' being positive can be easily met.

In dark energy $f(R)$ gravity, some $f(R)$ models have a singularity problem, while the $R \ln R$ model is free from this problem. For some $f(R)$ models, such as the Starobinsky model and the Hu-Sawicki model described by Eqs. (2.42) and (2.43), respectively, ϕ asymptotes to 1 as the Ricci scalar goes to infinity. Note that the equation of motion for ϕ is described by Eq. (2.18):

$$\Box\phi = V'(\phi) + \frac{8\pi G}{3}T. \tag{3.21}$$

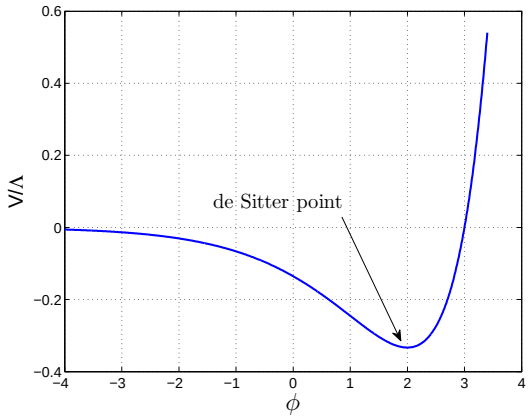

Figure 3.2: The potential $V(\phi)$ as in Eq. (3.22) for the $R\ln R$ model with $\alpha_0 = R_0 = 1$.

As shown in Fig. 2.1, for the Starobinsky model and the Hu-Sawicki model, the height of the potential barrier, defined by $\Delta V \equiv V(\phi \to 1) - V(\phi_{\rm dS})$, is finite, where $\phi_{\rm dS}$ is the de Sitter value for ϕ. Therefore, a perturbation from the matter force, $8\pi GT/3$, can easily push the field ϕ to the barrier of $V(\phi)$, and then the Ricci scalar becomes singular.[57] However, the $R\ln R$ model is free of this singularity problem. Integrating Eq. (3.19), we obtain the potential

$$V(\phi) = \frac{1}{3}\alpha_0\Lambda e^{\frac{\phi}{\alpha_0}-2}(\phi - 3\alpha_0), \tag{3.22}$$

which has an exponential wall, avoiding the singularity problem. The potential is shown in Fig. 3.2.

For this model, with Eq. (3.18), the function $f(R)$ expressed by Eq. (3.17) can be rewritten as

$$f(R) = R(\phi - \alpha_0). \tag{3.23}$$

When the $R\ln R$ gravity is reduced to general relativity, ϕ evolves slowly. Then, from Eq. (2.15), which describes the dynamics of ϕ, one obtains

$$\phi \approx 2\alpha_0 + \alpha_0 W(X), \tag{3.24}$$

where $X = 8\pi G\rho/\Lambda$ and $W(X)$ is the Lambert W function. The basic properties of $W(X)$ with positive X are described in Appendix 3.6. Equations (3.23) and (3.24) show that when general relativity is restored, we have

$$\alpha_0 \approx \frac{1}{W(X)} \ll 1.$$

When X is much greater than 1, $W(X)$ is approximately equal to $\ln(X)$. This feature, together with Eq. (3.24), implies that the field ϕ logarithmically runs depending on X, when X is much greater than 1. Therefore, this model is reduced to general relativity only for a certain period of curvature or matter density. The less α_0 is, the longer the general relativity restoration period is. This is quite different from some other models, such as the Hu-Sawicki model[72] and the Starobinsky model,[126] in which $f(R)$ gravity goes to general relativity once ρ_m is above the cosmological constant scale. On the other hand, in order for the $R\ln R$ model to have a sensible cosmic acceleration in the late Universe, the de Sitter curvature–and hence α_0–cannot be too small [see Eq. (3.20)]. Consequently, an appropriate value for α_0 needs to be chosen to reconcile the tension between the requirements in the early and the late Universe.

In Chapters 4 and 5, we will explore the cosmological dynamics and Solar System tests of this model in detail.

3.4 A modified logarithmic model

3.4.1 A modified logarithmic model

As shown in Fig. 3.1(b), in the $R\ln R$ model, at the high-curvature scale, the effective gravitational constant asymptotes to zero. As a result, the modification term causes significant deviation from general relativity at the high-curvature scale, and this model has difficulties in developing a matter domination stage and passing the Solar System tests. This problem is alleviated in the modified logarithmic model

$$f(R) = R\frac{a+\ln(R/R_0)}{1+\ln(R/R_0)} = R\left[1-\frac{b}{1+\ln(R/R_0)}\right], \tag{3.25}$$

where $b = 1-a$. The corresponding flow of this model is

$$\beta = -k(\alpha-\alpha_*)^2, \tag{3.26}$$

where k is a parameter, and α_* is a fixed point. The flow is shown in Fig. 3.1(b). The flow approaches the nonzero fixed point $\alpha = \alpha_*$ at the high-curvature scale. Consequently, compared to the $R\ln R$ model, this model can generate a more favorable cosmological evolution in the early Universe stage.

In this model,

$$f' = 1 - \frac{b}{1 + \ln(R/R_0)} + \frac{b}{[1 + \ln(R/R_0)]^2}. \tag{3.27}$$

Equation (3.27) implies that f'' and $V''(\phi)[= (f' - f''R)/3f'']$ will change signs at some point, and the potential $V(\phi)$ is folded at that point, as shown in Fig. 3.3. When b is small, the potential $V(\phi)$ can be folded before ϕ reaches the de Sitter point, as shown in Fig. 3.3(a). The model is unstable at places where $f'' < 0$ and $V''(\phi) < 0$. When b is larger, the folding point of $V(\phi)$ can be shifted to the left side of the de Sitter point, as shown in Fig. 3.3(b).

In this modified logarithmic model, $f(R)$ gravity is reduced to general relativity at the high-curvature scale. However, because of the "soft" logarithmic dependence in the function $f(R)$, this model is reduced to general relativity at the high-curvature scale slowly, and still does not have a fully matter-dominated epoch in the early Universe.[58]

3.4.2 Discussions

In the last subsection, we considered a modified logarithmic model, described by Eq. (3.25). In order to explore other possibilities, one can generalize the function of Eq. (3.25) as follows:

$$f(R) = R\left[1 - \frac{b}{1 + A(R/R_0)}\right], \tag{3.28}$$

where $A(R/R_0)$ is a function of R/R_0. One may consider a polynomial case as expressed by

$$f(R) = R\left[1 - \frac{b}{1 + (R/R_0)^n}\right]. \tag{3.29}$$

When $n = 1$, this model happens to be the simplest format of the Hu-Sawicki model.[72] The complete format of the Hu-Sawicki model is described as follows:

$$f(R) = R - \frac{b}{c + (R_0/R)^n} = R - \frac{b(R/R_0)^n}{c(R/R_0)^n + 1}, \tag{3.30}$$

where n is a positive integer number. For the model expressed by Eq. (3.29), in the case of $n = 1$, there is

$$f' = 1 - \frac{b}{(1 + R/R_0)^2}. \tag{3.31}$$

Therefore, f'' will not be zero, and $V(\phi)$ does not have a folding point from the high-curvature scale ($R \gg \Lambda$) to the low-curvature scale ($R \sim \Lambda$), as is shown in Fig. 3.3(c).

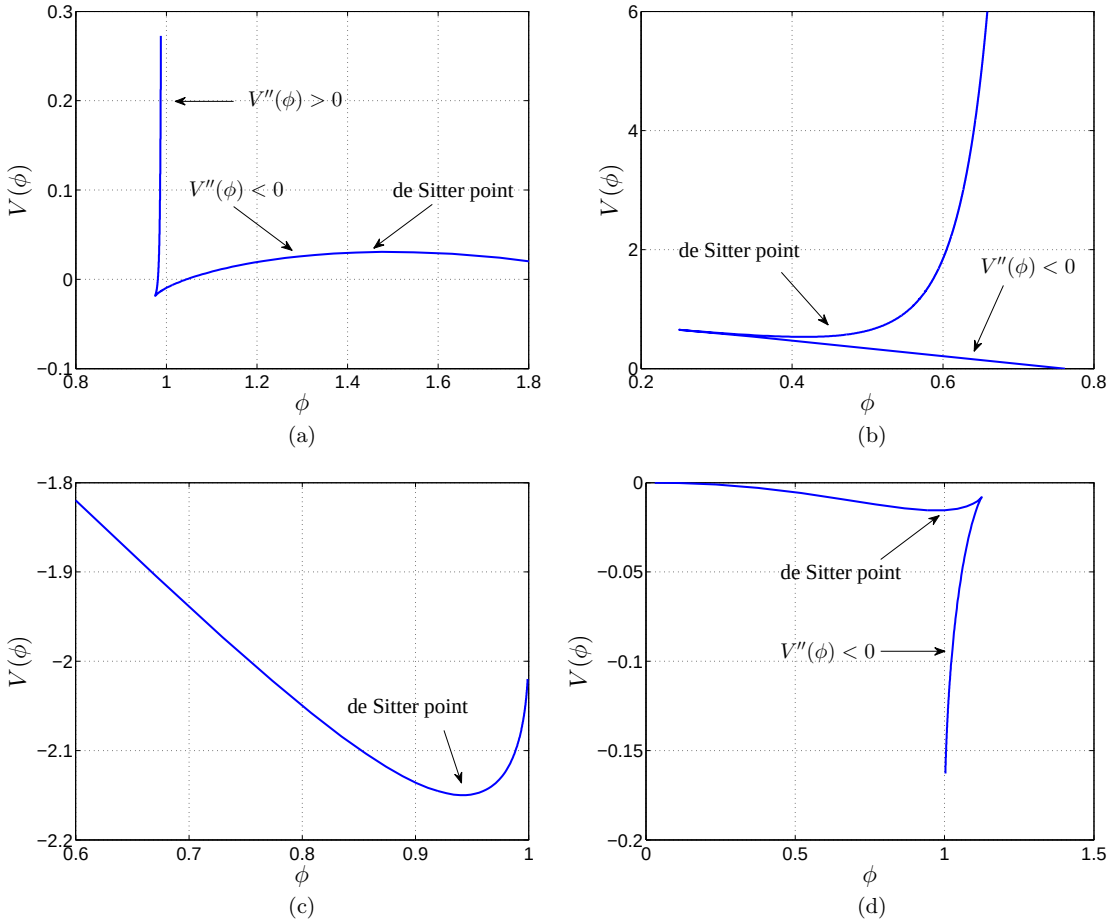

Figure 3.3: Potentials for some $f(R)$ models. (a) The potential for the modified logarithmic model of Eq. (3.25) with $b = 0.1$ and $R_0 = 1$. (b) The potential for the modified logarithmic model of Eq. (3.25) with $b = 3$ and $R_0 = 1$. (c) The potential for the polynomial model of Eq. (3.29) with $n = R_0 = 1$ and $b = 5$. (d) The potential for the polynomial model of Eq. (3.29) with $n = 2$ and $b = R_0 = 1$.

However, as long as $n > 1$, f'' will include more than one term of R with different signs, $V(\phi)$ will have a folding point, and $V''(\phi)$ will switch signs at the folding point. As illustrated in Fig. 3.3(d), in this case, for some period of ϕ from the high to the low-curvature scales, $V''(\phi)$ is negative and, consequently, the scalaron f' is tachyonic. One exponential case, as described by Eq. (3.32), has a similar problem.

$$f(R) = R\left[1 - \frac{b}{1 + \exp(R/R_0)}\right]. \tag{3.32}$$

In this class of $f(R)$ models described by Eq. (3.28), there are functions of R in both the numerator and the denominator of the modification term, which results in $V(\phi)$ having a folding point. At that folding point, $V''(\phi)$ switches signs, and the scalaron f' is tachyonic at places where $V''(\phi) < 0$. To avoid this problem, one may replace the function of R in the numerator with a constant, and obtain ΛCDM-like models. In these models, the function $f(R)$ is approximately equal to $(R - 2\Lambda)$ at the high-curvature scale, and the modification term will be the decisive term in the late cosmological evolution.

3.5 Conclusions

We discussed the renormalization group flow idea in the context of gravity. A cosmic acceleration could be generated by this idea. An $R \ln R$ model, produced by the renormalization group flow, has the exponential hierarchy between the effective cosmological constant scale and UV scale. On the other hand, in this model, the modification term causes significant deviation from general relativity at the high-curvature scale. Consequently, it is hard for this model to have a matter domination stage in the early Universe and to avoid the Solar System tests. This problem is alleviated considerably in a modified logarithmic model (3.25). However, because of the "soft" logarithmic dependence in the function $f(R)$, this model still does not have a fully matter-dominated epoch in the early Universe.

3.6 Appendix: Lambert W function

The Lambert W function is defined[42] by

$$Y = W(Y)e^{W(Y)}, \tag{3.33}$$

where Y can be a negative or a complex number. In this thesis, we only consider the case of $Y > 0$. When $0 < Y \ll 1$, $W(Y) \ll 1$, $e^{W(Y)} \to 1$, then $W(Y) \approx Y$. When $Y \gg 1$, $W(Y) \gg 1$, then $\ln Y \approx W$. Concisely,

$$W(Y) \approx \begin{cases} Y & \text{if } 0 < Y \ll 1, \\ \ln Y & \text{if } Y \gg 1. \end{cases} \tag{3.34}$$

Chapter 4

Cosmological dynamics in $f(R)$ gravity

In this chapter, we study the cosmological viability conditions, phase-space dynamics, and cosmological evolution of $f(R)$ gravity. In contrast to most previous works in the literature, which analyzed the background dynamics of $f(R)$ gravity by means of a dynamical system, we proceed by focusing on the equivalent scalar field description of the theory, which we believe is a more intuitive way of treating the problem. In order to study how the physical solutions evolve in $f(R)$ cosmology, we explore the cosmological dynamics of a range of $f(R)$ models. We present generic features of the phase-space dynamics in $f(R)$ cosmology. We study the global structure of the phase space in $f(R)$ gravity by compactifying the infinite phase space into a finite space via the Poincaré transformation. On the expansion branch of the phase space, the constraint surface has a repeller and a de Sitter attractor. On the contraction branch, the constraint surface has an attractor and a de Sitter repeller. Generally, the phase currents originate from the repeller and terminate at the corresponding attractor in each space. The trajectories between the repeller and the attractor in the presence of matter density are different from those in the vacuum case. The phase analysis techniques developed in this chapter are very general and can be applied to other similar dynamical systems. This chapter is mainly based on Ref.[65]

4.1 Introduction

Any modified gravity model should fit the conventional standard cosmology as well as explain the current cosmic speed-up issue. Specifically, in a viable model, the Universe should have a matter domination epoch in the early Universe to enable the formation of large-scale structure, and it should transit from a matter domination epoch into the current dark energy domination one. Moreover, in order to be able to drive the cosmic speed-up, the effective dark energy should have sufficiently large negative pressure, and the effective equation of state should be less than $-1/3$.

The conditions for a viable matter domination epoch and late-time acceleration were derived via an analysis in phase space in Ref.[3] In fact, the dynamics of $f(R)$ gravity closely depends on a potential defined by $V'(\phi) \equiv dV/d\phi = (2f - \phi R)/3$, where $\phi \equiv f' = df(R)/dR$. In this chapter, the cosmological viability conditions are studied directly by considering how this potential determines the dynamics of $f(R)$ cosmology.

We explore the phase-space dynamics and cosmological evolution of the $R\ln R$ model and Hu-Sawicki model with the following techniques: compactifying the infinite phase space into a finite space via the Poincaré transformation; studying the vector fields on two-dimensional slices of the constraint surface when the constraint surface is three-dimensional; and plotting typical trajectories of the phase flows.

This chapter is organized as follows. In Sec. 4.2, we construct the dynamical system for $f(R)$ cosmology. In Sec. 4.3, the conditions of the cosmological viability for $f(R)$ gravity are explored. In Secs. 4.4 and 4.5, the phase-space dynamics and the cosmological evolution of the $R\ln R$ model are studied. In Sec. 4.6, we explore the phase-space dynamics of the Hu-Sawicki model. Lastly, Sec. 4.7 summarizes our results.

4.2 Dynamical system in $f(R)$ cosmology

4.2.1 Basic equations

In this section, we prepare for the dynamical analysis of $f(R)$ cosmology. The equivalent of the Einstein equation in $f(R)$ gravity reads,

$$f'R_{\mu\nu} - \frac{1}{2}fg_{\mu\nu} - (\nabla_\mu\nabla_\nu - g_{\mu\nu}\Box)\,f' = 8\pi G T_{\mu\nu}, \tag{4.1}$$

where f' denotes the derivative of the function f with respect to its argument R, and $\Box$ is the usual notation for the covariant D'Alembert operator $\Box \equiv \nabla_\alpha \nabla^\alpha$. Compared to general relativity, $f(R)$ gravity has one extra scalar degree of freedom, f'. The dynamics of this degree of freedom is determined by the trace of Eq. (4.1)

$$\Box f' = \frac{1}{3}(2f - f'R) + \frac{8\pi G}{3}T, \tag{4.2}$$

where T is the trace of the stress-energy tensor $T_{\mu\nu}$. Identifying f' with a scalar degree of freedom by

$$\phi \equiv \frac{df}{dR}, \tag{4.3}$$

and defining a potential $V(\phi)$ by

$$V'(\phi) \equiv \frac{dV}{d\phi} = \frac{1}{3}(2f - \phi R), \tag{4.4}$$

one can rewrite Eq. (4.2) as

$$\Box\phi = V'(\phi) + \frac{8\pi G}{3}T. \tag{4.5}$$

We consider the homogeneous Universe with the flat Friedmann-Robertson-Walker metric,

$$ds^2 = -dt^2 + a^2(t)d\boldsymbol{x}^2, \tag{4.6}$$

where $a(t)$ is the scale factor. In this case, the evolution of the Universe is described by a four-dimensional dynamical system of $\{\phi, \pi, H, a\}$, where

$$\pi \equiv \dot{\phi}, \tag{4.7}$$

H is the Hubble parameter, and the dot $(\cdot)$ denotes the derivative with respect to the coordinate time t. Equation (4.2) provides the equation of motion for π

$$\dot{\pi} = -3H\pi - V'(\phi) + \frac{8\pi G}{3}\rho_m. \tag{4.8}$$

The equation of motion for H is

$$\dot{H} = \frac{R}{6} - 2H^2. \tag{4.9}$$

The definition of the Hubble parameter implies that

$$\dot{a} = aH. \tag{4.10}$$

The system is constrained by the Friedman equation

$$H^2 + \frac{\pi}{\phi}H + \frac{f - \phi R}{6\phi} - \frac{8\pi G}{3\phi}(\rho_m + \rho_r) = 0, \tag{4.11}$$

where ρ_m and ρ_r are the density of matter and density of radiation, respectively. Equations (4.7)-(4.11) provide a closed description of the dynamical system $\{\phi, \pi, H, a\}$.

In order to explore whether $f(R)$ gravity can account for the cosmic speed-up, it is instructive to cast the formulation of $f(R)$ gravity into a format similar to that of general relativity. We rewrite Eq. (4.1) as

$$G_{\mu\nu} = 8\pi G\left[T_{\mu\nu} + T^{(\text{eff})}_{\mu\nu}\right], \tag{4.12}$$

where

$$8\pi G T^{(\text{eff})}_{\mu\nu} = \frac{f - f'R}{2}g_{\mu\nu} + (\nabla_\mu\nabla_\nu - g_{\mu\nu}\Box)\, f' + (1 - f')G_{\mu\nu}.$$

$T^{\mu\nu}_{\text{eff}}$ is the energy-momentum tensor of the effective dark energy. It is guaranteed to be conserved, $T^{\mu\nu}_{\text{eff};\nu} = 0$. Equation (4.13) reveals the definition of the equation of state for the effective dark energy

$$w_{\text{eff}} \equiv \frac{p_{\text{eff}}}{\rho_{\text{eff}}}, \tag{4.13}$$

where

$$8\pi G\rho_{\text{eff}} = 3H^2 - 8\pi G(\rho_m + \rho_r) = \frac{f'R - f}{2} - 3H\dot{f}' + 3H^2(1 - f'), \tag{4.14}$$

$$8\pi G p_{\text{eff}} = H^2 - \frac{R}{3} - 8\pi G p_r = \ddot{f}' + 2H\dot{f}' + \frac{f - f'R}{2} + \left(H^2 - \frac{R}{3}\right)(1 - f'). \tag{4.15}$$

In order for an $f(R)$ model to account for the cosmic speed-up, w_{eff} should be less than $-1/3$.

4.2.2 Effective dark energy

For the reference consideration, in this subsection, we give derivations of Eqs. (4.14) and (4.15). The (t, t) component of Eq. (4.1) is

$$f'R_{00} + \frac{1}{2}f - [\nabla_0\nabla_0 - g_{00}\Box]f' = 8\pi G T_{00}. \tag{4.16}$$

Using

$$\Gamma^0_{11} = a\dot{a}, \qquad \Gamma^0_{22} = a\dot{a}r^2, \qquad \Gamma^0_{33} = a\dot{a}r^2\sin^2\theta,$$

we compute

$$R_{00} = -3\frac{\ddot{a}}{a}, \tag{4.17}$$

$$\nabla_0\nabla_0 f' = \ddot{f}' - f'_{,\alpha}\Gamma^{\alpha}_{00} = \ddot{f}', \tag{4.18}$$

$$\Box f' \equiv g^{\mu\nu}\nabla_\mu\nabla_\nu f' = g^{\mu\mu}\nabla_\mu\nabla_\mu f' = g^{\mu\mu}(f'_{,\mu\mu} - \Gamma^{\alpha}_{\mu\mu}f'_{,\alpha}) = -\ddot{f}' - 3\left(\frac{\dot{a}}{a}\right)\dot{f}'. \tag{4.19}$$

Substituting Eqs. (4.17)-(4.19) into (4.16), we obtain

$$-3\left(\frac{\ddot{a}}{a}\right)f' = -\frac{1}{2}f + \ddot{f}' + \Box f' + 8\pi G\rho_m. \tag{4.20}$$

Using $R_{11} = a\ddot{a} + 2\dot{a}^2$, the (r, r) component of Eq. (4.1) can be described by

$$\left[\frac{\ddot{a}}{a} + 2\left(\frac{\dot{a}}{a}\right)^2\right]f' = \frac{1}{2}f - \dot{f}'\left(\frac{\dot{a}}{a}\right) - \Box f' + 8\pi G p_r. \tag{4.21}$$

A combination of Eqs. (4.20) and (4.21) yields,

$$\begin{aligned} 6\left(\frac{\dot{a}}{a}\right)^2 f' &= f - 2\cdot\Box f' - 3\left(\frac{\dot{a}}{a}\right)\dot{f}' + 3\cdot 8\pi G p_r + \ddot{f}' + 8\pi G\rho_t \\ &= 2\cdot 8\pi G\rho_t + f'R - f - 6\left(\frac{\dot{a}}{a}\right)\dot{f}', \end{aligned}$$

where $\rho_t = \rho_m + \rho_r$, and we have used Eq. (4.19) and a revised form of Eq. (4.2),

$$3\cdot 8\pi G p_r = f'R - 2f + 3\Box f' + 8\pi G\rho_t.$$

Then we have

$$H^2 = \left(\frac{\dot{a}}{a}\right)^2 = \frac{1}{3f'}\left(8\pi G\rho_t + \frac{f'R - f}{2} - 3H\dot{f}'\right), \tag{4.22}$$

with which we obtain the expression for the matter density of the effective dark energy Eq. (4.14).

Note that

$$2\dot{H} + 3H^2 = 2\frac{\ddot{a}}{a} + \left(\frac{\dot{a}}{a}\right)^2.$$

Then a combination of Eqs. (4.20) and (4.21) leads to

$$2\dot{H} + 3H^2 = -\left(H^2 - \frac{R}{3}\right) = -\frac{1}{f'}\left(8\pi G p_r + \ddot{f}' + 2H\dot{f}' + \frac{f - f'R}{2}\right), \tag{4.23}$$

where we have used a revised format of Eq. (4.2),

$$-8\pi G\rho_t = f'R - 2f + 3\Box f' - 3\cdot 8\pi G p_r.$$

Then, we can achieve the expression for the pressure of the effective dark energy described by Eq. (4.15).

4.3 Cosmological viability conditions

Many $f(R)$ models have been proposed to address the current cosmic speed-up issue. It is necessary to check whether these models agree with the observations of both the early and late Universe. In a viable $f(R)$ theory, there should be a matter domination epoch in the early Universe such that large-scale structure could be formed. Moreover, the Universe should experience an acceleration during the late time. The cosmological viability conditions for $f(R)$ theory were discussed via dynamical analysis in phase space in Ref.[3] With this approach, one could investigate the conditions for the existence of a viable matter domination epoch prior to a late-time acceleration. These conditions can be expressed as

$$m(r) \approx 0^+ \quad \text{and} \quad \frac{dm}{dr} > -1, \quad \text{at } r \approx -1, \tag{4.24}$$

where $m \equiv f''R/f'$ and $r \equiv -f'R/f$. Actually, r and m are closely related to $V'(\phi)$ and $V''(\phi)$, respectively, with $V'(\phi)$ being defined by Eq. (4.4) and

$$V''(\phi) = \frac{f' - f''R}{3f''}. \tag{4.25}$$

In this section, we will revisit these cosmological viability conditions using the scalar field description for $f(R)$ gravity.

In the standard cosmology based on general relativity, a matter domination epoch (and also a radiation domination epoch) is ensured in the early Universe. Therefore, in order to obtain a long matter domination epoch in $f(R)$ gravity, one may consider how $f(R)$ gravity could be reduced to general relativity. The restoration of general relativity implies that

$$f(R) \approx f'R, \quad \text{with } \phi \equiv f' \approx 1, \tag{4.26}$$

which results in $r \approx -1$ as shown in Eq. (4.24). In the early Universe, the matter domination epoch should last long enough to ensure large-scale structure formation. This means that

general relativity should be restored for a long time. Therefore, f' should roll down very slowly. Combining Eqs. (4.7) and (4.8), one obtains

$$\ddot{\phi} = -3H\dot{\phi} - V'(\phi) + \frac{8\pi G}{3}\rho_m. \tag{4.27}$$

Consequently, when the field ϕ evolves slowly, we have

$$|3H\dot{\phi}| \ll V'(\phi) \approx \frac{8\pi G}{3}\rho_m. \tag{4.28}$$

Note that $\rho_m = \rho_{m0}/a^3$ and $\dot{a} = aH$, where ρ_{m0} is the matter density of the current Universe. Taking the time derivative of $V'(\phi) \approx 8\pi G\rho_m/3$, we arrive at

$$V'' \cdot \dot{\phi} \approx -8\pi G\frac{\rho_{m0}}{a^4}\dot{a} = -8\pi G\rho_m H \approx -3HV',$$

and therefore

$$\dot{\phi} \approx -3H\frac{V'}{V''}. \tag{4.29}$$

Substituting Eq. (4.29) into (4.28) yields

$$|3\dot{\phi}H| \approx 9H^2\frac{V'}{V''} \ll V' \approx \frac{8\pi G}{3}\rho_m. \tag{4.30}$$

Then we have

$$V'' \gg 9H^2 \approx 3 \cdot 8\pi G\rho_m. \tag{4.31}$$

The condition expressed by Eq. (4.31) can be interpreted as follows. Note that the potential $V(\phi)$ should have a minimum so that there could be a dark energy domination epoch in the late Universe. In the early Universe, the field ϕ evolves slowly, and stays at the quasistatic equilibrium of $V'(\phi) \approx 8\pi G\rho_m/3$ as shown in Eq. (4.28). Therefore, the field ϕ and the matter density ρ_m are coupled. From this coupling, the field ϕ acquires a mass. When the mass of ϕ is heavy [large $V''(\phi)$], it is hard to excite ϕ. Then the field ϕ stays near 1 for a long time. Consequently, general relativity is restored for a long time and the Universe has a long matter domination epoch. The matter density decreases slowly. The field ϕ then becomes light, and is eventually released from the coupling to the matter density and approaches the de Sitter minimum of the potential $V(\phi)$. Note that we only consider the case in which the potential $V(\phi)$ has a de Sitter minimum, like the case plotted in Fig. 3.2. Correspondingly, the Universe transits from the matter domination epoch into the dark energy domination epoch.

Substituting Eq. (4.25) into (4.31), and noting that in the general relativistic limit $R \approx 8\pi G\rho_m$, one obtains

$$f' \gg f''R. \tag{4.32}$$

The condition for the recovery of general relativity is given by Eq. (4.31) or Eq. (4.32). Equation (4.32) is equivalent to $m(r) \approx 0^+$, shown in Eq. (4.24). Equation (4.32) can be interpreted via a comparison of the modification term and the main term of the function $f(R)$. We write the function $f(R)$ as $f(R) = R + A(R)$, where R is the main term and $A(R)$ is the modification term. If $f(R)$ theory satisfies Eq. (4.26) at a certain time in the early Universe, which means that $|A(R)| \ll R$ and $|A'(R)| \ll 1$, there is a matter domination epoch at that time. However, to make this matter domination and/or the general relativity recovery last long enough, $A'(R)$ should also change with respect to R more slowly than $1/R$, namely $A''(R) \ll 1/R$, as implied in Eq. (4.32).

The process of the field ϕ obtaining a mass from its coupling to the matter density is very similar to the chameleon mechanism studied in the context of the Solar System tests of $f(R)$ gravity.[49,64,66,72,84,85,97,128,131] In the chameleon mechanism, the field ϕ is coupled to the matter densities of the Sun and of the background, respectively. The field ϕ acquires a large mass from this coupling. Therefore, $f(R)$ gravity could in principle evade the Solar System tests.

In addition to having a long matter domination epoch in the early Universe, a viable $f(R)$ model should also have a stable dark energy domination epoch in the late Universe to account for the cosmic acceleration. [The potential $V(\phi)$ needs to have a minimum.] Generally, the parameters in viable $f(R)$ models need to take values that can make a trade-off between the two requirements.

4.4 Phase-space dynamics of the $R \ln R$ model

In this section, we study the cosmic dynamics of the $R \ln R$ model, as introduced in Chapter 3, in phase space.

$$f(R) = R\left(1 + \alpha_0 \ln \frac{R}{R_0}\right), \tag{4.33}$$

where α_0 and R_0 are positive constants. The cosmic dynamics of $f(R)$ gravity is described by Eqs. (4.7)-(4.11), as shown in Sec. 4.2. For the $R \ln R$ model, the equations of motion

(4.7)-(4.10) can be rewritten as

$$\pi \equiv \dot{\phi}, \tag{4.34}$$

$$\dot{\pi} = -3H\pi - \frac{1}{3}\Lambda e^{\frac{\phi}{\alpha_0}-2}(\phi - 2\alpha_0) + \frac{8\pi G}{3}\rho_m, \tag{4.35}$$

$$\dot{H} = \frac{1}{6}\Lambda e^{\frac{\phi}{\alpha_0}-2} - 2H^2, \tag{4.36}$$

$$\dot{a} = aH. \tag{4.37}$$

The constraint equation (4.11) becomes

$$H^2 + \frac{\pi}{\phi}H - \frac{\Lambda}{6\phi}e^{\frac{\phi}{\alpha_0}-2} - \frac{8\pi G}{3\phi}(\rho_m + \rho_r) = 0. \tag{4.38}$$

4.4.1 Phase-space dynamics in vacuum

For simplicity, we first consider the dynamics in vacuum, where both ρ_m and ρ_r are equal to zero. In this case, the solutions to the constraint equation (4.38) are

$$H_{\pm} = \frac{1}{2}\left[-\frac{\pi}{\phi} \pm \sqrt{\left(\frac{\pi}{\phi}\right)^2 + \frac{2\Lambda}{3\phi}e^{\frac{\phi}{\alpha_0}-2}}\right]. \tag{4.39}$$

Since the domains of $\{\phi, \pi, H\}$ span from $-\infty$ to $+\infty$, it is hard to directly view the global structure of the constraint surface in the space of $\{\phi, \pi, H\}$. Instead, we use the Poincaré compactification in the cylindrical coordinate system to transform ϕ, π, and H, respectively, to

$$\begin{aligned} \phi_P &\equiv \tfrac{\phi}{\sqrt{\sigma+\phi^2+\pi^2}}, \\ \pi_P &\equiv \tfrac{\pi}{\sqrt{\sigma+\phi^2+\pi^2}}, \\ H_P &\equiv \tfrac{H}{\sqrt{\sigma+H^2}}, \end{aligned} \tag{4.40}$$

where σ is an arbitrary constant, and we set it to 12 for the $R\ln R$ model. In this way, the constraint surface is compactified into a finite space, as shown in Fig. 4.1. The Hubble parameter on the upper branch of the constraint surface is positive, corresponding to an expanding Universe, whereas the lower branch corresponds to a contracting one. The

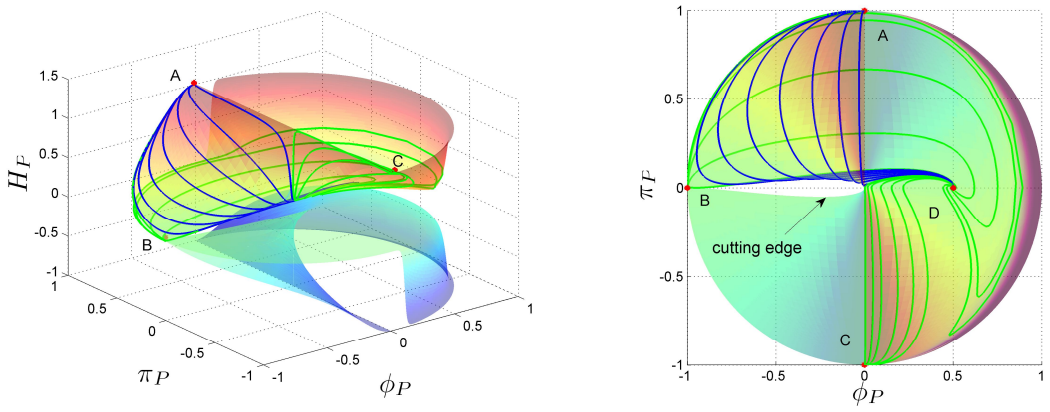

(a) Constraint surface (b) Top view

Figure 4.1: Constraint surface and phase-space flows with $\rho_m = 0$ for the $R \ln R$ model, with $\alpha_0 = R_0 = 1$. The phase currents flow out of point A and move to point D. Point A is a repeller, points B and C are saddle points, and point D is an attractor. Regarding the trajectories in green (light color), the parts of them between A and C are not plotted due to the difficulty in obtaining an accurate numerical integration near the boundary. The shadings correspond to the values of H_P. A color bar is not shown because the values of H_P can be seen from the z axis.

constraint surface is folded in the octants of $(\phi \leq 0, \pi \geq 0, H \geq 0)$ and $(\phi \leq 0, \pi \leq 0, H \leq 0)$. On the folding line, which we also call a cutting edge, the solutions of H_+ and H_- merge and become equal. This and Eq. (4.39) together imply that the cutting edge can be described by

$$\pi_\pm = \pm\sqrt{-\frac{2}{3}\Lambda e^{\frac{\phi}{\alpha_0}-2}\phi}. \tag{4.41}$$

When ϕ goes to $-\infty$, the $\pi_\pm$ approach $0^\pm$ and the cutting edge is almost closed, as shown in Fig. 4.1. We denote the two ends of the cutting edge as point $B(\phi_P = -1, \pi_P = 0^+, H_P = 0^+)$ and point $B'(\phi_P = -1, \pi_P = 0^-, H_P = 0^-)$, respectively. The two branches of the constraint surface are disconnected. The reasons for this fact are explained below.

We consider the constraint equation (4.39). For positive ϕ, we have $2\Lambda \exp(\phi/\alpha_0 - 2)/(3\phi) > 0$. Consequently, we have $H_+ > 0$ and $H_- < 0$. For negative ϕ, the expansion branch of the constraint surface belongs to the space of $(\phi < 0, \pi > 0)$, while the contraction branch belongs to the space of $(\phi < 0, \pi < 0)$. As shown in Fig. 4.1, the two branches are close to each other around point B and point B'. As implied by Eq. (4.41), at point B, $\pi_P = 0^+$, and at point B', $\pi_P = 0^-$. Therefore, B and B' are separated, and then the two

branches are separated as well. In summary, the two branches of the constraint surface are disconnected, although they both asymptote to the point $(\phi_P = -1, \pi_P = 0, H_P = 0)$ when compactified.

In this paragraph and the next, the critical points on the constraint surface in vacuum will be briefly discussed. More details are given in Sec. 4.4.2. In the vacuum evolution, the phase-space flows stay on the constraint surface. Some typical trajectories of the flows with $H_P > 0$ are plotted in Fig. 4.1. There are four special points on the branch with $H_P > 0$ of the constraint surface as listed below:

$$A : (\phi_P = 0^-, \pi_P = 1, H_P = 1),$$

$$B : (\phi_P = -1, \pi_P = 0^+, H_P = 0^+),$$

$$C : (\phi_P = 0^+, \pi_P = -1, H_P = 1),$$

$$D : \left(\phi_P = 0.5, \pi_P = 0, H_P = \frac{\sqrt{\Lambda/(12\alpha_0)}}{\sqrt{\sigma+\Lambda/(12\alpha_0)}} = 0.083\right).$$

At point A, the kinetic term π_P is dominant over the field ϕ_P, $\dot{\phi}_P = -2$, and $\dot{\pi}_P = \dot{H}_P = 0$. All of the phase currents flow out of point A and move to point D. Therefore, loosely speaking, point A is a repeller. Point B is at one end of the cutting edge. At point B, the field ϕ_P is dominant over the kinetic term π_P, and $\dot{\phi}_P = \dot{\pi}_P = \dot{H}_P = 0$. Moreover, near point B, the currents slowly approach and then move away from point B. Thus, point B is a saddle point. Similarly, point C is also a saddle point. At point C, the kinetic term π_P is dominant over the field ϕ_P. When ρ_m is equal to zero, Eq. (4.5) reads

$$\ddot{\phi} + 3H\dot{\phi} + V'(\phi) = 0. \tag{4.42}$$

Therefore, on the upper branch of the constraint surface with $H_P > 0$, due to the friction force $-3H\dot{\phi}$, the field ϕ will eventually arrive and stay at the minimum of the potential, where $V'(\phi) = 0$, $\phi = 2\alpha_0$, $\pi = 0$, and $H = \sqrt{\Lambda/(12\alpha_0)}$. This minimum corresponds to point D in Fig. 4.1, which is an attractor and is also called a de Sitter point. When the field ϕ comes to this point, only dark energy exists in the Universe, with normal matter diluted away.

We project the phase diagrams onto the regular space (ϕ, π, H). Near the cutting edge, the directions of the flows are described as

$$\left.\frac{d\pi}{d\phi}\right|_{\text{flow}} = \frac{\dot{\pi}}{\dot{\phi}} = -(\phi+1)\sqrt{-\frac{\Lambda}{6\phi}e^{\frac{\phi}{\alpha_0}-2}}. \tag{4.43}$$

On the other hand, with Eq. (4.41), the slope of the tangent to the edge yields the same expression. To conclude, the phase-space flows are tangential to the cutting edge and do not enter the forbidden area enclosed by the edge. In other words, the constraint equation forces the currents to stay on the surface. These conclusions also apply to the compactified space $\{\phi_P, \pi_P, H_P\}$.

The corresponding behavior of the phase currents on the lower branch of the constraint surface with $H_P < 0$ can be analyzed in a similar way. There are still four critical points on this branch, as listed below:

$$A' : (\phi_P = 0^+, \pi_P = 1, H_P = -1),$$

$$B' : (\phi_P = -1, \pi_P = 0^-, H_P = 0^-),$$

$$C' : (\phi_P = 0^-, \pi_P = -1, H_P = -1),$$

$$D' : (\phi_P = 0.5, \pi_P = 0, H_P = -0.083)\,.$$

The phase flows originate from the repeller point D', and terminate at the attractor point C'. Point A' and point B' are saddle points.

4.4.2 Critical points

In this subsection, with the knowledge on dynamical analysis in the Appendix 4.8, we classify the critical points mentioned in the last subsection. Use the notation in the Appendix 4.8, the matrix for the dynamical system $\{\phi_P, \psi_P, H_P\}$ can be described as

$$M = \begin{pmatrix} \frac{\partial \dot{\phi_P}}{\partial \phi_P} & \frac{\partial \dot{\phi_P}}{\partial \pi_P} & \frac{\partial \dot{\phi_P}}{\partial H_P} \\ \frac{\partial \dot{\pi_P}}{\partial \phi_P} & \frac{\partial \dot{\pi_P}}{\partial \pi_P} & \frac{\partial \dot{\pi_P}}{\partial H_P} \\ \frac{\partial \dot{H_P}}{\partial \phi_P} & \frac{\partial \dot{H_P}}{\partial \pi_P} & \frac{\partial \dot{H_P}}{\partial H_P} \end{pmatrix}. \tag{4.44}$$

For convenience, in computing the above matrix, we use the normal variables ϕ, π, and H as intermediate one. For example, near the infinity critical points, we use

$$\frac{\partial \dot{\phi_P}}{\partial \phi_P} \approx \frac{\frac{\partial \dot{\phi_P}}{\partial \phi}}{\frac{\partial \phi}{\partial \phi_P}}.$$

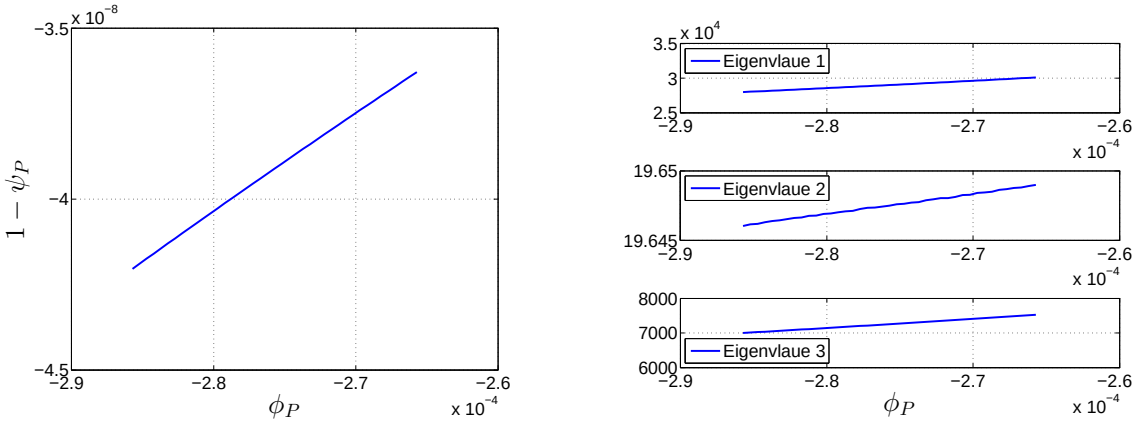

(a) Trajectory (b) Eigenvalues of M

Figure 4.2: Eigenvalues of the matrix M near the critical point A. Along the trajectory in (a), $H_P = 0.9999995$. All the three set of eigenvalues are positive, so point A is a repeller.

We compute the eigenvalues of the matrix M along a trajectory near the critical points A, B, and C. The results for point A are shown in Fig. 4.2. The three set of eigenvalues are all positive, implying that point A is a repeller. Near the critical point B, at $(\phi_P = -0.99997, \psi_P = -0.00377, H_P = 0.00110)$, the eigenvalues are -0.0111, 0.0005, and -0.0151. These show that point B is a saddle point. Near the critical point C, at $(\phi_P = 0.00489, \psi_P = -0.99998, H_P = 0.99986)$, the eigenvalues are 2900, -1400, and 400. Therefore, point C is a saddle point. It is so obvious that point D is an attractor, computations of the corresponding eigenvalues are skipped.

4.4.3 Phase-space dynamics in the presence of matter

The constraint surface described by Eq. (4.38) is three-dimensional when the matter or radiation density is not zero. For ease of visualization, we explore the vector fields of $\{\dot{\phi}_P, \dot{\pi}_P, \dot{H}_P\}$ on the slices where $H_P =$ const in the three-dimensional space $\{\phi_P, \pi_P, H_P\}$, with the scale factor a being taken as an implicit variable and ρ_r equal to zero.

Some typical slices of the vector fields $\{\dot{\phi}_P, \dot{\pi}_P\}$ with H_P taking different values from -1 to 1 are shown in Fig. 4.3. The thinner (blue) arrows denote that $\dot{H}_P < 0$ at the positions of the arrows, and the thicker (red) arrows are for $\dot{H}_P > 0$. The solid (black) line is the intersection between the two-dimensional constraint surface of Eq. (4.39) and the slice of $H_P =$ const. The dashed (cyan) line is the trace of $\dot{\pi}_P = 0$, and point C is at one end of

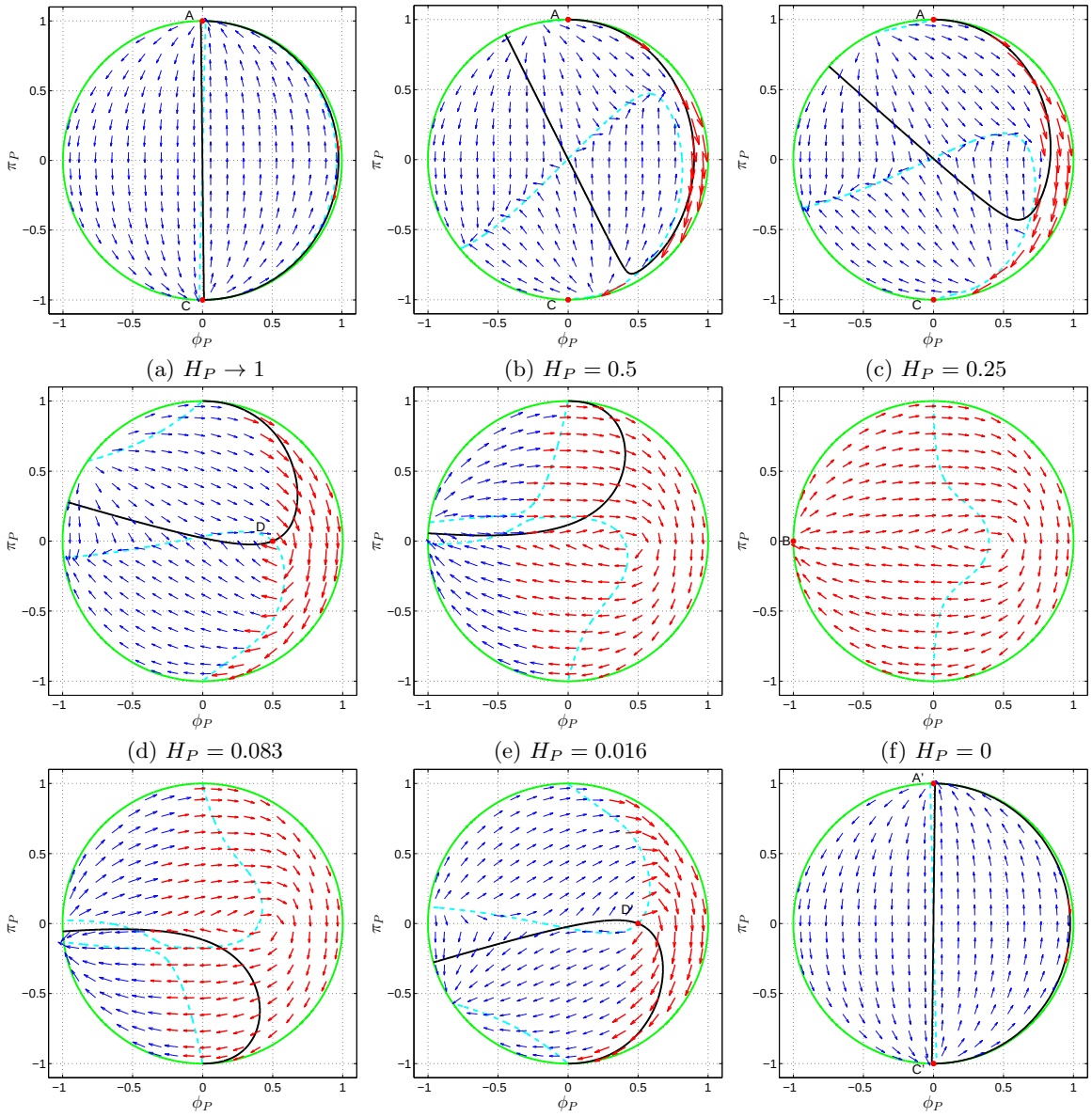

(a) $H_P \to 1$ (b) $H_P = 0.5$ (c) $H_P = 0.25$

(d) $H_P = 0.083$ (e) $H_P = 0.016$ (f) $H_P = 0$

(g) $H_P = -0.016$ (h) $H_P = -0.083$ (i) $H_P \to -1$

Figure 4.3: Vector fields of $\{\dot{\phi}_P, \dot{\pi}_P, \dot{H}_P\}$ on the slices of $H_P =$ const for the $R \ln R$ model, with $\alpha_0 = R_0 = 1$. The thinner (blue) arrows denote that $\dot{H}_P < 0$ at the positions of the arrows. The thicker (red) arrows are for $\dot{H}_P > 0$. The solid (black) line is the intersection between the two-dimensional vacuum constraint surface and the slice of $H_P =$ const. The dashed (cyan) line is the trace of $\dot{\pi}_P = 0$, where the flows change the direction of the $\dot{\pi}_P$ component. In (d), point D is an attractor. In (f), point B is a saddle point. In (h), point D' is a repeller. In (i), point A' is a saddle point and point C' is an attractor.

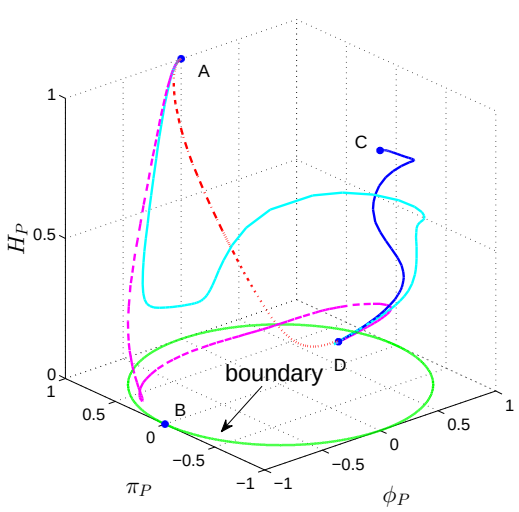

(a) Trajectories with $\rho_m > 0$

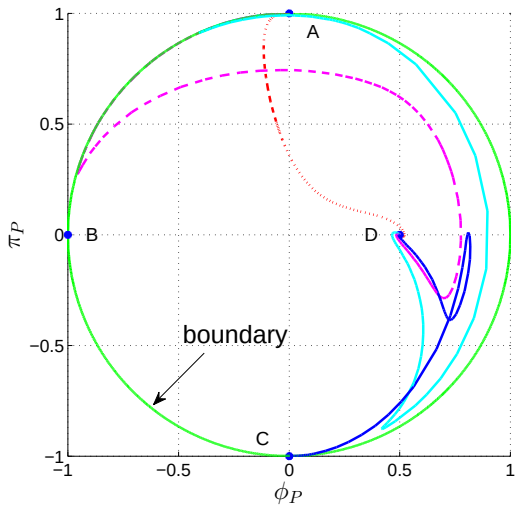

(b) Top view

Figure 4.4: Some typical trajectories of the phase-space flows with $\rho_m > 0$ for the $R \ln R$ model, with $\alpha_0 = R_0 = 1$. Compared to the vacuum case, in the $\rho_m > 0$ case, the phase-space flows still originate at point A and terminate at point D. Regarding the trajectory plotted in a solid (blue) line, one part of it between A and C is not shown due to the difficulty in obtaining an accurate numerical integration near the boundary.

this trace. The two-dimensional constraint surface described by Eq. (4.39) is the separation surface for the signs of the matter density term. The matter density is positive in the space enclosed by the constraint surface, and is negative outside the surface. The vector fields and some typical trajectories of the phase-space flows can be combined together to study the tendencies of the phase flows, as done below.

To complement the vector-field-slice approach, some typical trajectories of the phase-space flows with $\rho_m > 0$ are plotted in Fig. 4.4. Note that although the trajectories for $\rho_m < 0$ may not be physically meaningful, we plot them in Fig. 4.5 for completeness. Compared to the vacuum case, the phase-space flows still originate at point A and terminate at point D, but the trajectories between point A and point D can be different from the vacuum solutions. Some flows, such as those plotted with solid (cyan) and dashed (magenta) lines in Fig. 4.4, behave similarly to those in the vacuum case shown in Fig. 4.1. The flows go down from point A, then up, then make a turn and go down to point D. This is also shown in Figs. 4.3(a)-(c). The thinner (blue) arrows near point A in Fig. 4.3(a) show the downward movement from point A. The thicker (red) arrows near the boundary in Figs. 4.3(b) and (c)

show the upward movement. The thinner (blue) and thicker (red) arrows near the dashed (cyan) line in Figs. 4.3(b) and (c) show the turn and movement down to point D. Some flows (well away from the constraint surface in vacuum), such as those plotted in dash-dotted (red) and solid (blue) lines in Fig. 4.4, can be very different from those in the vacuum case. The flow plotted with a dash-dotted (red) line goes directly downwards from point A to point D. This behavior can also be observed from the thinner (blue) arrows in the region $-0.5 < \phi_p < 0.5$ and $\pi_p > 0$ in Figs. 4.3(a)-(d). Regarding the trajectory plotted with a solid (blue) line in Fig. 4.4, one part of it from point A to point C is not shown due to the difficulty in obtaining an accurate numerical integration near the boundary. The part of this trajectory from point C to point D goes down from point C, makes two turns, and approaches point D. This is also shown by the thinner (blue) arrows at the corresponding places in Figs. 4.3(b)-(d).

The fact that point D is still an attractor in the presence of matter is related to the dynamics of the scale factor a. Equation (4.10) implies that $\dot{a}$ is positive when the Hubble parameter H is positive. Then the matter density keeps decreasing in the evolution and asymptotically comes to zero. Correspondingly, the phase flows approach point D.

The flows with $\rho_m < 0$ are between or outside the two branches of the vacuum constraint surface. In the $R \ln R$ model, when $H = H_P = 0$, Eq. (4.9) becomes

$$\dot{H} = \frac{R}{6} = \frac{1}{6} R_0 \exp\left(\frac{\phi - 1 - \alpha_0}{\alpha_0}\right) > 0.$$

So $\dot{H}_P$ is positive on the whole slice of $H_P = 0$, as is also shown in Fig. 4.3(f). Therefore, the flows from the repeller point A do not cross the slice of $H_P = 0$. In fact, the flows from point A for $\rho_m < 0$ still end at the attractor point D. Some flows from the repeller point D' with $\rho_m < 0$ can cross the slice of $H_P = 0$, and end at the attractor point D. These are shown in Fig. 4.5.

Some slices of the vector fields $\{\dot{\phi}_P, \dot{\pi}_P\}$ with $H_P < 0$ are shown in Figs. 4.3(g)-(i). The typical behavior of the phase flows can be analyzed in a similar way as was done in the case of $H_P > 0$, and is not included.

4.5 Cosmological evolution of the $R \ln R$ model

In the previous section, we studied the global behavior of phase-space dynamics in $f(R)$ cosmology, where ρ_m and ρ_r are independent of the Hubble parameter, H. In this section,

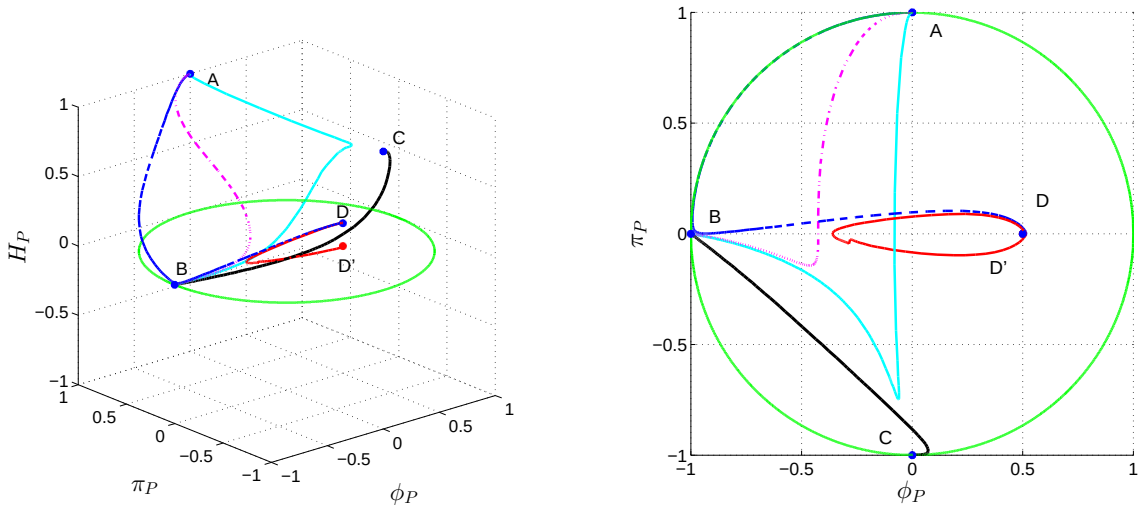

(a) Trajectories with $\rho_m < 0$ (b) Top view

Figure 4.5: Some trajectories of phase flows with $\rho_m < 0$ for the $R \ln R$ model. The flows marked by (blue) dashed, (magenta) dash-dot, (cyan) solid, and (black) solid lines originate from point A, and terminate at point D. The flow marked as a (red) solid line starts from point D', crosses the slice of $H_P = 0$, and ends at point D. The part between A and C for the trajectory of the (black) solid line is not plotted due to the difficulty in obtaining accurate numerical integration near the line of $\phi \to 0$.

we explore the physically more important solution where the scalar field ϕ tracks the matter density evolution, and ρ_m and ρ_r are related to H by

$$\frac{8\pi G}{3}(\rho_m + \rho_r) \equiv (\Omega_m + \Omega_r)H^2 = \left(\frac{\Omega_{m,0}}{a^3} + \frac{\Omega_{r,0}}{a^4}\right) H_0^2,$$

where the "0" in the indices denotes that the quantities are measured today with $z = 0$. The $\Omega_i{}'s$ are defined as $\Omega_i = 8\pi G\rho_i/(3H^2)$, where the index i refers to radiation or matter. At high redshift, the field ϕ of this solution closely follows the minimum of the effective potential V_{eff}, which is defined by $V'_{\text{eff}} = V'(\phi) - 8\pi G\rho_m/3$ [see Eq. (4.8)], until the field ϕ becomes very light and "releases," approaching the de Sitter minimum of the potential $V(\phi)$.

Equation (4.33) shows that the model is reduced to general relativity when R is equal to R_0. However, the field ϕ logarithmically runs with respect to $X = 8\pi G\rho/\Lambda$, and the $R\ln R$ model slowly deviates from general relativity. We set units so that R_0 is equal to 1, and let R be equal to R_0 around the redshift $z = 3.5 \times 10^4$, where the matter-radiation equality takes place.[89]

The cosmological acceleration is a low-curvature issue. Consequently, $f(R)$ gravity should be reduced to general relativity at the high-curvature scale, and deviate from general relativity at the low-curvature scale. However, in the $R\ln R$ model, the modification term is not negligible at both the high- and low-curvature scales. In order to reduce this model to general relativity at the high-curvature scale, the parameter α_0 should be much less than 1. However, α_0 cannot be too small because of the relation between the de Sitter curvature and α_0, $\Lambda = R_0 e^{-1/\alpha_0+1}$, and also because of the relation between the mass of the field and α_0. Note that the mass of the field ϕ is defined by

$$m^2 \equiv V''(\phi) = \frac{1}{3}\Lambda e^{\frac{\phi}{\alpha_0}-2}\left(\frac{\phi}{\alpha_0} - 1\right). \tag{4.45}$$

A tiny α_0 generates an extremely small value for Λ and a heavy mass for the field ϕ. Consequently, the matter domination stage would last too long due to the extremely small value of Λ, and the evolution of ϕ would be very slow due to its heavy mass, which is shown in Figs. 4.6(a) and (d). With the same arguments, the parameter α_0 cannot be too large either. A large α_0 would result in a short matter domination epoch (if such an epoch were to exist) and a fast evolution of ϕ. These arguments are illustrated in Figs. 4.6(b) and (d), respectively. Consequently, one needs to choose an intermediate value for α_0. Letting α_0 take a value of 0.02, we plot the evolution of the $\Omega_i{}'s$ and w_{eff} in Fig. 4.6(c), and the evolution of ϕ in Fig. 4.6(d). In this solution, matter-radiation equality takes place around a

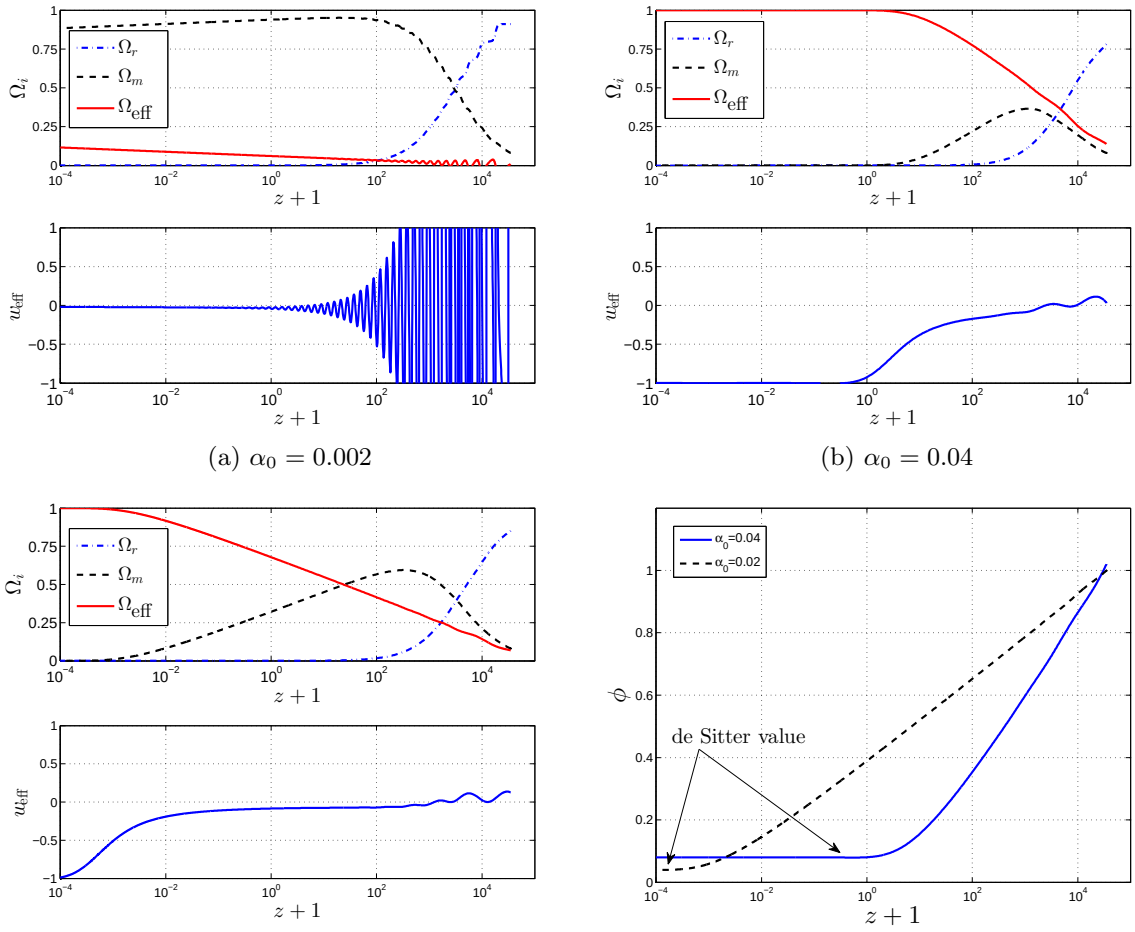

(a) $\alpha_0 = 0.002$ (b) $\alpha_0 = 0.04$

(c) $\alpha_0 = 0.02$ (d) evolution of ϕ

Figure 4.6: Cosmological evolution for the $R \ln R$ model with $R_0 = 1$. (a) Cosmological evolution with $\alpha_0 = 0.002$. A tiny value of α_0 will generate an extremely small value of $\Lambda (= R_0 e^{-1/\alpha_0 + 1})$, then a super long matter domination stage. (b) Cosmological evolution with $\alpha_0 = 0.04$. A large α_0 makes a small $V''(\phi)$ and then a fast evolution of ϕ. (c) Cosmological evolution with $\alpha_0 = 0.02$. (d) Evolution of the field ϕ with α_0 taking different values.

redshift of $z = 3250$,[89] and $\Omega_m = 0.32$ at $z = 0$. The field ϕ runs significantly depending on the matter density, as shown in Eq. (3.24). Consequently, the effective dark energy density also changes significantly as implied in Eq. (4.14). As a result, there is no ideal matter domination epoch at high redshift. Moreover, w_{eff} is far away from the expected value of -1 in the late Universe for this model.

The equation of state w_{eff} oscillates as shown in Fig. 4.6. This is related to the initial conditions in the numerical simulations, and can be explained as follows. At high redshift, the field ϕ oscillates near the minimum of the effective potential $V_{\text{eff}}(\phi)$, defined by $V'_{\text{eff}}(\phi) = V'(\phi) - 8\pi G\rho_m/3$. [See Eq. (4.27).] The close dependence of w_{eff} on the kinetic terms of $\dot{\phi}$ and $\ddot{\phi}$ also makes w_{eff} oscillate.[126,130] [See Eqs. (4.13), (4.14), and (4.15), which define w_{eff}.]

In Sec. 4.3, we analyzed the cosmological viability of $f(R)$ gravity, and concluded that a heavy mass for the field ϕ would result in a slow evolution of ϕ and thus a long matter domination epoch, and vice versa. These conclusions are verified by the evolution of the $\Omega_i's$ and ϕ, as shown in Fig. 4.6.

4.6 Phase-space dynamics of the Hu-Sawicki model

In the $R\ln R$ model, general relativity is recovered only for a particular range of curvature scales due to the logarithmic running of f' with respect to the matter density. This makes it hard for the $R\ln R$ model to have a sensible cosmological evolution. Actually, this problem is alleviated in the modified logarithmic model

$$f(R) = R\frac{a + \ln(R/R_0)}{1 + \ln(R/R_0)} = R\left[1 - \frac{b}{1 + \ln(R/R_0)}\right], \tag{4.46}$$

where $b = 1 - a$, because in this model f' asymptotes to a finite value and general relativity is restored at the high-curvature scale. In this model, the running of the beta function, $\beta = -k(\alpha - \alpha_*)^2$, is essentially the same as in the $R\ln R$ model. k and α_* are positive constants. Therefore, this model can still generate a hierarchy. However, because of the slow logarithmic running with R, the function $f(R)$ still deviates noticeably from general relativity from $R = R_0$ to $R \gg R_0$.

In the ΛCDM-like models, the scalar field f' is almost frozen when the Ricci scalar is greater than the cosmological constant scale, and is released when the Ricci scalar is close to the cosmological constant scale. Therefore, a model of this type has an advantage when

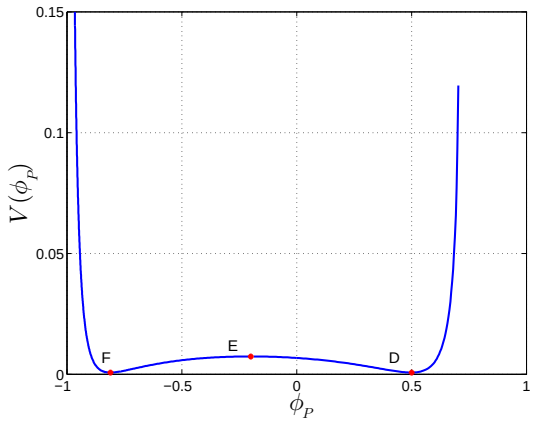

Figure 4.7: The potential $V(\phi_P)$, obtained via integration of Eq. (4.50), for the Hu-Sawicki model, with $C = 1.2$ and $R_0 = 1$. ϕ_P is a compactified coordinate obtained via the Poincaré transformation, $\phi_p = \phi/\sqrt{1+\phi^2}$.

it comes to generating a sensible cosmological evolution and avoiding the local tests. In this section, we apply the techniques developed above to a typical example of ΛCDM-like models: the Hu-Sawicki model. We consider one of the simplest versions of this model,

$$f(R) = R - \frac{CR_0R}{R+R_0}, \tag{4.47}$$

where C is a dimensionless parameter. With this choice,

$$f' = 1 - \frac{CR_0^2}{(R+R_0)^2}, \tag{4.48}$$

$$R = R_0\left[\sqrt{\frac{C}{1-f'}} - 1\right], \tag{4.49}$$

$$V'(\phi) = \frac{R^3}{3(R+R_0)^2}\left[1 + (1-C)\frac{R_0}{R}\left(2 + \frac{R_0}{R}\right)\right]. \tag{4.50}$$

Equations (4.48) and (4.50) show that as long as the matter density is much greater than R_0, the curvature R will trace the matter density well, ϕ will be close to 1 but will not cross 1, and general relativity will be restored. As implied in Eq. (4.50), in order for this model to have a de Sitter attractor where $V'(\phi) = 0$, the parameter C needs to be greater than 1. We set C to 1.2.

Integrating Eq. (4.50) leads to the potential $V(\phi)$, as plotted in Fig. 4.7, with the integration constant being set arbitrarily. The potential has three special points: two minimum

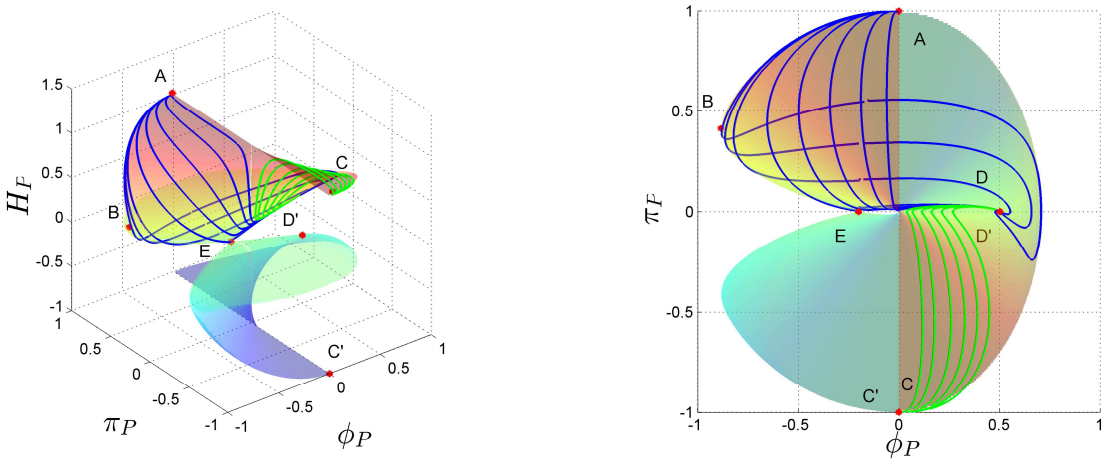

(a) Constraint surface (b) Top view

Figure 4.8: Constraint surface and phase-space flows with $\rho_m = 0$ for the Hu-Sawicki model, with $C = 1.2$ and $R_0 = 1$. As in the $R \ln R$ model, point A is a repeller, points B and C are saddle points, and point D is an attractor. Point C' is an attractor, and point D' is a repeller. Point E is a critical saddle point. It is also the only point connecting the two branches, $H_P \geq 0$ and $H_P \leq 0$, of the constraint surface. In (b), the left boundary of the constraint surface is defined by $\phi \equiv f' = 1$. Regarding the trajectories in green (light color), the parts of them between A and C are not plotted due to the difficulty in obtaining accurate numerical integration near the boundary. The shadings correspond to the values of H_P. A color bar is not shown because the values of H_P can be seen from the z axis.

points D, F, and one maximum point E. Points D and E are also shown on the constraint surface in the vacuum case, as plotted in Fig. 4.8. However, point F is not shown in Fig. 4.8, because its corresponding Hubble parameter is a complex number.

4.6.1 Phase-space dynamics in vacuum

We explore the phase-space dynamics of the Hu-Sawicki model using the Poincaré compactification in Eq. (4.40). For this model, the parameter σ in Eq. (4.40) is set to 1, and Eq. (4.48) implies that the left boundary of the phase space is constrained by $\phi \equiv f' = 1$. (Also see Fig. 4.7.)

We first study the structure of the vacuum constraint surface, which is plotted in Fig. 4.8. It is similar to that in the $R \ln R$ model. The surface is folded in the octants of $(\phi \leq 0, \pi \geq 0, H \geq 0)$ and $(\phi \leq 0, \pi \leq 0, H \leq 0)$. There are five critical points on the $H \geq 0$ branch

of the constraint surface for this model. When C and R_0 take the values of 1.2 and 1, respectively, the coordinates of these critical points are as follows:

$$A : (\phi_P = 0^-, \pi_P = 1, H_P = 1),$$

$$B : (\phi_P = -0.884, \pi_P = 0.412, H_P = 0.227),$$

$$C : (\phi_P = 0^+, \pi_P = -1, H_P = 1),$$

$$D : (\phi_P = 0.502, \pi_P = 0, H_P = 0.233),$$

$$E : (\phi_P = -0.196, \pi_P = 0, H_P = 0).$$

Similarly to the $R \ln R$ model, in the Hu-Sawicki model, point A is a repeller, points B and C are saddle points, and point D is an attractor. Point E is a new critical saddle point. It is on the cutting edge and also on one end of a critical line. Details regarding point E and the critical line are discussed below.

In the three-dimensional phase space $\{\phi, \pi, H\}$, the two-dimensional plane $\phi = 1 - C$ is very special. From Eqs. (4.47) and (4.49), one can see that on this plane

$$f(R) = R = 0. \tag{4.51}$$

The intersections between the constraint equation (4.11) in vacuum and the plane $\phi = 1-C$ in the octant $(\phi \leq 0, \pi \geq 0, H \geq 0)$ can be expressed as follows: on the vacuum H_+ branch,

$$\phi = 1 - C, \;\; \pi = \pi, \;\; H = -\frac{\pi}{\phi}, \tag{4.52}$$

and on the vacuum H_- branch,

$$\phi = 1 - C, \;\; \pi = \pi, \;\; H = 0. \tag{4.53}$$

The vacuum H_+ and H_- branches are obtained from the constraint equation (4.11) by setting $\rho_m = \rho_r = 0$:

$$H_\pm = \frac{1}{2}\left[-\frac{\pi}{\phi} \pm \sqrt{\left(\frac{\pi}{\phi}\right)^2 - \frac{2(f - \phi R)}{3\phi}}\right].$$

The line given by Eq. (4.53) is a critical saddle line. With Eqs. (4.7)-(4.11) and (4.51), one can see that, on this line, $\dot{\pi} = \dot{H} = 0$. Consequently, $\dot{H}_P$ is equal to zero on the transformed line in the compactified phase space $\{\phi_P, \pi_P, H_P\}$. The critical line is the bottom of the $H_P \geq 0$ branch of the vacuum constraint surface. The corresponding critical line on the $H_P \leq 0$ branch is the top of that branch. These two lines are connected by point E, for which $(\phi = 1-C, \pi = 0, H = 0)$. At this point, $\dot{\phi} = \dot{\pi} = \dot{H} = 0$, and then $\dot{\phi}_P = \dot{\pi}_P = \dot{H}_P = 0$. Point E is a critical saddle point, as shown in Figs. 4.7 and 4.8. Moreover, point E is also the only point connecting the two branches of $H_P \geq 0$ and $H_P \leq 0$ of the vacuum constraint surface, as shown in Fig. 4.8. The combined critical line is shown by a solid (magenta) line in Fig. 4.9(f).

The dynamics on the constraint surface of $H_P < 0$ can be explored in a similar way, and is omitted.

4.6.2 Phase-space dynamics in the presence of matter

Some typical slices for the vector fields of $\{\dot{\phi}_P, \dot{\pi}_P\}$ with H_P taking different values in the presence of matter are shown in Fig. 4.9. In the case of $\rho_m > 0$, the phase flows in the Hu-Sawicki model move similarly to those in the $R \ln R$ model. Specifically, the flows start from point A, and end at point D. However, in the case of $\rho_m < 0$, there is a difference between the two models as discussed below.

In the Hu-Sawicki model, when $H = H_P = 0$, Eq. (4.9) becomes

$$\dot{H} = \frac{R}{6} = \frac{\Lambda}{6}\left[\sqrt{\frac{C}{1-f'}} - 1\right] = \begin{cases} > 0 & \text{if } f' > 1 - C, \\ < 0 & \text{if } f' < 1 - C. \end{cases} \tag{4.54}$$

Consequently, on the whole slice of $H_P = 0$, $\dot{H}_P$ is positive at some places, and negative at other places, which is also shown in Fig. 4.9(f). Therefore, i) some flows from the repeller point A will terminate at the attractor point D as in the case of $\rho_m > 0$; ii) some flows will connect the repeller point D' to the attractor point D; iii) some other flows will cross the plane of $H_P = 0$, and end at the attractor point $C'(\phi_P = 0^+, \phi_P = -1, H_P = -1)$. These are shown in Fig. 4.10. The case iii) is different from the $R \ln R$ model, in which the phase flows do not move from the $H_P > 0$ space into the $H_P < 0$ space.

The phase-space dynamics of the modified logarithmic model given by Eq. (4.46), the

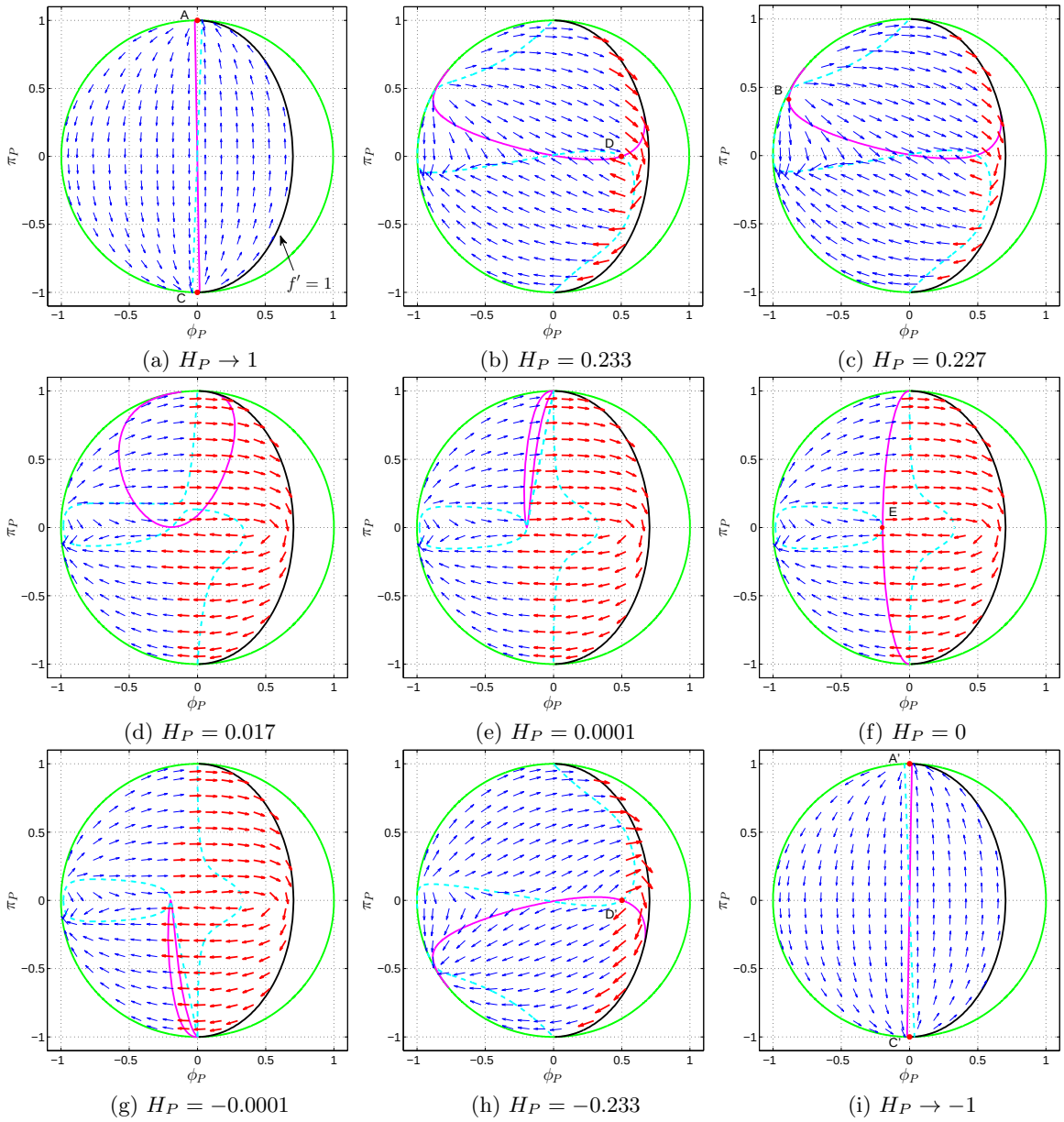

(a) $H_P \to 1$ (b) $H_P = 0.233$ (c) $H_P = 0.227$

(d) $H_P = 0.017$ (e) $H_P = 0.0001$ (f) $H_P = 0$

(g) $H_P = -0.0001$ (h) $H_P = -0.233$ (i) $H_P \to -1$

Figure 4.9: Phase flows on the slices of $H_P =$ const for the Hu-Sawicki model, with $C = 1.2$ and $R_0 = 1$. The thinner (blue) arrows denote that $\dot{H}_P < 0$. The thicker (red) arrows are for $\dot{H}_P > 0$. The solid (magenta) line is the intersection between the two-dimensional constraint surface and the slice of $H_P =$ const. The dashed (cyan) line is the trace of $\dot{\pi}_P = 0$. The solid (black) line is defined by $\phi \equiv f' = 1$. In (a), point A is a repeller and Point C is a saddle point. In (b), point D is an attractor. In (c), point B is a saddle point. In (f), point E is a saddle point and the solid (magenta) line is a critical saddle line. In (h), point D' is a repeller. In (i), point A' is a saddle point and point C' is an attractor.

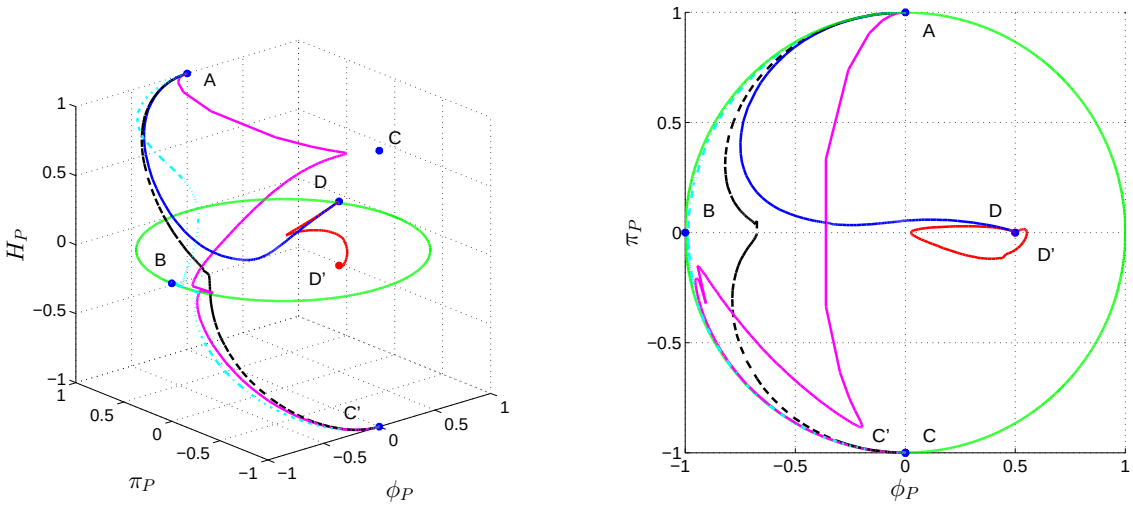

(a) Trajectories with $\rho_m < 0$ (b) Top view

Figure 4.10: Some typical trajectories of the phase flows with $\rho_m < 0$ for the Hu-Sawicki model. The trajectory marked as a (blue) solid line originates from point A, and terminates at point D. The trajectories of the (cyan) dash-dot, (black) dashed, and (magenta) solid lines start from point A, and end at point C'. The flow of the (red) solid line starts from point D', and ends at point D.

exponential model given by Eq. (4.55) (below),[9,40,48,94] and the Tsujikawa (hyperbolic tangent) model given by Eq. (4.56) (below)[130] are also analyzed:

$$f(R) = R - b\left[c - \exp\left(-\frac{R}{R_0}\right)\right], \tag{4.55}$$

$$f(R) = R - b\tanh\left(\frac{R}{R_0}\right). \tag{4.56}$$

In Eqs. (4.55) and (4.56), b, c, and R_0 are constants. When the models have a de Sitter attractor with the parameters taking appropriate values, the phase-space dynamics is similar to that of the Hu-Sawicki model. The noticeable differences are given below. In the modified logarithmic model,

$$f' = 1 - \frac{b}{1+\ln(R/R_0)} + \frac{b}{[1+\ln(R/R_0)]^2} \geq 1 - \frac{b}{4}.$$

Therefore, the left boundary of $\phi \equiv f'$ in the phase space of $\{\phi, \pi, H\}$ is constrained by $\phi \geq 1 - b/4$. In the Tsujikawa model described by Eq. (4.56), the left boundary of ϕ in the

phase space of $\{\phi, \pi, H\}$ is constrained by

$$\phi \equiv f' = 1 - \frac{b}{R_0}\text{sech}^2\left(\frac{R}{R_0}\right) \geq 1 - \frac{b}{R_0}.$$

A critical point, labeled as E and at which $f(R) = R = 0$, is present in the Hu-Sawicki model. However, a similar point is absent in the modified logarithmic model described by Eq. (4.46) and the exponential model described by Eq. (4.55). This occurs because in the modified logarithmic model the Ricci scalar R cannot be zero due to the logarithmic function shown in $f(R)$ and f' of this model, and in the exponential model $f(R)|_{R=0} = -b \cdot c \neq 0$.

4.6.3 Cosmological evolution

In Sec. 4.3, the conditions for the existence of a matter domination epoch in the early Universe for $f(R)$ gravity were explored. These conditions can be expressed such that the corrections should be less than the main terms at three orders of derivative with respect to the Ricci scalar R. Namely, if we rewrite the function $f(R)$ as $f(R) = R + A(R)$, with $A(R)$ being the modification term, we will have

$$|A(R)| \ll R, \quad |A'(R)| \ll 1, \quad A''(R) \ll \frac{1}{R}. \tag{4.57}$$

We can now compare the cosmological evolution of the $f(R)$ models discussed above with the results of Eq. (4.57).

For the $R\ln R$ model expressed by Eq. (4.33), we have

$$A''(R) = \frac{\alpha_0}{R}.$$

Under the balance of general relativity restoration in the early Universe and dark energy domination in the late Universe, a value around 0.02 is chosen for α_0. In this case, $A'(R)$ does not run slowly enough with respect to R to ensure an ideal matter domination epoch. For the modified logarithmic model (4.46), we have

$$A''(R) = \frac{b}{R}\left\{\frac{1}{[1+\ln(R/R_0)]^2} - \frac{2}{[1+\ln(R/R_0)]^3}\right\}.$$

Therefore, in the early Universe where R is much greater than R_0, $A''(R)$ in this model runs more slowly than the one in the $R\ln R$ model, and hence has a better cosmological evolution, as shown in Ref.[66] The ΛCDM-like models (e.g., the Hu-Sawicki model) are very

close to the ΛCDM model at high redshift. At low redshift, the modification term in the function $f(R)$ becomes important, and the dark energy is dominant enough to drive the cosmic acceleration. In one of the simplest versions of the Hu-Sawicki model (4.47),

$$A''(R) = \frac{2CR_0}{(R+R_0)^3} \ll \frac{1}{R}, \quad \text{when } R \gg R_0.$$

Therefore, $A'(R)$ moves more slowly with respect to R than the one in the modified logarithmic model. Consequently, models of this type better fit the cosmological observations in both the early and late Universe. The exponential model (4.55) and Tsujikawa (hyperbolic tangent) model (4.56) are similar in terms of $A''(R)$ to the Hu-Sawicki model, and they have similar cosmological evolution as well.[9]

4.7 Conclusions

In this chapter, we studied cosmological evolution in $f(R)$ gravity, and obtained the cosmological viability conditions by using the scalar field description of $f(R)$ gravity. In the early Universe, the field $\phi(\equiv f')$ is coupled to the matter density, acquiring a mass from this coupling. It has a slow-roll evolution. Consequently, general relativity is recovered, and a matter domination stage is ensured in the early Universe. In the late Universe, when the scalar curvature is around the cosmological constant scale, the field ϕ will be released from its coupling to the matter density and approach the de Sitter minimum of the potential $V(\phi)$. Then, the dark energy will be dominant and drive the cosmic speed-up.

Phase-space dynamics and cosmological evolution of the $R\ln R$ model and Hu-Sawicki model were studied in detail. The $R\ln R$ model has the feature of being singularity-free, which is an advantage in terms of the hierarchy problem between the cosmological acceleration scale and the Planck scale. On the other hand, in this model, general relativity can only be restored at a certain high-curvature scale due to the logarithmic running of f' with respect to the matter density. Therefore, it is hard for this model to have a sensible cosmological evolution in the early Universe. The Hu-Sawicki model is very close to the ΛCDM model, and can generate a cosmological evolution compatible with the observations of both the early and late Universe.

In our explorations of phase-space dynamics, for simplicity, the radiation density was set to zero. In order to obtain a global picture of the phase space, we compactified the infinite phase space into a finite space via the Poincaré transformation. The $R\ln R$ model

and Hu-Sawicki model have similar phase-space dynamics. In the vacuum case where the matter density is zero, the phase space is three-dimensional, and the constraint surface is two-dimensional. The phase-space dynamics was explored in the three-dimensional phase space $\{\phi, \pi, H\}$ without difficulty. On the expansion branch of the phase space, the constraint surface has a repeller and a de Sitter attractor. On the contraction branch, the constraint surface has an attractor and a de Sitter repeller. When the matter density is not zero, the phase space $\{\phi, \pi, H, a\}$ is four-dimensional, and the constraint surface is three-dimensional. For ease of visualization, we projected the four-dimensional phase space $\{\phi, \pi, H, a\}$ onto the three-dimensional phase space $\{\phi, \pi, H\}$ by taking the scale factor a as an implicit variable. It is not convenient to study the phase-space dynamics on the three-dimensional constraint surface directly. Instead, we cut the three-dimensional surface into two-dimensional slices of $H_P = \text{const}$, and explored the vector fields of the phase flows on the slices.

As a supplement, we plotted some typical trajectories of the phase flows. When the matter density is not zero, the constraint surface has the same repellers and attractors as in the vacuum case. Some trajectories between the repeller and the attractor are similar to those in the vacuum case, while some others are not. We also explored the phase-space dynamics of some other $f(R)$ models, such as the modified logarithmic model, the exponential model, and the Tsujikawa model. The results are similar to those of the Hu-Sawicki model.

We presented some generic features of the phase-space dynamics in $f(R)$ gravity in this chapter. We developed new techniques to explore the phase-space dynamics. These techniques are very general and can be applied to other similar dynamical systems.

4.8 Appendix: classification of critical points in a dynamical system

In this Appendix, we briefly discuss how to classify the critical points. Take a two-dimensional autonomous system as an example.

$$\dot{x} = f(x, y), \quad \dot{y} = g(x, y),$$

where the dot $(\cdot)$ denotes time derivative. Assume (x_c, y_c) is a critical point for this system. Namely, at this point, $\dot{x} = \dot{y} = 0$. Consider a small perturbation around this point.

$$x = x_c + \delta x, \;\; y = y_c + \delta y.$$

Then we have

$$\frac{d}{dt}\begin{pmatrix} \delta x \\ \delta y \end{pmatrix} = M \begin{pmatrix} \delta x \\ \delta y \end{pmatrix}, \tag{4.58}$$

where

$$M = \begin{pmatrix} \frac{\partial f}{\partial x} & \frac{\partial f}{\partial y} \\ \frac{\partial g}{\partial x} & \frac{\partial g}{\partial y} \end{pmatrix}. \tag{4.59}$$

We denote λ_1 and λ_2 as the two eigenvalues of the matrix M. Then the solutions to the above equation are

$$\delta x = C_1 e^{\lambda_1 t} + C_2 e^{\lambda_2 t}, \;\; \delta y = C_3 e^{\lambda_1 t} + C_4 e^{\lambda_2 t}.$$

With the above equation, the stability of the critical point can be stated as follows. If the eigenvalues are real and distinct, the critical point is either a node or a saddle.

- It is a stable node (attractor) when $\lambda_1 < 0$ and $\lambda_2 < 0$.
- It is an unstable node (repeller) when $\lambda_1 > 0$ and $\lambda_2 > 0$.
- It is a saddle point when $\lambda_1 \cdot \lambda_2 < 0$.

If the eigenvalues are complex numbers in the form of $\alpha \pm \beta i$, the critical point will be a spiral point or a centre.

- It is a stable spiral point (attractor) when $\alpha < 0$.
- It is an unstable spiral point (repeller) when $\alpha > 0$.
- It is center when $\alpha = 0$.

If the eigenvalues are real and repeated, then the critical point is either a star or an improper node. In the case of improper node, trajectories are tangential to the sole eigenvector.[147]

Chapter 5

Solar System tests of $f(R)$ gravity

In this chapter, we discuss the Solar System tests of $f(R)$ gravity. When the Sun sits in a vacuum background, the field f' is light, which leads to a metric different from the observations. We reobtain this result in a simpler way by directly focusing on the equations of motion for $f(R)$ gravity in the Jordan frame. The discrepancy between the metric in $f(R)$ gravity and the observations can be alleviated by the chameleon mechanism. The implications of the chameleon mechanism for the form of the function $f(R)$ are discussed. Considering the analogy of the Solar System tests to the false vacuum decay problem, the effective potentials in different cases are also explored. A combination of analytic and numerical approaches enables us to ascertain whether an $f(R)$ model can pass the Solar System tests or not. This chapter is mainly based on Ref.[66]

5.1 Introduction

A viable $f(R)$ model should generate cosmic dynamics compatible with the cosmological observations, and also pass the Solar System tests, which place strong constraints on $f(R)$ gravity. The metric for the spherical spacetime for the Sun predicted by general relativity matches well with the observations. General relativity predicts that the parameterized post-Newtonian (PPN) parameter γ should be equal to 1, and the observational results show that $\gamma = 1 + O(10^{-4})$.[21,119,144] Therefore, general relativity should be recovered from $f(R)$ gravity in the Solar System. However, if the Sun sits in a vacuum, the scalar field f' will be very light, which will generate a metric considerably different from the observations. In

this chapter, we rederive this result in a simpler way by directly considering the equations of motion for $f(R)$ gravity in the Jordan frame.

General relativity could be recovered through the chameleon mechanism. In this mechanism, the scalar field f' is coupled to the matter density of the environment. f' acquires a mass from the coupling, and then is suppressed by the mass, such that $f(R)$ gravity can pass the Solar System tests. The chameleon mechanism is usually implemented in the Einstein frame, in which the condition on the existence of a thin shell is obtained in Refs.[84,85] However, the matter density and the transformed scalar field are coupled in a complex way in the Einstein frame. Note that $f(R)$ gravity is defined in the Jordan frame, and the picture is more intuitive in the Jordan frame, in which the coupling between the matter density and the scalar field f' has a much simpler form than in the Einstein frame. In this chapter, we discuss the chameleon mechanism in the Jordan frame, and also explore the implications of this mechanism for the form of the function $f(R)$.

In addition to analytical methods, a numerical approach provides another efficient way to study how the scalar field f' behaves in the effective potential. Taking the $R\ln R$ and Hu-Sawicki models as examples, we run the numerical experiments solving the equation of motion for f' in different configurations. The results verify the arguments for the thin-shell condition obtained in the Jordan frame and the thin-wall approximation condition in the false-vacuum decay scenario, and further clarify whether an $f(R)$ model can avoid the Solar System tests or not.

This chapter is organized as follows. In Sec. 5.2, we introduce the framework of the Solar System tests of $f(R)$ gravity. In Sec. 5.3, a case where the Sun sits in a vacuum background is discussed. In Sec. 5.4, working in the Jordan frame, we explore the chameleon mechanism, and its implications for the form of $f(R)$. In Sec. 5.5, the false-vacuum decay scenario is discussed. In Sec. 5.6, numerical computations are performed to verify the thin-shell condition. In Sec. 5.7, the results are summarized.

5.2 Framework

5.2.1 Basic equations

As discussed in Chapter 2, the equation of motion for $f' \equiv \phi$ is

$$\Box\phi = V'(\phi) + \frac{8\pi G}{3}T, \tag{5.1}$$

where

$$V'(\phi) \equiv \frac{dV}{d\phi} = \frac{1}{3}(2f - \phi R). \tag{5.2}$$

The spherically symmetric coordinate system inside and outside the Sun is set up as

$$ds^2 = -N(r)dt^2 + \frac{1}{B(r)}dr^2 + r^2 d\theta^2 + r^2 \sin^2\theta d^2\phi, \tag{5.3}$$

where r is the radius. In these coordinates, the equations of motion for $f(R)$ gravity[88] are

$$\frac{\phi}{r^2}(-1 + B + rB') = -8\pi G\rho - \frac{1}{2}(\phi R - f) - B\left[\phi'' + \left(\frac{2}{r} + \frac{B'}{2B}\right)\phi'\right], \tag{5.4}$$

$$\frac{\phi}{r^2}\left(-1 + B + rB\frac{N'}{N}\right) = 8\pi G p - \frac{1}{2}(\phi R - f) - B\left(\frac{2}{r} + \frac{N'}{2N}\right)\phi', \tag{5.5}$$

where the prime $(')$ denotes the derivative with respect to r, ρ is matter density, and p is pressure. The trace equation in the coordinate system described by Eq. (5.3) reads

$$B\left[\phi'' + \left(\frac{2}{r} + \frac{B'}{2B} + \frac{N'}{2N}\right)\phi'\right] = \frac{8\pi G}{3}(-\rho + 3p) + V'(\phi). \tag{5.6}$$

When the gravitational field is weak and $\rho \gg p$, Eq. (5.6) can be approximated as

$$\phi'' + \frac{2}{r}\phi' = -\frac{8\pi G}{3}\rho + V'(\phi). \tag{5.7}$$

The boundary conditions are

$$\phi(r)|_{r=\infty} = \text{Const}, \qquad \left.\frac{d\phi}{dr}\right|_{r=0} = 0. \tag{5.8}$$

We will use the above formulas to explore the behaviors of $f(R)$ gravity in the Solar System, and compare the theoretical results with the observations in the PPN formalism.

5.2.2 Parameterized post-Newtonian formalism

Generally, isotropic coordinates are used in the PPN formalism,[19,34,143] while it is convenient to express the metric outside the Sun in the spherical coordinates[138]

$$ds^2 = -\left[1 - 2\alpha\frac{GM}{r} + 2(\beta - \alpha\gamma)\left(\frac{GM}{r}\right)^2\right]dt^2 + \left(1 + 2\gamma\frac{GM}{r}\right)dr^2 + r^2 d\Omega^2, \tag{5.9}$$

where α, β, and γ are PPN parameters, and M is the solar mass. In general relativity, $\alpha = \beta = \gamma = 1$, and the prediction of $\alpha = 1$ follows from the empirical definition of the mass M. A centripetal acceleration for a slowly moving particle far from the center of the Sun is

$$-g = -\Gamma^r_{tt} = \frac{1}{2}\frac{\partial g_{tt}}{\partial r} = -\frac{\alpha GM}{r^2}, \tag{5.10}$$

and the solar mass is measured by setting g to MG/r^2. Therefore, we must set α to 1.[138] Then we can rewrite Eq. (5.9), to the first order of MG/r, as

$$ds^2 = -\left(1 - \frac{2GM}{r}\right)dt^2 + \left(1 + \gamma\frac{2GM}{r}\right)dr^2 + r^2 d\Omega^2. \tag{5.11}$$

A light pulse will be deflected by the Sun when it travels around the Sun. We denote d as the closest distance between the light pulse and the center of the Sun. Then, to the first order of MG/d, the deflection angle for the metric Eq. (5.11) can be expressed as[138]

$$\delta\theta = \left(\frac{1+\gamma}{2}\right)\frac{4M}{d}, \tag{5.12}$$

which is the same as the one derived in isotropic coordinates.[143] In general relativity, γ is equal to 1 and then the deflection angle $\delta\theta_{\mathsf{GR}}$ is equal to $4M/d$. The results from VLBI (very-long-baseline radio interferometry) observations show that $\gamma - 1 = (-1.7 \pm 4.5) \times 10^{-4}$.[119,144]

5.3 The metric for the Sun sitting in a vacuum background

5.3.1 The metric

In $f(R)$ gravity, if we assume that the Sun sits in a vacuum, the metric outside the Sun is dramatically different from the observations. In Refs.,[34,49,72,79,88,123,145] the metric Eq. (5.29) is obtained by a perturbation method or by transforming $f(R)$ theory from the Jordan frame into the Einstein frame. In this thesis, we will recompute the metric in a simpler way by directly focusing on the equations of motion in the Jordan frame.

We assume that the Sun is sitting in a vacuum, and that in Eq. (5.7) $V'(\phi)$ is negligible in comparison to ϕ'' and $2\phi'/r$. Note that at infinity, ϕ is expected to be close to the de Sitter value ϕ_0, for which $V'(\phi)|_{\phi=\phi_0} = 0$. Then, the solution to Eq. (5.7), inside and outside the Sun, can be written as

$$\phi(r)|_{\mathsf{interior}} \approx \phi_0 + \frac{\epsilon}{2r_0}\left[3 - \left(\frac{r}{r_0}\right)^2\right], \tag{5.13}$$

$$\phi(r)|_{\text{exterior}} \approx \phi_0 + \frac{\epsilon}{r}, \tag{5.14}$$

where $\epsilon = 2GM/3$, and r_0 is the radius of the Sun. When both $(\phi R - f)/2$ and p can be neglected, Eqs. (5.4) and (5.5) become

$$\frac{1}{r^2}(-1 + B + rB') \approx -\frac{2}{3\phi_0} 8\pi G\rho, \tag{5.15}$$

$$\frac{N'}{N} \approx \frac{\frac{\phi}{r^2}(1-B) - \frac{2B}{r}\phi'}{B\left(\frac{\phi}{r} + \frac{\phi'}{2}\right)}. \tag{5.16}$$

Note that Eq. (5.15) differs from the corresponding equation in general relativity only by a factor of $2/(3\phi_0)$. This means that the solutions of $B(r)$ inside and outside the Sun can be written as

$$B|_{\text{interior}} \approx 1 - \frac{2\epsilon_1}{r_0}\left(\frac{r}{r_0}\right)^2, \tag{5.17}$$

$$B(r)|_{\text{exterior}} \approx 1 - \frac{2\epsilon_1}{r}, \tag{5.18}$$

where $\epsilon_1 = 2GM/(3\phi_0)$. Substituting Eqs. (5.13)(5.17) and (5.14)(5.18) into (5.16) yields the solutions for $N(r)$ inside and outside the Sun, respectively,

$$N(r)|_{\text{interior}} \approx \exp\left[\frac{4\epsilon_1}{r_0}\left(\frac{r}{r_0}\right)^2 + C_1\right], \tag{5.19}$$

$$N(r)|_{\text{exterior}} \approx C_2\left(1 - \frac{4\epsilon_1}{r}\right). \tag{5.20}$$

Setting C_2 to 1 and requiring $N(r)$ to be continuous at r equal to r_0, we have

$$N(r)|_{\text{exterior}} \approx 1 - \frac{4\epsilon_1}{r}, \tag{5.21}$$

$$N(r)|_{\text{interior}} \approx 1 - \frac{8\epsilon_1}{r_0} + \frac{4\epsilon_1}{r_0}\left(\frac{r}{r_0}\right)^2. \tag{5.22}$$

In summary,

$$\phi(r) \approx \begin{cases} \phi_0\left\{1 + \frac{\epsilon_1}{2r_0}\left[3 - \left(\frac{r}{r_0}\right)^2\right]\right\} & \text{for } r < r_0, \\ \phi_0\left(1 + \frac{\epsilon_1}{r}\right) & \text{for } r > r_0, \end{cases} \tag{5.23}$$

$$B(r) \approx \begin{cases} 1 - \frac{2\epsilon_1}{r_0}\left(\frac{r}{r_0}\right)^2 & \text{for } r < r_0, \\ \\ 1 - \frac{2\epsilon_1}{r} & \text{for } r > r_0, \end{cases} \tag{5.24}$$

$$N(r) \approx \begin{cases} 1 - \frac{8\epsilon_1}{r_0} + \frac{4\epsilon_1}{r_0}\left(\frac{r}{r_0}\right)^2 & \text{for } r < r_0, \\ \\ 1 - \frac{4\epsilon_1}{r} & \text{for } r > r_0. \end{cases} \tag{5.25}$$

For comparison, we also list the corresponding quantities in general relativity: $\phi(r)$ is always equal to 1 and

$$B_{\mathsf{GR}}(r) \approx \begin{cases} 1 - \frac{3\epsilon}{r_0}\left(\frac{r}{r_0}\right)^2 & \text{for } r < r_0, \\ \\ 1 - \frac{3\epsilon}{r} & \text{for } r > r_0, \end{cases} \tag{5.26}$$

$$N_{\mathsf{GR}}(r) \approx \begin{cases} 1 - \frac{6\epsilon}{r_0} + \frac{3\epsilon}{r_0}\left(\frac{r}{r_0}\right)^2 & \text{for } r < r_0, \\ \\ 1 - \frac{3\epsilon}{r} & \text{for } r > r_0. \end{cases} \tag{5.27}$$

More generally, when the matter density and the radius of the Sun are large enough for some $f(R)$ models, $\phi(r)$ could be almost constant at $0 < r < r_1 < r_0$, therefore $V'(\phi) - 8\pi G\rho/3 \approx 0$. Note that in this case the chameleon mechanism is functioning. At $r_1 < r < r_0$, the field $\phi(r)$ varies with r, $\phi'' + 2\phi'/r = -8\pi G\rho/3 + V'(\phi)$. In this case, the solutions of $B(r)$ and $N(r)$ are a bit more complicated. However, the forms of $\phi(r)$, $B(r)$, and $N(r)$ will not change outside the Sun, except that in the definition of ϵ_1, M is replaced by

$$M_{\mathsf{eff}} \approx 4\pi \int_{r_1}^{r_0} \left[\rho - \frac{3V'(\phi)}{8\pi G}\right] r^2 dr. \tag{5.28}$$

5.3.2 Comparison of theoretical results and observations

Substitution of Eqs. (5.18) and (5.21) into (5.3) yields

$$ds^2 = -\left(1 - \frac{8}{3\phi_0}\frac{GM}{r}\right)dt^2 + \left(1 + \frac{4}{3\phi_0}\frac{GM}{r}\right)dr^2 + r^2 d\Omega^2. \tag{5.29}$$

This result is considerably different from the observations as discussed in Sec. 5.2.2. This difference can be explained as follows. Compared to general relativity, in $f(R)$ gravity,

there is one more degree of freedom f'. Equivalently, an extra force is operating. This force affects the metric and then the trajectory of the light pulse. In the next section, we will discuss the chameleon mechanism, in which the degree of freedom f' is suppressed and therefore $f(R)$ gravity may avoid the Solar System tests.

In Refs.,[19,38] a PPN parameter γ equal to 1 is obtained via a linear perturbation of the metric for $f(R)$ gravity in flat Minkowski space. In some $f(R)$ models, e.g., $f(R) = R+\alpha R^2$, where α is a parameter, the de Sitter curvature [obtained from $V'(\phi) = 0$] is zero and hence the background space can be Minkowski space. However, in the dark energy $f(R)$ gravity, the curvature of the background is not equal to zero, but equal to the cosmological constant. A linearized analysis in the de Sitter space will lead to the metric described by Eq. (5.29).[34,123]

5.4 Chameleon mechanism

5.4.1 Chameleon mechanism in the Einstein frame

The discrepancy between the theoretical results and observations in the Solar System tests of $f(R)$ gravity could be avoided through the chameleon mechanism.[49,50,84,85,123] The $f(R)$ gravity can be transformed into the Einstein frame. The field ϕ is rescaled to $\tilde{\phi} = \sqrt{3/2} m_{\rm pl} \ln \phi$, where $m_{\rm pl}$ is the Planck mass and $8\pi G = m_{\rm pl}^{-2}$. We can consider that the Sun sits in the Solar System background, which has a nonzero matter density. The new field $\tilde{\phi}$ can acquire a mass from its coupling to the matter density of the environment both inside and outside the Sun. The field $\tilde{\phi}$ is suppressed by this mass. In order to avoid the Solar System tests, the field $\tilde{\phi}$ should be suppressed to satisfy[49]

$$\frac{|\tilde{\phi}^{\infty}_{\rm min} - \tilde{\phi}^{c}_{\rm min}|}{\Phi_c} \frac{\sqrt{3/2}}{m_{\rm pl}} \leq 3.5 \times 10^{-5}, \tag{5.30}$$

where $\Phi_c (\approx 10^{-6})$ is the Newtonian potential on the Sun's surface.

5.4.2 Chameleon mechanism in the Jordan frame

We present the chameleon mechanism in the Jordan frame in this section, which has a simpler form than in the Einstein frame. General relativity predicts that γ is equal to 1, which matches the observations very well. By comparing the equations of motion in $f(R)$

gravity, (5.4) and (5.5), with those in general relativity,

$$\frac{1}{r^2}(-1+B+rB')=-8\pi G\rho, \tag{5.31}$$

$$\frac{1}{r^2}\left(-1+B+rB\frac{N'}{N}\right)=8\pi Gp, \tag{5.32}$$

one can see that in order to obtain a γ equal to 1 in $f(R)$ gravity, $f(R)$ gravity should be reduced to general relativity in the Solar System. The corresponding matter density ranges from $\rho\approx\rho_{\text{Sun}}\sim \text{g/cm}^3$ to $\rho\approx\rho_{\text{Solar-System}}\sim 10^{-8}\text{g/cm}^3$,

$$f(R)\approx R, \quad \text{and } f'\approx 1. \tag{5.33}$$

Therefore, with Eq. (5.7), which is the equation of motion for ϕ, we obtain that, from inside the Sun to places far away from the Sun, the following equation should be satisfied,

$$V'(\phi)-\frac{8\pi G}{3}\rho\approx 0. \tag{5.34}$$

As will be discussed in Sections 5.5 and 5.6 and as plotted in Figs. 5.4 to 5.7, when the radius of the Sun/sphere r_0 is large enough and the density of the Sun/sphere is high enough, inside the Sun/sphere, ϕ will stay at the state described by Eq. (5.34), and switch to another state across a thin shell near the boundary. The thin shell is plotted in Fig. 5.1.

Taking the spatial coordinate r in Eq. (5.7) as the "time" coordinate,

$$\ddot{\phi}+\frac{2}{r}\dot{\phi}=-\left[-V'(\phi)+\frac{8\pi G}{3}\rho\right]. \tag{5.35}$$

Then, as shown in Fig. 5.2, points B and C correspond to the respective quasistationary states for the field ϕ outside and inside the Sun, and $|\phi_B-\phi_C|\ll 1$. However, if the matter density of the environment is zero, the field ϕ will move to Point A, and a metric Eq. (5.29) different from the observations will be obtained.

When $\phi'\to 0$ and $\phi''\to 0$, Eqs. (5.4) and (5.5) become

$$\frac{\phi}{r^2}(-1+B+rB')=-8\pi G\rho-\frac{1}{2}(\phi R-f), \tag{5.36}$$

$$\frac{\phi}{r^2}\left(-1+B+rB\frac{N'}{N}\right)=8\pi Gp-\frac{1}{2}(\phi R-f). \tag{5.37}$$

Letting $\eta_1=8\pi G\rho+(\phi R-f)/2$ and $\eta_2=-8\pi Gp+(\phi R-f)/2$, we obtain

$$B(r)\approx 1+\frac{C_1}{r}-\frac{\eta_1}{3}r^2, \tag{5.38}$$

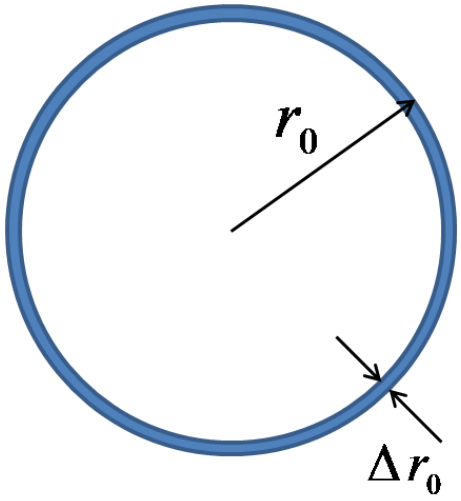

Figure 5.1: Thin shell. When the radius of the Sun/sphere r_0 is large enough and the density of the Sun/sphere is high enough, inside the Sun/sphere, ϕ will stay at the state described by $V'(\phi) - 8\pi G\rho/3 \approx 0$, and switch to another state across a thin shell Δr_0 near the boundary.

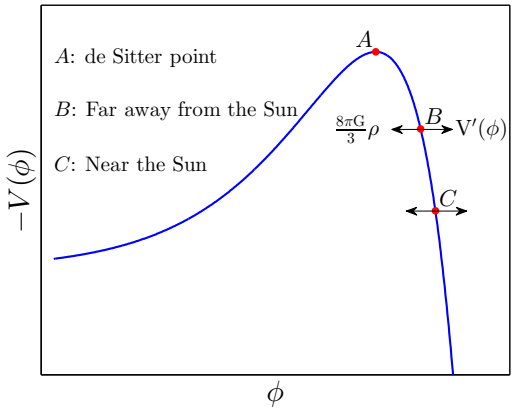

Figure 5.2: Description of the chameleon mechanism in the Jordan frame.

$$N(r) \approx C_2 \exp\left[-\int \frac{C_1/r^2 + (\eta_2 - \eta_1/3)r}{1 + C_1/r - \eta_1 r^2/3} dr\right]. \tag{5.39}$$

When $\eta_1 r \ll C_1/r^2$ and $\eta_2 r \ll C_1/r^2$, one obtains

$$B(r) \approx N(r) \approx 1 + \frac{C_1}{r}, \tag{5.40}$$

and $\gamma \approx 1$.

5.4.3 Requirements on the form of the function $f(R)$

The requirements on the fields $\tilde{\phi}$ and ϕ to pass the Solar System tests have been discussed in the above two subsections. In this subsection, we study the implications of these requirements on the form of the function $f(R)$.

Consider a small variation of Eq. (5.34):

$$V''(\phi) \cdot \delta\phi \approx \frac{8\pi G}{3}\delta\rho. \tag{5.41}$$

As discussed in the above subsection, when general relativity is restored, we have $R \approx 8\pi G\rho_m$ and $|\delta\phi| \ll 1$. These together with Eq. (5.41) imply that

$$|\delta\phi| \approx \frac{8\pi G}{3}\frac{|\delta\rho|}{|V''(\phi)|} \sim \frac{R}{|V''(\phi)|} \ll 1. \tag{5.42}$$

With Eq. (5.2) defining $V'(\phi)$, we have

$$V''(\phi) = \frac{f' - f''R}{3f''}. \tag{5.43}$$

Substitution of Eq. (5.43) into Eq. (5.42) yields that

$$f' \gg f''R. \tag{5.44}$$

Equation (5.44) can be interpreted as follows. We write the function $f(R)$ as

$$f(R) = R + A(R), \tag{5.45}$$

where R is the main term and $A(R)$ is the modification term. Then Eqs. (5.33) and (5.44) imply that the corrections should be smaller than the main terms at three orders of derivative:

$$|A(R)| \ll R, \quad |A'(R)| \ll 1, \quad A''(R) \ll \frac{1}{R}. \tag{5.46}$$

If general relativity is restored inside the Sun, there should be $|A(R)| \ll R$ and $|A'(R)| \ll 1$. To guarantee that general relativity recovery is valid from inside the Sun to places far away from the Sun, $A'(R)$ should also change considerably slowly with respect to R, and Eq. (5.44) shows that the change should be slower than $1/R$.

In addition to the Solar System tests, $f(R)$ gravity should also be reduced to general relativity in the early Universe so that large-scale structure can be formed. Therefore, the recovery requirements on the $f(R)$ form in the two cases are essentially same. The derivation of Eq. (5.46) is very similar to the corresponding one in the study of cosmological evolution, as was discussed in Chapter 4. On the other hand, $f(R)$ gravity should deviate from general relativity at the low-curvature scale, so that a cosmic acceleration can be generated in the late Universe. Therefore, the parameters in $f(R)$ models should take appropriate values to balance the requirements from both high and low-curvature scales.

5.5 False vacuum decay and Solar System tests of $f(R)$ gravity

From the mathematical point of view, the Solar System tests of $f(R)$ gravity are very similar to the false vacuum decay discussed in Ref.[41] The conclusions in Ref.[41] provide a pictorial description of the thin shell problem in $f(R)$ gravity. In this section, we first briefly introduce the scenario of false vacuum decay, then discuss the Solar System tests of $f(R)$ gravity using the arguments of this scenario.

5.5.1 False vacuum decay

Consider a single scalar field in four-dimensional spacetime

$$\mathcal{L} = \frac{1}{2}\partial_\mu\phi\partial^\mu\phi - U(\phi). \tag{5.47}$$

Let U possess two relative minima, $\phi_\pm$, only ϕ_- is an absolute minimum as shown in Fig. 5.3. Assume the energy difference between the two minima, ζ, is tiny, and denote U_{max} as the local maximum of U in the first order of ζ. If ϕ stays at the minimum ϕ_+ initially, quantum effects can make ϕ penetrate the barrier and approach ϕ_-. Thus, ϕ_+ is called a false vacuum. The Euclidian (imaginary-time) equation of motion for ϕ is

$$\left(\frac{\partial^2}{\partial\tau^2} + \nabla^2\right)\phi = U'(\phi), \tag{5.48}$$

where $\tau = it$, and the prime denotes differentiation with respect to ϕ. Define $\rho = (\tau^2 + |\boldsymbol{x}|^2)^{1/2}$. Then, in the three-dimensional spherical symmetry case, Eq. (5.48) becomes

$$\frac{d^2\phi}{d\rho^2} + \frac{3}{\rho}\frac{d\phi}{d\rho} = U'(\phi). \tag{5.49}$$

The boundary conditions are set as

$$\phi(\rho)|_{\rho=+\infty} = \phi_+, \quad \left.\frac{d\phi}{d\rho}\right|_{\rho=0} = 0. \tag{5.50}$$

Equation (5.49) can be studied in the language of classical mechanics. Taking ρ as the "time" variable, the field ϕ moves in $-U(\phi)$ as shown in Fig. 5.3(b). Assume ϕ stays very close to ϕ_- initially. Due to friction, ϕ will remain close to ϕ_- until some very long time after. The field will run through the valley quickly, then approach ϕ_+ very slowly. The place where ϕ moves fast is called the thin-wall. The condition for the validity of the thin-wall approximation can be equivalently expressed in the following three forms:[41]

$$\frac{\zeta}{8U_{\text{max}}} \ll 1 \Longleftrightarrow \frac{\Delta a}{a} \ll 1 \Longleftrightarrow \frac{\Delta\left(\mu^2\right)}{\mu^2} \ll 1. \tag{5.51}$$

With the illustration of Fig. 5.3, $\Delta a = |a_+ - a_-|$, $a = (a_+ + a_-)/2$, $\mu^2 = \left[U''(\phi_+) + U''(\phi_-)\right]/2$, and $\Delta\left(\mu^2\right) = |U''(\phi_+) - U''(\phi_-)|$. Next, we will use these results to examine the Solar System tests of $f(R)$ gravity.

5.5.2 Solar System tests of $f(R)$ gravity

It is possible to rewrite Eq. (5.7) as

$$\phi'' + \frac{2}{r}\phi' = V'_{\text{eff}}(\phi), \tag{5.52}$$

where

$$V'_{\text{eff}}(\phi) = -\frac{8\pi G}{3}\rho + V'(\phi). \tag{5.53}$$

The boundary conditions are described by Eq. (5.8). The dynamics of $\phi(r)$ defined by Eqs. (5.7)-(5.8) are almost identical to the scenario of false vacuum decay, except that the spacetime has one dimension less in the former than in the latter.

For convenience, one may take the spatial coordinate as the "time" coordinate, and rewrite Eq. (5.52) in a "dynamical" form

$$\ddot{\phi} + \frac{2}{r}\dot{\phi} = -\left[-V'_{\text{eff}}(\phi)\right], \tag{5.54}$$

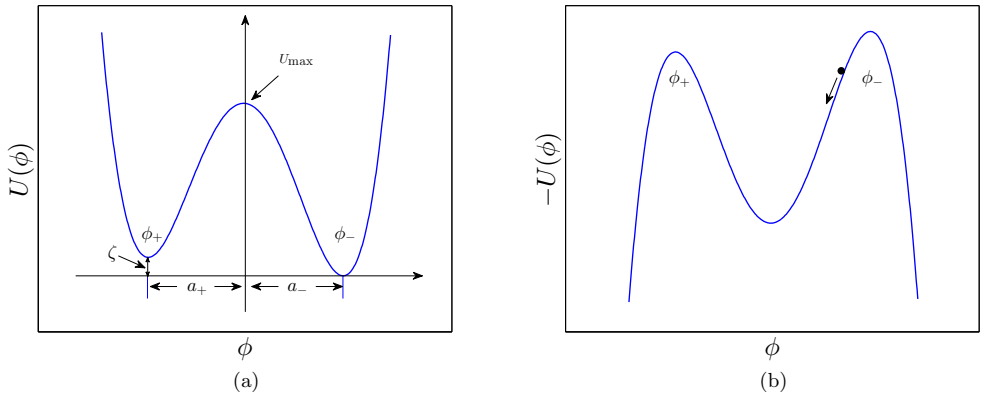

Figure 5.3: Instanton in false vacuum decay. (a) Pictorial description of the thin-wall approximation condition expressed by Eq. (5.51). (b) The inverted potential, $-U(\phi)$. In the beginning, the field ϕ quasistatically stays at the right maximum of the inverted potential for a long "time" due to the large friction force $2\dot{\phi}/r$. Then, after a long "time" (if r is large enough), the friction force becomes negligible, the field ϕ will run through the valley instantly and then slowly approach the left maximum of $-U(\phi)$.

where the overdot still denotes the derivative with respect to the spatial coordinate r. The field ϕ is required to satisfy the boundary conditions described by Eq. (5.8). For $f(R)$ models satisfying the conditions expressed by Eq. (5.46), general relativity can be well restored when the matter density is much greater than the cosmological constant. In this case, the field $\phi(\equiv f')$ is always very close to 1 from inside the Sun to places far away from the Sun, and will have a fast transition between the values inside and outside the Sun. Consequently, the two maxima of $-V_{\text{eff}}$ for these models are almost at the same "height". In the beginning, the field ϕ quasistatically stays at the right maximum of the inverted potential $-V_{\text{eff}}$ for a long "time" due to the large friction force $2\dot{\phi}/r$. Then, after a long "time" (when r is large enough), the friction force becomes negligible such that the field ϕ will run through the valley instantly and then slowly approach the left maximum of $-V_{\text{eff}}$. In this case, ϕ is an instanton, and has a thin shell across the Sun's surface. However, for $f(R)$ models not well satisfying the condition expressed by Eq. (5.46), general relativity may be recovered only for a very short period of matter density, and the field ϕ can deviate significantly from 1 from inside the Sun to places far away from the Sun. Then, a slow transition for the field ϕ between the values inside and outside the Sun will take place. In this case, the two maxima of the effective potential can be quite different. Both the instanton and noninstanton cases will be numerically implemented in the rest of this chapter.

5.6 Numerical computations

In order to verify the analytic arguments in Secs. 5.4 and 5.5, we numerically investigate the profile of $\phi(r)$ for a sphere (including the Sun) sitting in a background with nonzero matter density. When the function $f(R)$ can trace the Ricci scalar R closely enough in the Solar System, the field ϕ will be very close to 1, and has a fast but tiny drop near the surface of the Sun. The two maxima of the effective potential will be almost equally high, and the field ϕ is an instanton across the valley of the effective potential. However, if the function $f(R)$ deviates greatly from the Ricci scalar R in the Solar System, the field ϕ will change significantly from 1 and will have a long-term transition between the values inside and outside the Sun. Consequently, the heights of the two maxima of the effective potential can be very different, and the corresponding $f(R)$ model will have difficulty in passing the Solar System tests. To justify these results, in this section, we will numerically explore the behaviors of $\phi(r)$ in the Solar System, taking the $R\ln R$ and Hu-Sawicki models as examples.

5.6.1 Numerical computations for the $R\ln R$ model

We consider the $R\ln R$ model as introduced in Chapter 3,

$$f(R) = R\left(1+\alpha_0 \ln\frac{R}{R_0}\right), \tag{5.55}$$

where α_0 and R_0 are positive constants. For this model, the de Sitter curvature is

$$\Lambda \equiv R_0 e^{-\frac{1}{\alpha_0}+1}. \tag{5.56}$$

The function $f(R)$ can be rewritten as

$$f(R) = R(\phi-\alpha_0), \tag{5.57}$$

with

$$\phi \equiv f' = 1+\alpha_0+\alpha_0\ln\frac{R}{R_0}. \tag{5.58}$$

When ϕ'' and $2\phi'/r$ are negligible compared to $V'(\phi)$ and $8\pi G\rho/3$ in Eq. (5.7), one obtains

$$\phi \approx 2\alpha_0 + \alpha_0 W(X), \tag{5.59}$$

where $X = 8\pi G\rho/\Lambda$, and $W(X)$ is the Lambert W function. Equations (5.57) and (5.59) show that, at the general-relativistic limit, $\phi \approx 1$, $R \sim R_0$, and

$$\alpha_0 \approx \frac{1}{W(X)} \ll 1. \tag{5.60}$$

$W(X) \approx \ln(X)$ when $X \gg 1$. Then, with Eq. (5.59), ϕ is logarithmically dependent on X when $X \gg 1$. This model is therefore reduced to general relativity only for a certain period of curvature or matter density even at the high-curvature scale.

Regarding the low-curvature scale, in order for $f(R)$ gravity to generate a cosmic acceleration in the late Universe, the de Sitter curvature, and hence α_0, cannot be too small. [See Eq. (5.56).] Consequently, an appropriate value for α_0 needs to be chosen to reconcile the tension between the requirements at the high- and low-curvature scales. Under the reconciliation, the running of ϕ makes it hard for the $R \ln R$ model to pass the Solar System tests, as discussed below.

Using Newton's iteration method, we numerically solve Eq. (5.7) to obtain $\phi(r)$ for a sphere (which can be the Sun) in a background with nonzero matter density in different configurations. As far as the units are concerned, in this chapter, we set the parameters to be dimensionless. We set the radius of the Sun r_0 to 1, in which case the densities of the Sun, the Solar System and the dark energy are 2.1×10^{-6}, 6×10^{-14} and 10^{-34}, respectively. We describe the matter density profile around the sphere approximately as

$$\rho = \frac{\rho_{\text{sphere}}}{1 + e^{10(r-r_0)}} + \rho_{\text{background}}. \tag{5.61}$$

For simplicity, we set R_0 to 1. We consider the following three cases in sequence: i) a thin shell of $\phi(r)$ exists, ii) a thick shell of $\phi(r)$ exists, and iii) a solar case, where the field ϕ does not sit at one minimum of $V_{\text{eff}}(\phi)$ inside the Sun, and a shell does not exist.

Generally, a thin-shell solution of $\phi(r)$ could exist, when i) the matter densities of the sphere and the background are high, ii) the gap between the two matter densities is not too large, iii) the sphere is large enough, and iv) and the parameters take appropriate values so that the $f(R)$ model does not deviate much from general relativity at the curvature scale above the one of the background. Take $\alpha_0 = 0.015$ and $R_0 = 1$. Using the same units as those in the Solar System case, we set the matter densities of the sphere and the background to 55 and 5, respectively. The radius of the sphere r_0 is 10. The results for this set of parameters are shown in Fig. 5.4. A thin-shell solution for ϕ exists across the surface of the sphere. [See Fig. 5.4(a).] In this configuration, ϕ stays at the coupling state, for which

$V'(\phi) \approx 8\pi G\rho/3$, from inside to outside the sphere, and the absolute value of the friction force $|2\phi'/r|$ is much less than that of the net force $|\phi''|$, as shown in Figs. 5.4(b) and (c). Consequently, ϕ can instantly cross the valley of $-V_{\text{eff}}(\phi)$ and, as plotted in Fig. 5.4(c), the two maxima of the inverted effective potential $-V_{\text{eff}}$ are almost at the same height, and ϕ is an instanton in $-V_{\text{eff}}$. The potentials, V, V_{eff}, and V_m in Fig. 5.4(c) are defined by Eqs. (5.2), (5.53), and $V_m' = -8\pi G\rho/3$, respectively. Equation (5.53) implies that $V_{\text{eff}} = V + V_m$.

Now we consider a more challenging configuration. Take $\alpha_0 = 0.02$ and $R_0 = 1$. The matter densities of the sphere and the background are 2.1×10^{-1} and 2.1×10^{-5}, respectively. The radius of the sphere r_0 is 5. The results for this set of parameters are shown in Fig. 5.5. As shown in Figs. 5.5(a) and (b), in this situation, at places well inside and far away from the sphere, the field ϕ stays at the coupling state, and the equation of motion for ϕ (5.7) becomes $V'(\phi) - 8\pi G\rho/3 \approx 0$. Near the surface of the sphere, Eq. (5.7) is approximated as $\phi'' + 2\phi'/r \approx 0$. In this case, ϕ has a thick shell. In the meantime, although $-V_{\text{eff}}(\phi)$ still has two maxima, they are not at the same height, as shown in Fig. 5.5(c).

In the above two configurations, inside the sphere, ϕ stays at the coupling state. Then, the scalar field ϕ runs slowly with respect to the matter density. [See Eq. (5.59).] This running can easily trigger the field ϕ to move off the coupling state inside the sphere and then the field ϕ will slowly approach the other coupling state which is far away from the sphere, as shown in Figs. 5.4 and 5.5. The smaller the matter density and the radius of the sphere are, the earlier the field ϕ will be released from the coupling state inside the sphere. In the Solar System case, such a coupling process does not even exist. We let $\alpha_0 = 0.0126$ and $R_0 = 1$ so that Λ can take the value of the dark energy, 10^{-34}. The numerical results in the solar case are shown in Fig. 5.6. Figure 5.6(a) shows that Eq. (5.7) can be approximated as $\phi'' + 2\phi'/r \approx 8\pi G\rho/3$ and $\phi'' + 2\phi'/r \approx 0$ inside and outside the Sun, respectively. As a result, outside the Sun, $\phi(r) \approx \phi_0 + 2GM/(3r)$, where $\phi_0 = 2\alpha_0 + \alpha_0 W(8\pi G\rho_{\text{Solar-System}}/\Lambda)$. Therefore, a metric close to Eq. (5.29), which is different from the observations, will be obtained, similarly to what was discussed in Sec. 5.3.

One may also interpret the results in the solar case in another way. For the $R\ln R$ model,

$$f'' = \frac{\alpha_0}{R}. \tag{5.62}$$

In comparison to the requirement of the general relativity restoration (5.46), the modification term in the $R\ln R$ model changes fast with respect to the Ricci scalar R, and the model deviates significantly from general relativity. Consequently, with Eq. (5.59), there can be

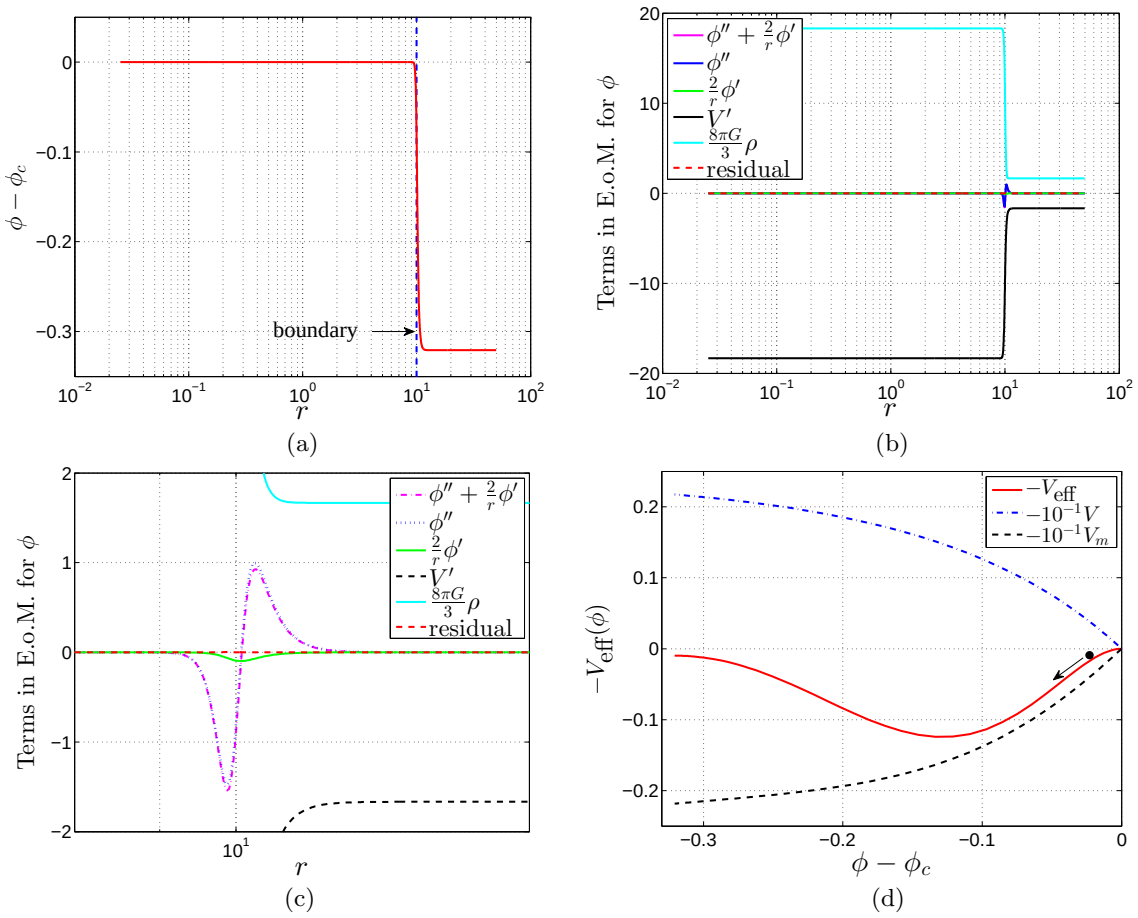

Figure 5.4: Numerical solution for the $R \ln R$ model when the parameters are set up to make the field ϕ heavy. (a) The field $\phi(r)$. $\phi(r)$ is coupled to the matter density from inside to outside the sphere, and a thin shell exists across the surface of the sphere. $\phi_c (= 1.70)$ is the value of ϕ at the center of the sphere. (b) The terms in the equation of motion (E.o.M.) for ϕ (5.7). From inside to outside the sphere, Eq. (5.7) is approximated as $V'(\phi) \approx 8\pi G\rho/3$. The absolute value of the friction force, $|2\phi'/r|$, is much less than that of the net force $|\phi''|$, which allows the field ϕ to cross the valley of $-V_{\rm eff}$ instantly. (c) Zoom-in of (b) near the surface of the sphere. (d) The inverted effective potential $-V_{\rm eff}(\phi)$. The two maxima of $-V_{\rm eff}(\phi)$ are almost at the same height, and $\phi(r)$ is an instanton in $-V_{\rm eff}(\phi)$. $V_{\rm eff} = V + V_m$.

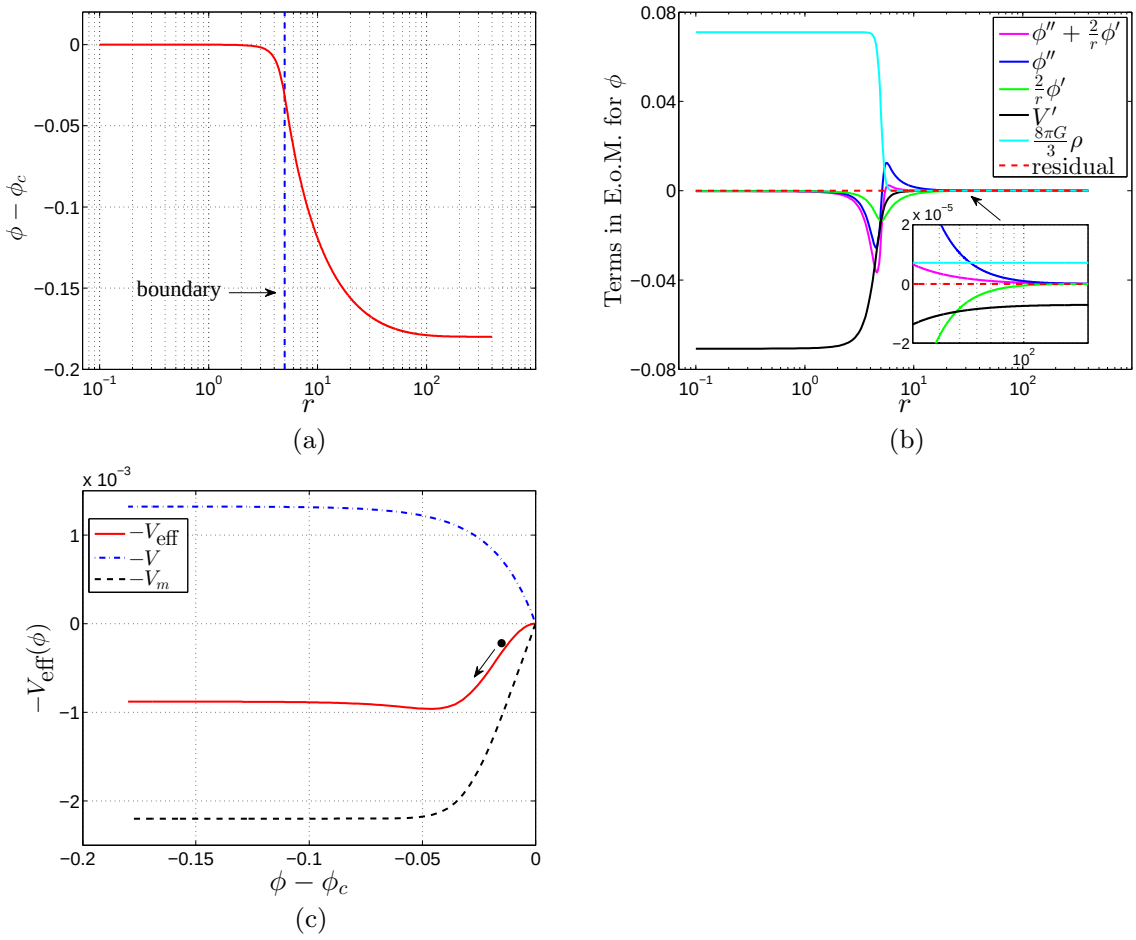

Figure 5.5: Numerical solution for the $R \ln R$ model in an intermediate case. (a) The field $\phi(r)$. At places well inside and far away from the sphere, the field ϕ is coupled to the matter density of the environment. Near the surface of the sphere, the field ϕ is decoupled from the matter density and has a slow rather than instant roll. (In other words, ϕ has a thick shell.) $\phi_c (= 0.99)$ is the value of ϕ at the center of the sphere. (b) The terms in the equation of motion for ϕ (5.7). At places well inside and far away from the sphere, Eq. (5.7) becomes $V'(\phi) - 8\pi G\rho/3 \approx 0$. Just outside the sphere, Eq. (5.7) is approximated as $\phi'' + 2\phi'/r \approx 0$. (c) The inverted effective potential $-V_{\rm eff}(\phi)$. The left maximum of $-V_{\rm eff}(\phi)$ is lower than the right one. A large fraction of potential energy of the field ϕ is exhausted by the friction force in the rolling-down process. $V_{\rm eff} = V + V_m$.

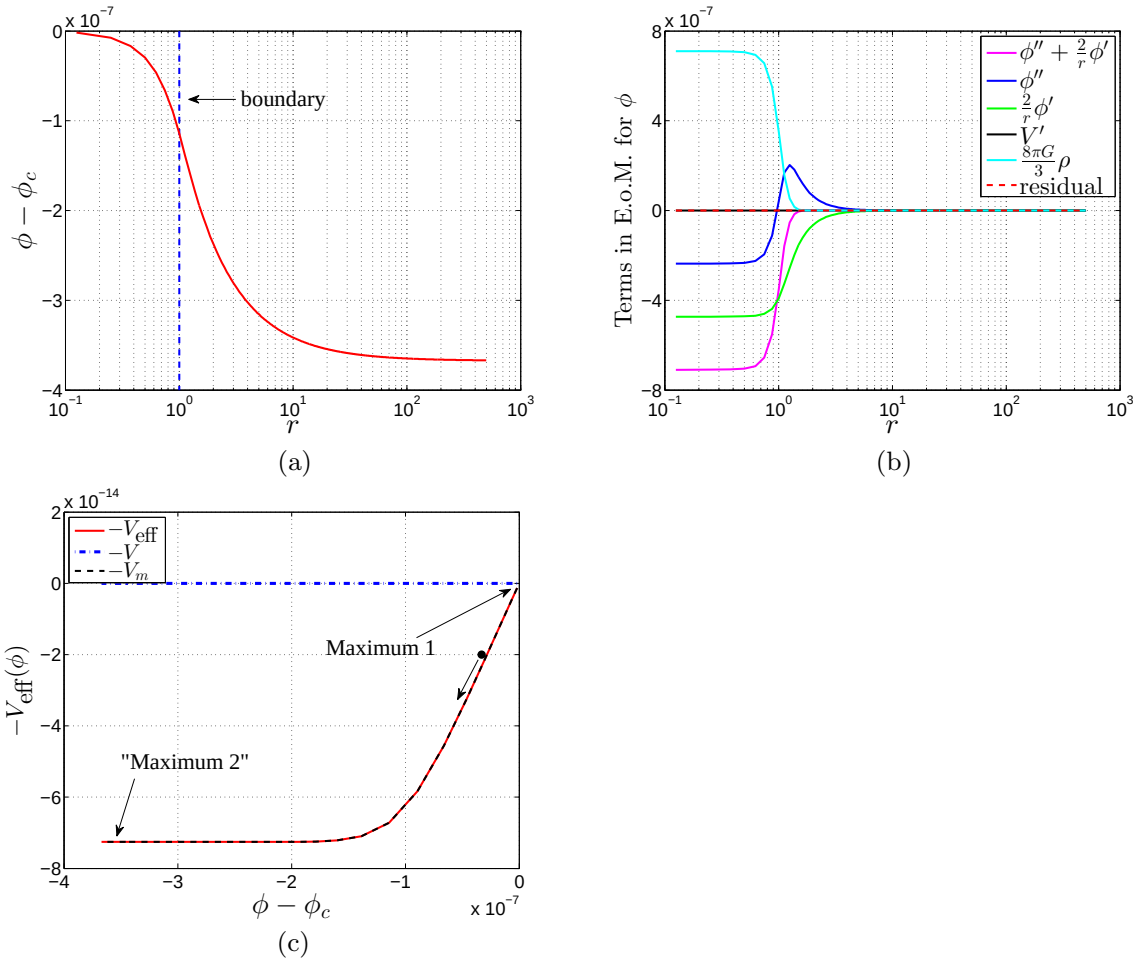

Figure 5.6: Numerical solution for the $R \ln R$ model in the Solar System case. (a) The field $\phi(r)$. In this configuration, $\phi(r)$ is not coupled to the matter density inside the Sun, and then a shell does not exist near the surface of the Sun. $\phi_c (= 0.202555860)$ is the value of ϕ at the center of the Sun. (b) The terms in the equation of motion for ϕ (5.7). The friction force, $2\phi'/r$, is relatively large, and $\phi'' + 2\phi'/r \approx 8\pi G\rho/3$, which leads to a metric Eq. (5.29) different from the observations. (c) The inverted effective potential, $-V_{\rm eff}(\phi)$. The field ϕ slowly rolls down from Maximum 1 to "Maximum 2" due to the large friction force. $V_{\rm eff} = V + V_m$.

a big gap for ϕ between inside and outside the sphere. In the Solar System, outside the Sun, due to the small value of $W(8\pi G\rho_{\text{Solar-System}}/\Lambda)$, the value of ϕ in the coupling state, $V'(\phi) \approx 8\pi G\rho_{\text{Solar-System}}/3$, is very close to its de Sitter value $2\alpha_0$. Then along the radial direction from outside to inside the Sun, because of the big gap between the general relativity restoration value $\phi \approx 1$ and the value close to $\phi_0(= 2\alpha_0)$, ϕ slowly moves toward the general relativity restoration place as the matter density increases. However, because the solar density is not high enough and the Sun is not large enough for the $R\ln R$ model, inside the Sun, the equation of motion for ϕ is reduced to $\phi'' + 2\phi'/r \approx 8\pi G\rho_{\text{Sun}}/3$. In other words, the field ϕ does not even come to the equilibrium point between $V'(\phi)$ and $8\pi G\rho_{\text{Sun}}/3$ as the radius approaches to zero. As a result, Eq. (5.42) does not apply, and $\phi(r)$ does not have a shell across the Sun's surface.

As a supplement, Fig. 5.6(c) shows that the inverted potential, $-V_{\text{eff}}$, has only one rather than two maxima, so ϕ just slowly rather than instantly rolls down from the maximum (inside the Sun) to the minimum (outside the Sun) of the inverted potential, $-V_{\text{eff}}$. In summary, due to the large running of the modification term with respect to the Ricci scalar R, the $R\ln R$ model has difficulty in passing the Solar System tests.

As a result, it remains challenging for the $R\ln R$ model to pass the Solar System tests when the chameleon mechanism has been taken into account. This problem is significantly alleviated in some other $f(R)$ models (e.g., the Hu-Sawicki model) that are close to the ΛCDM model. In these models, the field ϕ is not sensitive to the change in the matter density when the matter density is above the cosmological constant scale.

5.6.2 Numerical computations for the Hu-Sawicki model

We consider the simplest version of the Hu-Sawicki model,[72]

$$f(R) = R - \frac{CR_0R}{R + R_0}, \tag{5.63}$$

where C is a dimensionless parameter, $R_0 = 8\pi G\bar{\rho}_0/3$, and $\bar{\rho}_0$ is the average matter density of the current Universe. In this model,

$$V'(\phi) = \frac{R^3}{3(R + R_0)^2}\left[1 + (1 - C)\frac{R_0}{R}\left(2 + \frac{R_0}{R}\right)\right]. \tag{5.64}$$

The above two equations show that as long as the matter density is much greater than R_0, the curvature R will trace the matter density well, and ϕ will be close to 1.

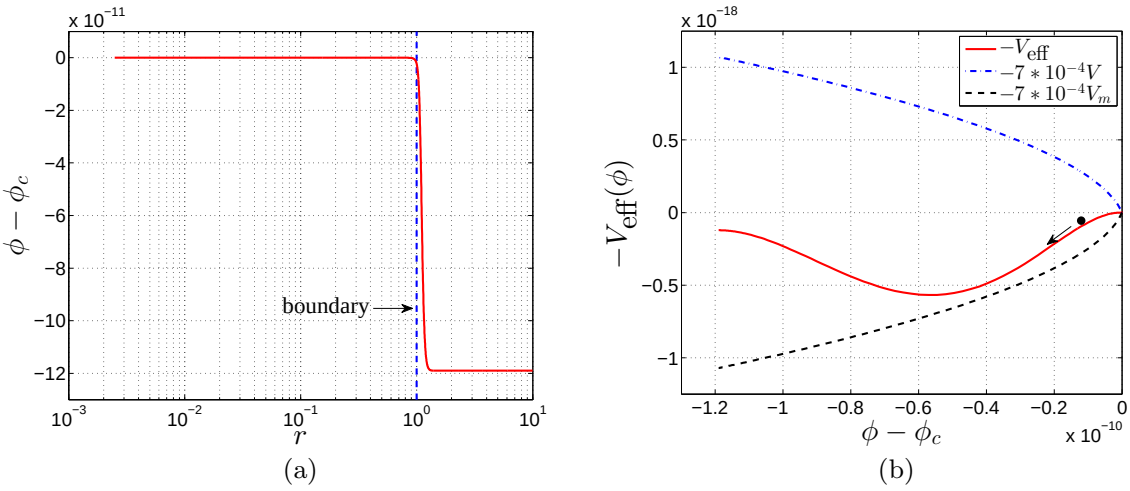

Figure 5.7: Numerical solution for the Hu-Sawicki model described by Eq. (5.63). (a) The field $\phi(r)$. A thin shell exists near the surface of the sphere. $\phi_c (= 1 - 1.188 \times 10^{-14})$ is the value of ϕ at the center of the sphere. (b) The inverted effective potential $-V_{\text{eff}}(\phi)$. The two maxima of $-V_{\text{eff}}(\phi)$ are almost at the same height, and $\phi(r)$ is an instanton in $-V_{\text{eff}}(\phi)$. $V_{\text{eff}} = V + V_m$.

In this model,

$$A''(R) = \frac{2CR_0}{(R+R_0)^3} \ll \frac{1}{R}, \quad \text{when } R \gg R_0$$

where $A(R)$ is the modification term, $f(R) = R + A(R)$. So $A'(R)$ moves very slowly with respect to R in comparison to $1/R$, which makes the Hu-Sawicki model favorable to avoid the Solar System tests. We compute the field $\phi(r)$ when a sphere sits in a background with nonzero matter density, and the parameters take the following values. Equation (5.64) shows that in order for the model to have a de Sitter point for which $V'(\phi) = 0$, the parameter C needs to be greater than 1. In this chapter, we set C to 1.2. In the same set of units as used in the $R \ln R$ case, the radius of the sphere r_0 is equal to 1, and the densities of the sphere, background, and R_0 are 2.1×10^{-4}, $10^{-2}\rho_{\text{sphere}}$, and $10^{-7}\rho_{\text{sphere}}$, respectively. The density profile is

$$\rho = \frac{\rho_{\text{sphere}}}{[1 + \exp(30(r - r_0))]} + \rho_{\text{background}}.$$

The solution for $\phi(r)$ is plotted in Fig. 5.7(a), which shows that $\phi(r)$ has a thin shell near the surface of the sphere. As shown in Fig. 5.7(b), the two maxima of the inverted effective potential are at the same height, and $\phi(r)$ is an instanton in the inverted effective potential.

In principle, when the computational precision is high enough, numerical computations in the solar case can be performed. On the other hand, in this thesis, we only considered a simple case ($n = 1$) of the Hu-Sawicki model (2.43). A case with a larger n will be more favored to pass the Solar System tests because the field ϕ will be more suppressed. However, implementing all such computations is beyond the scope of this thesis.

5.7 Conclusions

Confrontations between $f(R)$ gravity and the Solar System tests were explored in the Jordan frame in this chapter. The metric grossly violates the observations if the Sun is assumed to sit in a vacuum background. We reobtain this result in a simpler way by directly focusing on the equation of motion for $\phi(\equiv f')$ in the Jordan frame.

The chameleon mechanism implies that the function $f(R)$ should be very close to the Ricci scalar R for R above or equal to the Solar System scale. On the other hand, $f(R)$ gravity should deviate from general relativity at the cosmological constant scale, so that a cosmic acceleration can be generated in the late Universe. Therefore, a trade-off between the requirements at the high- and low-curvature scales needs to be made.

We numerically computed the profiles of $\phi(r)$ for a sphere (which can be the Sun) in an environment (which can be the Solar System) with nonzero matter density in different configurations. The corresponding inverted effective potentials were plotted. These provided an intuitive understanding of the effects from the matter density. Regarding the $R\ln R$ model, in the coupling state, the scalar field ϕ runs logarithmically with respect to the matter density when the matter density is much greater than the cosmological constant. This logarithmic relationship can easily trigger the field ϕ to release from the coupling state inside the sphere, and ϕ will then SLOWLY approach the other coupling state, which is far away from the sphere. Consequently, it is challenging for the $R\ln R$ model to pass the Solar System tests. In fact, the coupling state does not even exist inside the Sun for this model. In some other $f(R)$ models which are very close to the ΛCDM model, the field ϕ is robust to the change in the matter density as long as the matter density is greater than the cosmological constant. As a result, this class of $f(R)$ models has the advantage of passing the Solar System tests.

Chapter 6

Spherical collapse in $f(R)$ gravity

Spherical scalar collapse in $f(R)$ gravity is studied numerically in double-null coordinates in the Einstein frame. Dynamics in the vicinity of the singularity of the formed black hole is examined via mesh refinement and asymptotic analysis. Before the collapse, the scalar degree of freedom f' is coupled to a physical scalar field, and general relativity is restored. During the collapse, the major energy of the physical scalar field moves to the center. As a result, f' loses the coupling and becomes light, and gravity transits from general relativity to $f(R)$ gravity. Due to strong gravity from the singularity and the low mass of f', f' will cross the minimum of the potential and approach zero. The static solution for a black hole in $f(R)$ gravity is a de Sitter-Schwarzschild solution. Therefore, the dynamical solution is significantly different from the static one. f' tries to suppress the collapse of the physical scalar field. This is a dark energy effect. As the singularity is approached, the metric terms are dominant over other terms. The Kasner solution for spherical scalar collapse in $f(R)$ theory is obtained and confirmed by numerical results. These results support the Belinskii-Khalatnikov-Lifshitz conjecture well. This chapter is mainly based on Ref.[67]

6.1 Introduction

Black hole physics is an ideal platform from which to study gravity. It connects classical general relativity, semiclassical gravity, and the quantum theory of gravity. It is studied not only in the context of gravitation, but also in astrophysics and cosmology. Moreover, there are profound links between black hole physics, thermodynamics, and information theory.

Historically, some static solutions for black holes have been obtained analytically. The "no-hair" theorem states that a stationary black hole can be described by only a few parameters.[142] Hawking showed that stationary black holes as the final states of Brans-Dicke collapses are identical to those in general relativity.[69] In Ref.,[12] a novel "no-hair" theorem was proven. In this theorem, the scalar field, surrounding an asymptotically flat, static, spherically symmetric black hole, is assumed to be minimally coupled to gravity, and to have a non-negative energy density. In this case, the black hole must be a Schwarzschild black hole. This result is also valid if the scalar field has a potential whose global minimum is zero. The possible black hole solutions were explored in scalar-tensor gravity, including $f(R)$ gravity, by Sotiriou and Faraoni. If black holes are isolated from the cosmological background, they can be shown to have a Schwarzschild solution.[124]

As astrophysical black holes are expected to come from collapses of matter, studying collapse processes, especially spherical collapses, is an instructive way to explore black hole physics and to verify the results on stationary black holes as well. (For reviews of gravitational collapse and spacetime singularities, see Refs.[15,17,70,77,78,81]) The Oppenheimer-Snyder solution offers an analytic description of spherical dust collapse into a Schwarzschild black hole.[100] The Lemaître-Tolman–Bondi solution describes a spherically symmetric inhomogeneous universe filled with dust matter.[23,92,129] However, due to the nonlinearity of the Einstein field equations, in most other cases, the collapse solutions have to be searched for numerically. The simulations of spherical collapse in Brans-Dicke theory were implemented in Refs.,[115,116,118] confirming Hawking's conclusion that stationary black holes as the final states of Brans-Dicke collapses are identical to those in general relativity.[69] In Ref.,[71] numerical integration of the Einstein equations outwards from the horizon was performed. The results strongly supported the new "no-hair" theorem presented in Ref.[12] Recently, the dynamics of single and binary black holes in scalar-tensor theories in the presence of a scalar field was studied in Ref.,[20] in which the potential for scalar-tensor theories is set to zero and the source scalar field is assumed to have a constant gradient.

Although $f(R)$ theory is equivalent to scalar-tensor theories, it is a unique type. In $f(R)$ theory, the potential is related to the function $f(R)$ or the Ricci scalar R by $V'(\chi) \equiv (2f - \chi R)/3$, with $\chi \equiv f'$. In dark-energy-oriented $f(R)$ gravity, the de Sitter curvature obtained from $V'(\chi) \equiv (2f - \chi R)/3 = 0$ is expected to drive the cosmic acceleration. Consequently, the minimum of the potential cannot be zero. Therefore, spherical collapse in $f(R)$ theory

has rich phenomenology and is worth exploring in depth, although some studies have been implemented in scalar-tensor theories. In Ref.,[32] the gravitational collapse of a uniform dust cloud in $f(R)$ gravity was analyzed; the scale factor and the collapsing time were computed. In Ref.,[117] the junction conditions through the hypersurface separating the exterior and the interior of the global gravitational field in $f(R)$ theory were derived. In Ref.,[75] a charged black hole from gravitational collapse in $f(R)$ gravity was obtained. However, to a large extent, a general collapse in scalar-tensor theories (especially in $f(R)$ theory), in which the global minimum of the potential is nonzero, still remains unexplored as of yet. In addition to a black hole formation, large-scale structure is another formation that can be modeled. In Refs.,[10,90] with the scalar fields assumed to be quasistatic, simulations of dark matter halo formation were implemented in $f(R)$ gravity and Galileon gravity, respectively.

Another motivation comes from the study of the dynamics as one approaches the singularity. The Belinskii, Khalatnikov, and Lifshitz (BKL) conjecture states that as the singularity is approached, the dynamical terms will dominate the spatial terms in the Einstein field equations, the metric terms will dominate the matter field terms, and the metric components and the matter fields are described by the Kasner solution.[13,14,82,91,136] The BKL conjecture was verified numerically for the singularity formation in a closed cosmology in Refs.[16,61] It was also confirmed in Ref.[62] with a test scalar field approaching the singularity of a black hole, which is described by a spatially flat dust Friedmann$-$Robertson$-$Walker spacetime. In Ref.,[5] the BKL conjecture in the Hamiltonian framework was examined, in an attempt to understand the implications of the BKL conjecture for loop quantum gravity. In this thesis, we consider a scalar field collapse in $f(R)$ gravity. We study the evolution of the spacetime, the physical scalar field ψ, and the scalar degree of freedom f' throughout the whole collapse process and also near the singularity.

Regarding simulations of gravitational collapses and binary black holes in gravitational theories beyond general relativity, in addition to the references mentioned above, in Ref.,[68] the generation and propagation of the scalar gravitational wave from a spherically symmetric and homogeneous dust collapse in scalar-tensor theories were computed numerically, with the backreaction of the scalar wave on the spacetime being neglected. Scalar gravitational waves generated from stellar radial oscillations in scalar-tensor theories were computed in Ref.[122] The response of the Brans-Dicke field during gravitational collapse was studied in Ref.[73] Charge collapses in dilaton gravity were explored in Refs.[24,55,56] Binary black hole mergers in $f(R)$ theory are simulated in Ref.[28]

We take the Hu-Sawicki model and the Starobinsky model as sample $f(R)$ models. We perform the simulations in the double-null coordinates proposed by Christodoulou.[37] These coordinates have been used widely, because they have the horizon-penetration advantage and also allow us to study the global structure of spacetime.[24,54–56,63,73,74,120] The results show that a black hole can be formed. During the collapse, the scalar field f' is decoupled from the matter density and becomes light. Simultaneously, the Ricci scalar decreases, and the modification term in the function $f(R)$ becomes important. The lightness of f' and the gravity from the scalar sphere, which forms a black hole later, make the scalar field f' cross the minimum of the potential (also called a de Sitter point), and then approach zero near the singularity. The asymptotic expressions for the metric components and scalar fields are obtained. They are the Kasner solution. These results support the BKL conjecture.

To a large extent, the features of $f(R)$ theory are defined by the shape of the potential. Local tests and cosmological dynamics of $f(R)$ theory are closely related to the right side and the minimum area of the potential. In the early Universe, the scalar degree of freedom f' is coupled to the matter density. In the later evolution, f' is decoupled from the matter density and goes down toward the minimum of the potential, and eventually stops at the minimum after some oscillations. Interestingly, the study of the collapse process draws one's attention to the left side of the potential.

The chapter is organized as follows. In Sec. 6.2, we introduce the framework of the collapse, including the formalism of $f(R)$ theory, double-null coordinates, and the Hu-Sawicki model. In Sec. 6.3, we set up the numerical structure, including discretizing the equations of motion, defining initial and boundary conditions, and implementing the numerical tests. In Sec. 6.4, numerical results are presented. In Sec. 6.5, we discuss numerical results from the point of view of the Jordan frame. In Sec. 6.6, we consider collapses in more general models. Section 6.7 summarizes our work.

6.2 Framework

In this section, we build the framework of spherical scalar collapse in $f(R)$ theory. For computational convenience, $f(R)$ gravity is transformed from the Jordan frame into the Einstein frame. In order to study the global structure of the spacetime and the dynamics near the singularity, we simulate the collapse in double-null coordinates. A typical $f(R)$ model, the Hu-Sawicki model, is chosen as an example model.

6.2.1 Formalism in the Einstein frame

As shown in Chapter 2, the second-order derivatives of f' make the field equations in $f(R)$ gravity complex,

$$f'R_{\mu\nu} - \frac{1}{2}fg_{\mu\nu} - (\nabla_\mu\nabla_\nu - g_{\mu\nu}\Box)\, f' = 8\pi G T_{\mu\nu}. \tag{6.1}$$

Based on our preliminary numerical experiments, simulating collapse in the Jordan frame seems not a trivial issue. Among all the possible causes, the presence of second-order derivatives of f' might be an important one. Compared to the first-order derivatives of f', the second-order ones could produce more noises in the simulations, causing instabilities especially at the inner boundary that we are more concerned with, and eventually crashing the simulations. Although simulating collapse in the Jordan frame could be implemented in principle, more efforts need to be invested. In this thesis, for computational convenience, we consider an alternative and simpler approach: transforming $f(R)$ gravity from the Jordan frame into the Einstein frame. In the latter, the second-order derivatives of f' are absent in the field equations for the metric components. The formalism can be treated as Einstein gravity coupled to two scalar fields. Therefore, we can use some results that have been developed in the numerical relativity community.

As discussed in Sec. 2.2.3, in the conformal transformation from the Jordan frame into the Einstein frame, we rescale $\chi(\equiv f')$ by

$$\kappa\phi \equiv \sqrt{\frac{3}{2}}\ln\chi. \tag{6.2}$$

Then, in the Einstein frame, the Einstein field equations are

$$\tilde{G}_{\mu\nu} = \kappa^2\left[\tilde{T}^{(\phi)}_{\mu\nu} + \tilde{T}^{(M)}_{\mu\nu}\right], \tag{6.3}$$

where $\tilde{T}^{(\phi)}_{\mu\nu}$ and $\tilde{T}^{(\phi)}_{\mu\nu}$ are the energy-momentum tensors for the scalar field ϕ and matter field, respectively.

$$\tilde{T}^{(\phi)}_{\mu\nu} = \partial_\mu\phi\partial_\nu\phi - \tilde{g}_{\mu\nu}\left[\frac{1}{2}\tilde{g}^{\alpha\beta}\partial_\alpha\phi\partial_\beta\phi + V(\phi)\right], \tag{6.4}$$

$$\tilde{T}^{(M)}_{\mu\nu} = \frac{T^{(M)}_{\mu\nu}}{\chi}. \tag{6.5}$$

$T^{(M)}_{\mu\nu}$ is the ordinary energy-momentum tensor of the physical matter field in terms of $g_{\mu\nu}$ in the Jordan frame.

We tried to use a dust field as the matter field for the collapse. Its energy-momentum tensor is $T_{\mu\nu} = \rho U_\mu U_\nu$, where ρ is the mass density, and U_μ is the four-velocity. However, in this case, the simulations can become unstable very easily. Therefore, we switch to the scalar field, which is stiffer than the dust field. We take a massless scalar field ψ as the matter field for the collapse. Its energy-momentum tensor in the Einstein frame is

$$\tilde{T}^{(M)}_{\mu\nu} = \tilde{T}^{(\psi)}_{\mu\nu} = \frac{1}{\chi}\left(\partial_\mu\psi\partial_\nu\psi - \frac{1}{2}g_{\mu\nu}g^{\alpha\beta}\partial_\alpha\psi\partial_\beta\psi\right) = \frac{1}{\chi}\left(\partial_\mu\psi\partial_\nu\psi - \frac{1}{2}\tilde{g}_{\mu\nu}\tilde{g}^{\alpha\beta}\partial_\alpha\psi\partial_\beta\psi\right), \tag{6.6}$$

which gives

$$\tilde{T}^{(M)} = \tilde{T}^{(\psi)} \equiv \tilde{g}^{\mu\nu}\tilde{T}^{(\psi)}_{\mu\nu} = -\frac{\tilde{g}^{\alpha\beta}\partial_\alpha\psi\partial_\beta\psi}{\chi}.$$

The equations of motion for ϕ and ψ can be derived from the Lagrange equations as

$$\tilde{\Box}\phi - V'(\phi) + \kappa Q\tilde{T}^{(M)} = 0, \tag{6.7}$$

$$\tilde{\Box}\psi - \sqrt{\frac{2}{3}}\,\kappa\tilde{g}^{\mu\nu}\partial_\mu\phi\partial_\nu\psi = 0, \tag{6.8}$$

where $Q \equiv -\chi_{,\phi}/(2\kappa\chi) = -1/\sqrt{6}$. Equation (6.8) can also be obtained from the Lagrange equation in the Jordan frame. Since the scalar field ψ is massless in the Jordan frame, there is

$$\begin{aligned} 0 = \Box\psi &= \frac{1}{\sqrt{-g}}\partial_\mu\left(\sqrt{-g}g^{\mu\nu}\partial_\nu\psi\right) \\ &= \frac{1}{\sqrt{-\tilde{g}\cdot\chi^{-4}}}\partial_\mu\left(\sqrt{-\tilde{g}\cdot\chi^{-4}}\cdot\chi\cdot\tilde{g}^{\mu\nu}\partial_\nu\psi\right) \\ &= \chi\left[\tilde{\Box}\psi - \tilde{g}^{\mu\nu}\partial_\mu\psi\partial_\nu(\ln\chi)\right] \\ &= \chi\left[\tilde{\Box}\psi - \sqrt{\frac{2}{3}}\,\kappa\tilde{g}^{\mu\nu}\partial_\mu\phi\partial_\nu\psi\right]. \end{aligned} \tag{6.9}$$

In the Einstein frame, the potential and the first-order derivative of the potential with respect to ϕ are

$$V(\phi) = \frac{\chi R - f}{2\kappa^2\chi^2}, \tag{6.10}$$

$$V'(\phi) = \frac{dV}{d\chi}\cdot\frac{d\chi}{d\phi} = \frac{1}{\sqrt{6}}\frac{2f - \chi R}{\kappa\chi^2}. \tag{6.11}$$

6.2.2 Coordinate system

We are interested in the singularity formation, the dynamics of the spacetime and the source fields near the singularity, and the global structure of the spacetime. The double-null coordinates described by Eq. (6.12) are a viable choice to realize these objectives:[37]

$$ds^2 = e^{-2\sigma}(-dt^2 + dx^2) + r^2 d\Omega^2 = -4e^{-2\sigma} du dv + r^2 d\Omega^2, \tag{6.12}$$

where σ and r are functions of (t, x), and $u[= (t-x)/2 = \text{Const}]$ and $v[= (t+x)/2 = \text{Const}]$ are outgoing and ingoing characteristics, respectively. The two-manifold metric

$$d\gamma^2 = e^{-2\sigma}(-dt^2 + dx^2) = -4e^{-2\sigma} du dv$$

is conformally flat. In these coordinates, one can know the speed of information propagation everywhere in advance. The metric (6.12) is invariant for the rescaling $u \to U(u)$, $v \to V(v)$. We fix this gauge freedom by setting up initial and boundary conditions.

6.2.3 $f(R)$ model

We take the Hu-Sawicki $f(R)$ model as an example. We consider one of the simplest versions of this model,

$$f(R) = R - \frac{DR_0 R}{R + R_0}, \tag{6.13}$$

where D is a dimensionless parameter, $R_0 = 8\pi G\bar{\rho}_0/3$, and $\bar{\rho}_0$ is the average matter density of the current Universe. In this model,

$$f' = 1 - \frac{DR_0^2}{(R + R_0)^2}, \tag{6.14}$$

$$R = R_0 \left[\sqrt{\frac{D}{1 - f'}} - 1 \right]. \tag{6.15}$$

In the Einstein frame, for the Hu-Sawicki model, the potential and the first-order derivative of the potential with respect to ϕ are

$$V(\phi) = \frac{DR_0 R^2}{2\kappa^2 f'^2 (R + R_0)^2}, \tag{6.16}$$

$$V'(\phi) = \frac{1}{\sqrt{6}} \frac{2f - \chi R}{\kappa \chi^2} = \frac{R^3}{\sqrt{6}\kappa f'^2 (R + R_0)^2} \left[1 + (1 - D)\frac{R_0}{R} \left(2 + \frac{R_0}{R} \right) \right]. \tag{6.17}$$

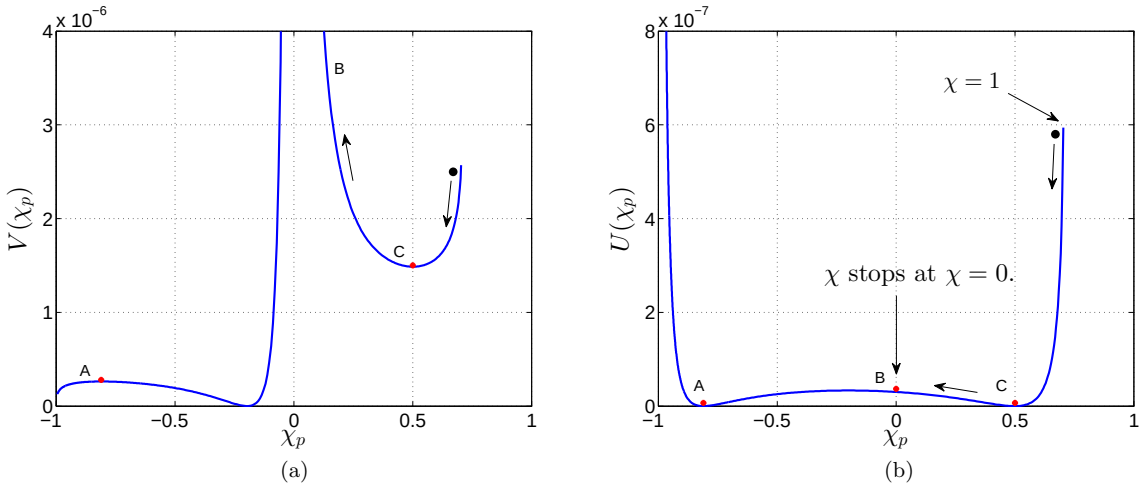

Figure 6.1: The potentials for the Hu-Sawicki model in (a) the Einstein frame and (b) the Jordan frame. χ_p is a compactified coordinate obtained via the Poincaré transformation, $\chi_p = \chi/\sqrt{1+\chi^2}$, with $\chi \equiv f'$. The potential $V(\chi(\phi))$ in the Einstein frame is defined by Eq. (6.16), and the potential $U(\chi)$ in the Jordan frame is defined by Eq. (2.17). A scalar field can collapse to form a black hole. As the singularity of the black hole is approached, χ asymptotes to zero.

As implied in Eq. (6.17), in order to make sure that the de Sitter curvature, for which $V'(\phi) = 0$, has a positive value, the parameter D needs to be greater than 1. In this chapter, we set D and R_0 to 1.2 and 5×10^{-6}, respectively. Then, together with Eqs. (6.16) and (6.17), these values imply that the radius of the de Sitter horizon is about $\sqrt{1/R_0} \sim 10^3$. Moreover, in the configuration of the initial conditions described in Sec. 6.3.2 and the above values of D and R_0, the radius of the apparent horizon of the formed black hole is about 2.2. [See Fig. 6.6.(b).] The potential in the Einstein frame defined by Eq. (6.16) and the potential in the Jordan frame defined by Eq. (2.17) are plotted in Figs. 6.1(a) and (b), respectively.

After explorations of spherical collapse for one of the simplest versions of the Hu-Sawicki model described by Eq. (6.13), we consider general cases. We let the parameter D in Eq. (6.13) take different values. We also study spherical collapse for the Starobinsky model.[126] All the results turn out to be similar.

6.3 Numerical setup

In this section, we present the numerical formalisms, including field equations, initial conditions, boundary conditions, discretization scheme, and numerical tests. The numerical code used in the chapter is a generalized version of the one developed in Ref.[54]

6.3.1 Field equations

In this chapter, we set $8\pi G$ to 1. In double-null coordinates (6.12), some components of the Einstein tensor can be expressed as follows:

$$G^t_t = \frac{2e^{2\sigma}}{r^2}\left[r(r_{,t}\sigma_{,t} + r_{,x}\sigma_{,x}) + rr_{xx} + \frac{1}{2}(-{r_{,t}}^2 + {r_{,x}}^2) - \frac{1}{2}e^{-2\sigma}\right], \tag{6.18}$$

$$G^x_x = \frac{2e^{2\sigma}}{r^2}\left[-r(r_{,t}\sigma_{,t} + r_{,x}\sigma_{,x}) - rr_{tt} + \frac{1}{2}(-{r_{,t}}^2 + {r_{,x}}^2) - \frac{1}{2}e^{-2\sigma}\right], \tag{6.19}$$

$$G^\theta_\theta = G^\phi_\phi = \frac{e^{2\sigma}}{r}\left[-r_{,tt} + r_{,xx} - r(-\sigma_{,tt} + \sigma_{,xx})\right], \tag{6.20}$$

$$G_{uu} = -\frac{2}{r}(r_{,uu} + 2\sigma_{,u}r_{,u}), \tag{6.21}$$

$$G_{vv} = -\frac{2}{r}(r_{,vv} + 2\sigma_{,v}r_{,v}), \tag{6.22}$$

where $r_{,t} \equiv dr/dt$, and other related quantities are defined in a similar way.

For a massive scalar field with energy-momentum tensor

$$T_{\mu\nu} = \phi_{,\mu}\phi_{,\nu} - g_{\mu\nu}\left[\frac{1}{2}g^{\alpha\beta}\phi_{,\alpha}\phi_{,\beta} + V(\phi)\right], \tag{6.23}$$

there are

$$T^t_t = -e^{2\sigma}\left[\frac{1}{2}(\phi^2_{,t} + \phi^2_{,x}) + e^{-2\sigma}V(\phi)\right], \tag{6.24}$$

$$T^x_x = e^{2\sigma}\left[\frac{1}{2}(\phi^2_{,t} + \phi^2_{,x}) - e^{-2\sigma}V(\phi)\right], \tag{6.25}$$

$$T^\theta_\theta = T^\phi_\phi = -e^{2\sigma}\left[\frac{1}{2}(-\phi^2_{,t} + \phi^2_{,x}) + e^{-2\sigma}V(\phi)\right], \tag{6.26}$$

$$T_{uu} = \phi_{,u}^2, \tag{6.27}$$

$$T_{vv} = \phi_{,v}^2, \tag{6.28}$$

$$T = -e^{2\sigma}(-\phi_{,t}^2 + \phi_{,x}^2) - 4V(\phi). \tag{6.29}$$

In the Einstein frame, using

$$\tilde{G}_t^t + \tilde{G}_x^x = \tilde{T}^{(\phi)t}_{\ \ t} + \tilde{T}^{(\phi)x}_{\ \ x} + \tilde{T}^{(\psi)t}_{\ \ t} + \tilde{T}^{(\psi)x}_{\ \ x},$$

one obtains the equation of motion for the metric component r,

$$r(-r_{,tt} + r_{,xx}) + (-r_{,t}^2 + r_{,x}^2) = e^{-2\sigma}(1 - r^2 V). \tag{6.30}$$

Equation (6.30) involves a delicate cancellation of terms at both small and large r, which makes it susceptible to discretization errors. In order to avoid this problem, when r is not too large, we define $\eta \equiv r^2$, and integrate the equation of motion for η instead. The equation of motion for η can be obtained by rewriting Eq. (6.30) as[54]

$$-\eta_{,tt} + \eta_{,xx} = 2e^{-2\sigma}\left(1 - r^2 V\right). \tag{6.31}$$

When r is very large, the delicate cancellation problem can be avoided by using a new variable $\rho \equiv 1/r$ instead.[54] $\tilde{G}_\theta^\theta = \tilde{T}^{(\phi)\theta}_{\ \ \theta} + \tilde{T}^{(\psi)\theta}_{\ \ \theta}$ provides the equation of motion for σ,

$$-\sigma_{,tt} + \sigma_{,xx} - \frac{-r_{,tt} + r_{,xx}}{r} - \frac{1}{2}(-\phi_{,t}^2 + \phi_{,x}^2) - \frac{1}{2\chi}(-\psi_{,t}^2 + \psi_{,x}^2) = e^{-2\sigma} V. \tag{6.32}$$

In double-null coordinates, the dynamical equations for ϕ (6.7) and ψ (6.8) become, respectively,

$$(-\phi_{,tt} + \phi_{,xx}) + \frac{2}{r}(-r_{,t}\phi_{,t} + r_{,x}\phi_{,x}) = e^{-2\sigma}\left[V'(\phi) + \frac{1}{\sqrt{6}}\kappa\tilde{T}^{(\psi)}\right], \tag{6.33}$$

$$(-\psi_{,tt} + \psi_{,xx}) + \frac{2}{r}(-r_{,t}\psi_{,t} + r_{,x}\psi_{,x}) = \sqrt{\frac{2}{3}}\,\kappa(-\phi_{,t}\psi_{,t} + \phi_{,x}\psi_{,x}), \tag{6.34}$$

where

$$\tilde{T}^{(\psi)} = \frac{e^{2\sigma}(\psi_{,t}^2 - \psi_{,x}^2)}{\chi}. \tag{6.35}$$

The $\{uu\}$ and $\{vv\}$ components of the Einstein equations yield the constraint equations:

$$r_{,uu} + 2\sigma_{,u} r_{,u} = -\frac{r}{2}\left(\phi_{,u}^2 + \frac{\psi_{,u}^2}{\chi}\right), \tag{6.36}$$

$$r_{,vv} + 2\sigma_{,v} r_{,v} = -\frac{r}{2}\left(\phi_{,v}^2 + \frac{\psi_{,v}^2}{\chi}\right). \tag{6.37}$$

Via the definitions of $u = (t-x)/2$ and $v = (t+x)/2$, the constraint equations can be expressed in (t, x) coordinates. Equations $(6.37) - (6.36)$ and $(6.37) + (6.36)$ generate the constraint equations for $\{tx\}$ and $\{tt\} + \{xx\}$ components, respectively,

$$r_{,tx} + r_{,t}\sigma_{,x} + r_{,x}\sigma_{,t} + \frac{r}{2}\phi_{,t}\phi_{,x} + \frac{r}{2\chi}\psi_{,t}\psi_{,x} = 0, \tag{6.38}$$

$$r_{,tt} + r_{,xx} + 2r_{,t}\sigma_{,t} + 2r_{,x}\sigma_{,x} + \frac{r}{2}(\phi_{,x}^2 + \phi_{,t}^2) + \frac{r}{2\chi}(\psi_{,x}^2 + \psi_{,t}^2) = 0. \tag{6.39}$$

In the equation of motion for σ (6.32), the term $(-r_{,tt} + r_{,xx})/r$ needs special attention. [In fact, a similar term, $(-r_{,t}^2 + r_{,x}^2 - e^{-2\sigma})/r$, exists in the equation of motion for r (6.30). However, this problem is avoided by converting Eq. (6.30) into the form (6.31).] The discretization errors of r increase dramatically near the center $x = r = 0$. The discretization errors in the term $(-r_{,tt} + r_{,xx})/r$ are amplified by the division of r. Some efforts have been made to avoid this problem in the community. Critical gravitational collapses in higher dimensions and in Einstein-Gauss-Bonnet gravity were discussed in Ref.[121] and Ref.,[63] respectively. In these two references, the double-null coordinates in the form of (6.40) were used:

$$ds^2 = -\alpha^2 du dv + r^2 d\Omega_{D-2}^2, \tag{6.40}$$

where α and r are functions of (u, v), and D is the dimension of the spacetime. Near the center, instead of integrating the equations of motion, Taylor series expansions were used to get the values of $r_{,u}$ and $\phi_{,u}$, where ϕ is a massless scalar field. In addition, the values of $\alpha_{,v}/\alpha$ and $\phi_{,v}$ were obtained via the combination of values from the evolution equations and values extrapolated from neighboring points in the past light cone. Moreover, in Ref.,[63] an auxiliary function, $\Gamma \equiv (\alpha^2 + 4r_{,u}r_{,v})/r^2$, was defined. In the equations of motion for certain quantities, some related terms are expressed in terms of Γ. The $\Gamma' s$ evolution, $\Gamma_{,v}$, can be obtained from the definition $\Gamma \equiv (\alpha^2 + 4r_{,u}r_{,v})/r^2$.

In Ref.,[43] a new numerical framwork was built, with a dynamical lapse function β being introduced,

$$ds^2 = -\alpha\beta^2 dt^2 + \alpha dx^2 + r^2 d\Omega^2, \tag{6.41}$$

where α, β, and r are functions of (t, x). In order to avoid the instability issue, instead of introducing Γ as was done in Ref.,[63] the Misner-Sharp mass m was introduced as an auxiliary variable,

$$m \equiv \frac{r}{2}\left(1 - g^{\mu\nu} r_{,\mu} r_{,\nu}\right) = \frac{r}{2}\left(\frac{\alpha\beta^2 + r_{,t}^2 - \beta^2 r_{,x}^2}{\alpha\beta^2}\right). \tag{6.42}$$

In this thesis, to circumvent the instability problem, we use the constraint equation (6.36) as proposed in Ref.[54] A new variable g is defined as

$$g = -2\sigma - \ln(-r_{,u}). \tag{6.43}$$

Then, Eq. (6.36) can be written as the equation of motion for g,

$$g_{,u} = \frac{r}{2}\frac{\phi_{,u}^2 + \psi_{,u}^2/\chi}{r_{,u}}. \tag{6.44}$$

In the numerical integration, once the values of g and r at the advanced level are obtained, the value of σ at the current level will be computed from Eq. (6.43).

6.3.2 Initial conditions

For any dynamical system whose evolution is governed by a second-order time derivative equation, its evolution is uniquely determined by setting the value of the dynamical variable, and its first-order time derivative, at any given instant. We set the initial data to be time-symmetric as follows (also refer to Fig. 6.2):

$$r_{,t} = \sigma_{,t} = \phi_{,t} = \psi_{,t} = 0 \qquad \text{at } t = 0. \tag{6.45}$$

In this case, the constraint equation (6.38) is satisfied identically.

We set the initial value of $\psi(r)$ at $t = 0$ as

$$\psi(r) = Q \cdot \tanh\left[(r - r_0)^2\right], \tag{6.46}$$

where Q and r_0 take the values of 0.5 and 5, respectively. The initial value of $\phi(r)$ can be arbitrary as long as it is negative. [See Eq. (2.24) and note that $\chi \equiv f' < 1$.] Here we

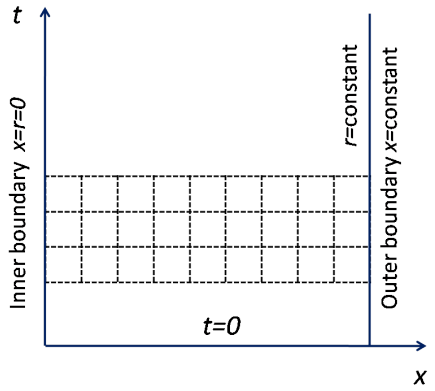

Figure 6.2: Initial and boundary conditions.

choose its value as that in a static system and weak-field limit $r = x$ and $\sigma = 0$. In this case, the equation of motion for ϕ, Eq. (6.33), becomes

$$\frac{d^2\phi}{dr^2} + \frac{2}{r}\frac{d\phi}{dr} = V'(\phi) + \frac{1}{\sqrt{6}}\kappa\tilde{T}^{(\psi)}. \tag{6.47}$$

We solve this equation for initial $\phi(r)$ with Newton's iteration method, enforcing $d\phi/dr = 0$ at $r = 0$ and ϕ to stay at the minimum of the potential $V(\phi)$ at the outer boundary. [Note that $\tilde{T}^{(\psi)} = 0$ at the outer boundary.]

We define a local mass by

$$p \equiv \tilde{g}^{\mu\nu} r_{,\mu} r_{,\nu} = 1 - \frac{2m}{r}. \tag{6.48}$$

Using $r_{,t} = 0$, $x = v - u$, and $t = u + v$, we have $r_{,u} = -r_{,x}$ at $t = 0$. Then, in double-null coordinates described by (6.12), Eq. (6.48) implies that

$$e^{-2\sigma} = \frac{r_{,x}^2}{p}. \tag{6.49}$$

On the other hand, from Eq. (6.43), one obtains, at $t = 0$,

$$r_{,u} = -r_{,x} = -e^{-2\sigma} e^{-g}. \tag{6.50}$$

A combination of Eqs. (6.49) and (6.50) provides the equation for r,

$$r_{,x} = \left(1 - \frac{2m}{r}\right) e^{g}. \tag{6.51}$$

In addition to assigning $r_{,t} = \phi_{,t} = 0$ at $t = 0$, we set $r_{,tt} = 0$ at $t = 0$ to fix the gauge freedom. Consequently, Eqs. (6.39) and (6.30) become, respectively,

$$r_{,xx} + 2r_{,x}\sigma_{,x} + \frac{r}{2}\left(\phi_{,x}^2 + \frac{\psi_{,x}^2}{\chi}\right) = 0, \tag{6.52}$$

$$e^{2\sigma} r_{,xx} = -rV + \frac{2m}{r^2}. \tag{6.53}$$

Differentiating Eq. (6.49) with respect to r yields

$$e^{2\sigma}(2\sigma_{,x} r_{,x} + 2r_{,xx}) = -\frac{2m_{,r}}{r} + \frac{2m}{r^2}. \tag{6.54}$$

Substituting Eqs. (6.52) and (6.53) into (6.54) generates the equation for m

$$m_{,r} = \frac{r^2}{2}\left[V + \frac{1}{2}e^{2\sigma}\left(\phi_{,x}^2 + \frac{\psi_{,x}^2}{\chi}\right)\right]. \tag{6.55}$$

Moreover, with Eqs. (6.48) and (6.49), we have

$$e^{2\sigma}\left(\phi_{,x}^2 + \frac{\psi_{,x}^2}{\chi}\right) \;=\; e^{2\sigma}\left(\phi_{,r}^2 + \frac{\psi_{,r}^2}{\chi}\right) r_{,x}^2 = \left(\phi_{,r}^2 + \frac{\psi_{,r}^2}{\chi}\right)\left(1 - \frac{2m}{r}\right).$$

Then, Eq. (6.55) can be rewritten as

$$m_{,r} = \frac{r^2}{2}\left[V + \frac{1}{2}\left(1 - \frac{2m}{r}\right)\left(\phi_{,r}^2 + \frac{\psi_{,r}^2}{\chi}\right)\right]. \tag{6.56}$$

The equation for g at $t = 0$ can be obtained from Eq. (6.44):

$$g_{,r} = \frac{r}{2}\left(\phi_{,r}^2 + \frac{\psi_{,r}^2}{\chi}\right). \tag{6.57}$$

We obtain the initial values of r, m, and g at $t = 0$ by integrating Eqs. (6.51), (6.56), and (6.57) via the fourth-order Runge-Kutta method. The values of r, σ, $f'[= \exp(\sqrt{2/3}\kappa\phi)]$, and ψ at $t = 0$ are plotted in Fig. 6.7.

We implement a leapfrog scheme, which is a three-level scheme and requires initial data on two different time levels. With the initial data at $t = 0$, we compute the data at $t = \Delta t$ with a second-order Taylor series expansion. Take the variable ϕ as an example:

$$\phi|_{t=\Delta t} = \phi|_{t=0} + \phi_{,t}|_{t=0}\Delta t + \frac{1}{2}\phi_{,tt}|_{t=0}(\Delta t)^2. \tag{6.58}$$

The values of $\phi|_{t=0}$ and $\phi_{,t}|_{t=0}$ are set up as discussed above, and the value of $\phi_{,tt}|_{t=0}$ can be obtained from the equation of motion for ϕ (6.33).

The second-order Taylor series expansion, exemplified by Eq. (6.58), helps to make the numerical results be second-order accurate. More importantly, it is found that this second-order expansion helps to stabilize the numerical simulations. Numerical experiments show that in spherical collapse in general relativity, the simulations remain stable even if we neglect the second-order terms in the expansion. However, in spherical collapse in $f(R)$ theory, the dynamics is more complex. Instability would arise especially at the inner boundary $x = 0$ when the second-order terms were omitted.

6.3.3 Boundary conditions

The range for the spatial coordinates is $x \in [0\ 22]$. The value of 22 is chosen such that it is much less than the radius of the de Sitter horizon ($\sim \sqrt{1/R_0} \sim 10^3$), and it is much greater than the dynamical scale.

On the inner boundary where $x = 0$, r is always set to zero, as illustrated in Fig. 6.2. The terms $2(-r_{,t}\phi_{,t} + r_{,x}\phi_{,x})/r$ and $2(-r_{,t}\psi_{,t} + r_{,x}\psi_{,x})/r$ in Eqs. (6.33) and (6.34) need to be regular at $r = x = 0$. Since r is always set to zero at the center, so is $r_{,t}$. Therefore, we enforce ϕ and ψ to satisfy the following conditions:

$$\phi_{,x} = 0, \qquad \psi_{,x} = 0.$$

The boundary condition for g at $r = 0$ is obtained via extrapolation.

Considering the outer boundary, since one cannot include infinity on the grid, one needs to put a cutoff at x, where the radius r is set to a constant. This is also shown in Fig. 6.2. In this thesis, we are mainly interested in the dynamics around the horizon and the dynamics near the singularity of the formed black hole. The dynamics in these regions will not be affected by the outer boundary conditions, as long as the spatial range of x is large enough compared to the time range needed for black hole formation. We set up the outer boundary conditions via extrapolation.

6.3.4 Discretization scheme

In this thesis, finite difference methods are used. The leapfrog integration scheme is implemented, which is second-order accurate and nondissipative. With the demonstration of

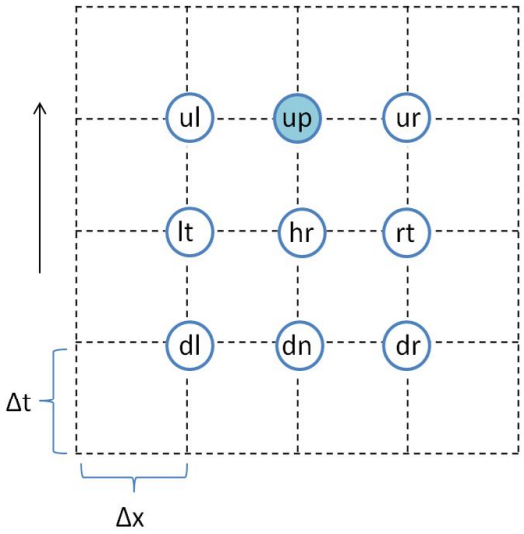

Figure 6.3: Numerical evolution scheme.

Fig. 6.3 and using the variable ϕ as an example, our discretization scheme is expressed below:

$$\frac{d\phi}{dt} = \frac{\phi_{\text{up}} - \phi_{\text{dn}}}{2\Delta t}, \qquad \frac{d\phi}{dx} = \frac{\phi_{\text{rt}} - \phi_{\text{lt}}}{2\Delta x},$$
$$\frac{d^2\phi}{dt^2} = \frac{\phi_{\text{up}} - 2\phi_{\text{hr}} + \phi_{\text{dn}}}{(\Delta t)^2}, \qquad \frac{d^2\phi}{dx^2} = \frac{\phi_{\text{lt}} - 2\phi_{\text{hr}} + \phi_{\text{rt}}}{(\Delta x)^2},$$
$$\frac{d^2\phi}{dxdt} = \frac{\phi_{\text{ur}} - \phi_{\text{ul}} - \phi_{\text{dr}} + \phi_{\text{dl}}}{4\Delta x \cdot \Delta t}, \qquad \frac{d\phi}{du} = \frac{d\phi}{dt} - \frac{d\phi}{dx}.$$

We let the temporal and the spatial grid spacings be equal, $\Delta t = \Delta x$.

The equations of motion for $\eta \equiv r^2$ (6.31), for ϕ (6.33), and for ψ (6.34) are coupled. Newton's iteration method can be employed to solve this problem.[108] With the illustration of Fig. 6.3, the initial conditions provide the data at the levels of "down" and "here," and we need to obtain the data on the level of "up". We take the values at the level of "here" to be the initial guess for the level of "up". Then, we update the values at the level of "up" using the following iteration (taking ϕ as an example):

$$\phi_{\text{up}}^{\text{new}} = \phi_{\text{up}} - \frac{G(\phi_{\text{up}})}{J(\phi_{\text{up}})},$$

where $G(\phi_{\text{up}})$ is the residual of the differential equation for the function ϕ_{up}, and $J(\phi_{\text{up}})$ is the Jacobian defined by

$$J(\phi_{\text{up}}) = \frac{\partial G(\phi_{\text{up}})}{\partial \phi_{\text{up}}}.$$

We do the iterations for all of the coupled equations one by one, and run the iteration loops until the desired accuracies are achieved.

6.3.5 Locating the apparent horizon

Horizons are important characteristics of black holes. For simplicity, we locate the apparent horizon of a black hole formed in the collapse, where the expansion of the outgoing null geodesics orthogonal to the apparent horizon is zero.[11] This implies that, in double-null coordinates,[43] at the apparent horizon

$$\tilde{g}^{\mu\nu} r_{,\mu} r_{,\nu} = e^{2\sigma}(-r_{,t}^2 + r_{,x}^2) = 1 - \frac{2m}{r} = 0. \tag{6.59}$$

With this property, one can look for the apparent horizon. $M(\equiv m/G)$ in Eq. (6.59) is the mass of the black hole.

6.3.6 Examining dynamics near the singularity with mesh refinement

Gravity near the singularity is super strong. In order to study the dynamics and examine the BKL conjecture in this region, high-resolution simulations are needed. To achieve this, one may choose to slow down the evolution near the singularity by multiplying the (t, t) metric component with an appropriate lapse function.[43] However, in this thesis, we employ an alternative approach: fixed mesh refinement, which is similar to the one used in Ref.[60] This technique is very convenient to implement and works very well. Firstly, with numerical results obtained using coarse grid points, we roughly locate the singularity curve $r = 0$, as shown by the solid (blue) line in Fig. 6.4, and choose a region to examine, e.g., the region enclosed by the dash-dotted (green) square. Then the grid points in this region are interpolated with the original grid spacing being halved. We take two neighboring slices, with narrower spatial range, of the newly interpolated results at the midway as new initial data. Specifically, the new initial data are located near the line segment AB in Fig. 6.4. We then run the simulations with these new initial data. The interpolate-and-run loop is iterated until the desired accuracies are obtained.

As discussed in Sec. 6.3.1, in the first simulation with coarse grid points, the term $(-r_{,tt} + r_{,xx})/r$ in (6.32) can create big errors near the center $x = r = 0$. To avoid this problem, we use the constraint equation (6.36) instead. However, at the mesh refinement stage, in the region that we are investigating, the values of r at the two boundaries are

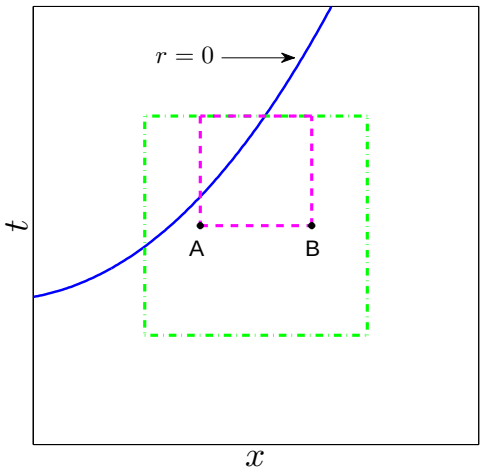

Figure 6.4: Description of fixed mesh refinement. Firstly, with numerical results obtained using coarse grid points, we roughly locate the singularity curve $r = 0$, as shown by the solid (blue) line, and choose a region to examine, e.g., the region enclosed by the dash-dotted (green) square. Then, the grid points in this region are interpolated with the original grid spacing being halved. We take two new neighboring slices as initial data for the next simulation. Specifically, the new initial data are located near the line segment AB. The interpolate-and-run loop is repeated until the desired accuracies are achieved.

usually as regular as those at other neighboring grid points. We need to study the behaviors of all the terms in Eq. (6.32) with high accuracy. Therefore, at the mesh refinement stage, we switch back to Eq. (6.32). The values of the integration variables on the two boundaries are obtained via extrapolation.

6.3.7 Numerical tests

The accuracies of the discretized equations of motion used in the simulations are checked. In the simulations, the range for the spatial coordinates is $x \in [0\ 22]$, and the grid spacing Δx of the coarsest grid is set to 0.01. The constraint equations (6.38) and (6.39) are also examined. The convergence rate of a discretized equation can be obtained from the ratio between residuals with two different step sizes,

$$n = \log_2 \left[\frac{\mathcal{O}(h^n)}{\mathcal{O}\left(\left(\frac{h}{2}\right)^n\right)} \right]. \tag{6.60}$$

Our numerical results show that both of the constraint equations are about second-order convergent. As a representative, in Fig. 6.5(a), we plot the results for the $\{tt\} + \{xx\}$ constraint equation (6.39) when the coordinate time is equal to 3.5.

Convergence tests via simulations with different grid sizes are also implemented.[63,120] If the numerical solution converges, the relation between the numerical solution and the real one can be expressed by

$$F_{\text{real}} = F^h + \mathcal{O}(h^n),$$

where n is the convergence order, and F^h is the numerical solution with step size h. Then, for step sizes of $h/2$ and $h/4$, we have

$$F_{\text{real}} = F^{\frac{h}{2}} + \mathcal{O}\left[\left(\frac{h}{2}\right)^n\right], \qquad F_{\text{real}} = F^{\frac{h}{4}} + \mathcal{O}\left[\left(\frac{h}{4}\right)^n\right].$$

Defining $c_1 \equiv F^h - F^{h/2}$ and $c_2 \equiv F^{h/2} - F^{h/4}$, one can obtain the convergence rate

$$n = \log_2 \left(\frac{c_1}{c_2}\right). \tag{6.61}$$

The convergence tests for $\eta \equiv r^2$, g, ϕ, and ψ are investigated, and they are all second-order convergent. As a representative, in Fig. 6.5(b), the results for η are plotted when the coordinate time is equal to 3.5.

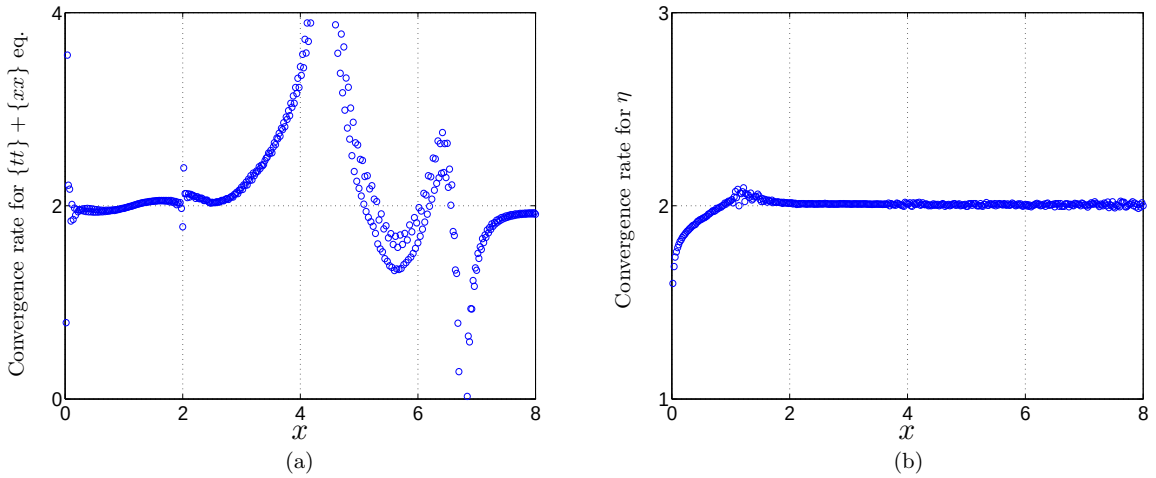

Figure 6.5: Numerical tests when the coordinate time t is equal to 3.5. (a) Convergence, described by Eq. (6.60), for $\{tt\}+\{xx\}$ constraint equation (6.39). In the numerical simulations, this constraint equation is about second-order convergent. (b) Convergence rate, expressed by Eq. (6.61), for $\eta \equiv r^2$. The simulation results for η are second-order convergent.

6.4 Results

A black hole formation from the scalar collapse in $f(R)$ gravity is obtained. During the collapse, the scalar degree of freedom f' is decoupled from the source scalar field ψ and becomes light. Consequently, gravity transits from general relativity to $f(R)$ gravity. Near the singularity, the contributions of various terms in the equations of motion for the metric components and scalar fields are studied. The asymptotic solutions for the metric components and the scalar field ϕ near the singularity are obtained. They are the Kasner solution. These results support the BKL conjecture well.

6.4.1 Black hole formation

Before the collapse, near the scalar sphere, f' stays at the right side of the potential (shown in Fig. 6.1) due to the balance between $U'(f')$ and the force from the physical scalar field ψ. During the collapse, the force from ψ decreases and then changes the direction at a later stage. Correspondingly, f' rolls down the potential and then crosses the minimum of the potential, as depicted in Fig. 6.1. If the energy carried by the scalar field ψ is small enough, the field f' will oscillate and eventually stop at the minimum of the potential, and the field

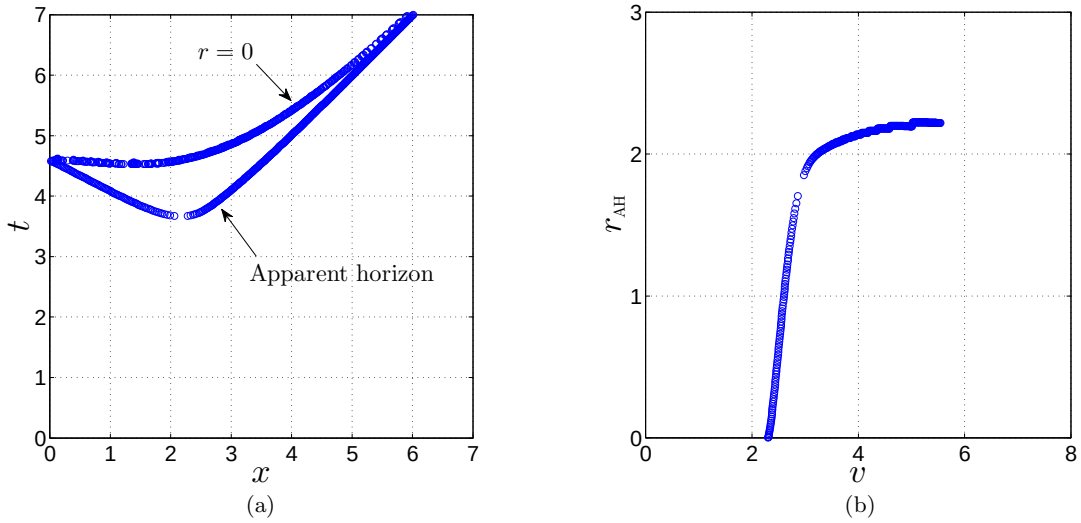

Figure 6.6: Black hole formation from spherical collapse for the Hu-Sawicki model described by Eq. (6.13), with $D = 1.2$ and $R_0 = 5 \times 10^{-6}$. (a) Global structure of spacetime for the collapse. (b) Growth of the apparent horizon. $v = (x + t)/2$.

ψ disperses. The resulting spacetime is a de Sitter spacetime. However, if the scalar field ψ carries enough energy, a black hole will form, and the Weyl tensor and Weyl scalar will become singular as r goes to zero, which is confirmed in Sec. 6.5 and Fig. 6.14. This shows that $r = 0$ is the true singularity inside a black hole. With Eq. (6.59), the apparent horizon is found and plotted in Fig. 6.6. Therefore, a black hole is formed.

6.4.2 Dynamics during collapse

The evolutions of r, σ, f', and ψ are shown in Fig. 6.7. The evolution of the Ricci scalar in the Jordan frame, $R_{\rm JF}$, is plotted in Fig. 6.8. During the collapse, the major part of the energy of the source scalar field ψ is transported to the center. Consequently, the field f' is decoupled from the source field and becomes light. At the same time, as shown in Fig. 6.8, the Ricci scalar in the Jordan frame decreases, and the modification term in the function $f(R)$ becomes important. In this process, gravity transits from general relativity to $f(R)$ gravity. Compared to gravity from the singularity, the left side of the potential $U(f')$ is not steep enough to stop f' from running to the left. Consequently, the field f' rolls down from its initial value, which is close to 1, crosses the de Sitter point, and asymptotes to but does not cross zero near the singularity, as shown in Figs. 6.7(c) and 6.11(c). Simultaneously,

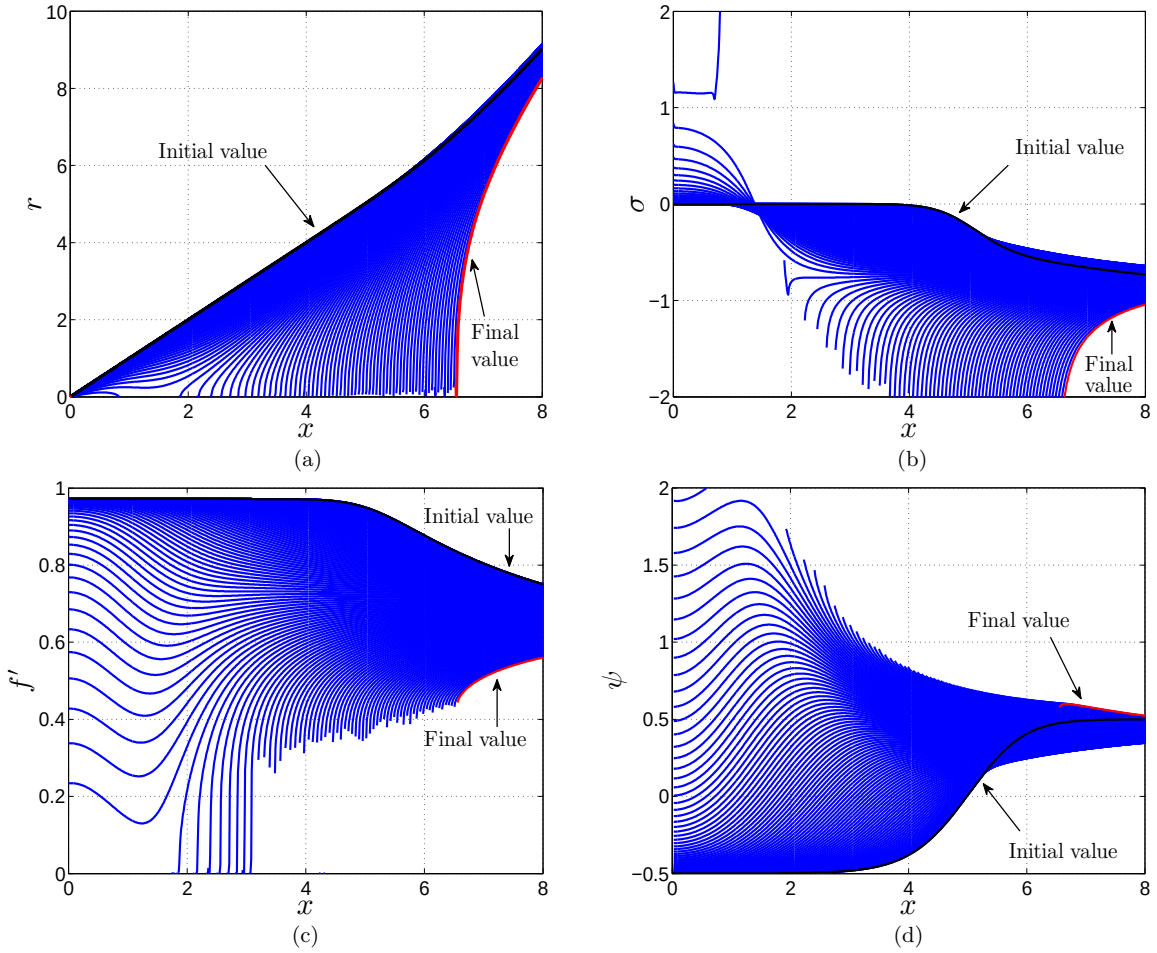

Figure 6.7: Evolutions of the metric components and scalar fields on consecutive time slices. As the singularity curve, $r = 0$, is approached, f' goes to zero, and the physical scalar field ψ becomes singular.

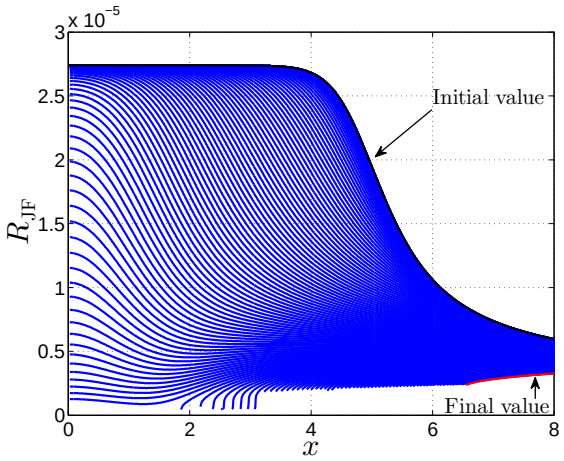

Figure 6.8: Evolution of the Ricci scalar in the Jordan frame on consecutive time slices. Near the boundary of the scalar sphere, the Ricci scalar in the Jordan frame, $R_{\rm JF}$, moves from a large value at the initial state to a very small value as the singularity is approached. Then, gravity transits from general relativity to $f(R)$ gravity.

as shown in Eq. (6.35), the factor $1/f'$ accelerates the transformed energy-momentum of the source field ψ in the Einstein frame to blow up. In other words, one may say that the effective gravitational coupling constant becomes singular at this point. The observations that f' approaches zero are consistent with the results of collapse in Brans-Dicke theory obtained in Ref.[73] One may take $f(R)$ theory as the $\omega = 0$ case of Brans-Dicke theory, where ω is the Brans-Dicke coupling constant. On the other hand, the potential in $f(R)$ theory has a more complicated form than in Brans-Dicke theory. In the latter case the potential is usually set to zero.

We examine the evolutions in the vicinity of the singularity using the fixed mesh refinement method as discussed in Sec. 6.3.6. On the sample slice $(x = 2.5, t = t)$ that we choose to study, the interpolate-and-run loop is iterated 20 times. As a result, the grid spacing $\Delta x = \Delta t$ is reduced from 10^{-2} to 10^{-8}. The smallest value for the radius r we can reach is reduced from 10^{-2} to 10^{-4} (see Figs. 6.9 and 6.11). Note that the radius of the apparent horizon of the formed black hole is about 2.2 [see Fig. 6.6(b)]. The results obtained via mesh refinement support the BKL conjecture well, as discussed below.

One statement of the conjecture is that, in the vicinity of the singularity, gravity dominates over the matter fields. This is verified by the results plotted in Fig. 6.9. The results show that the metric terms are the most important ones, while the potential term and the

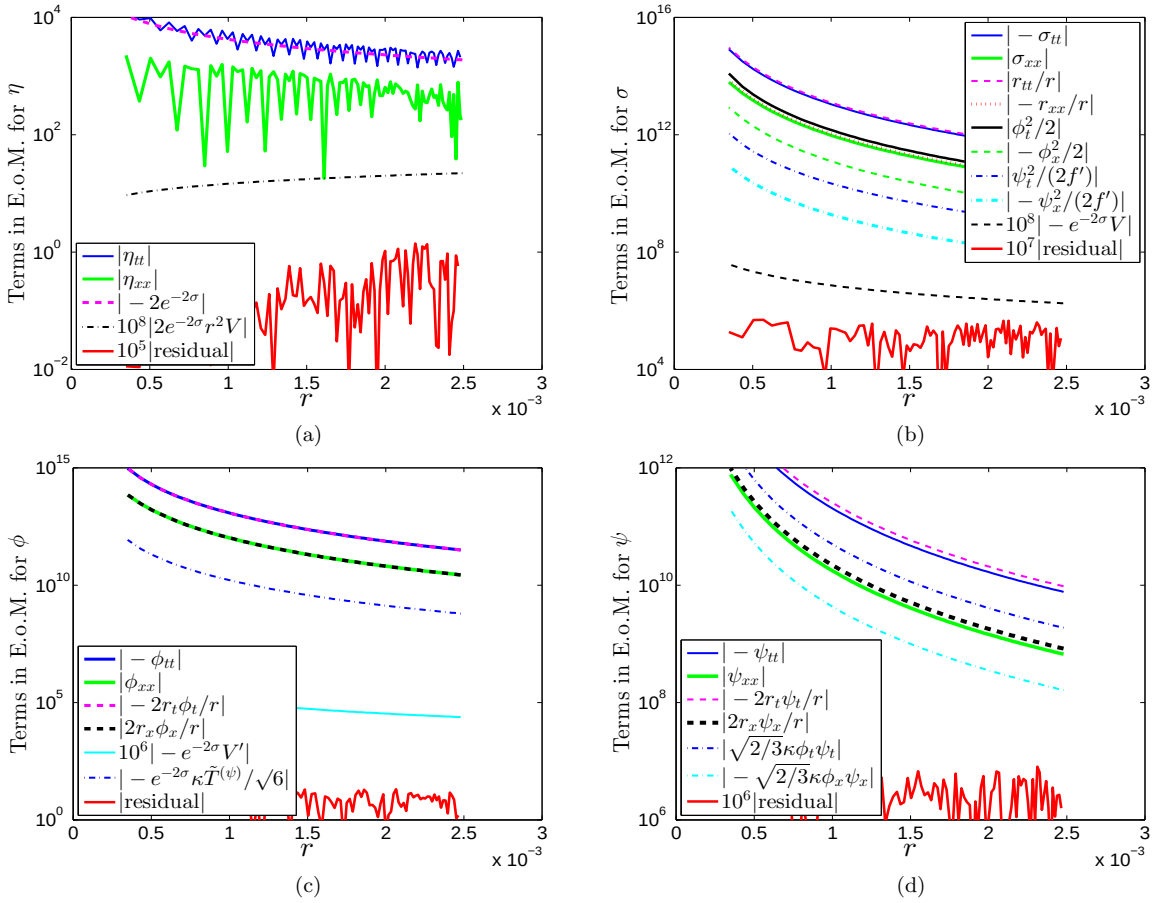

Figure 6.9: (color online) Numerical solutions near the singularity obtained via mesh refinement. The range for the spatial coordinates is $x \in [0\ 22]$, and the solution shown in this figure is for $(x = 2.5, t = t)$. In the vicinity of the singularity, in the equations of motion, the metric component terms are the most important, and the potential terms are the least important. The scalar fields are intermediate. The scalar field ϕ dominates over the physical field ψ. The ratios of $\sigma_{,tt}/\sigma_{,xx}$, $\phi_{,t}^2/\phi_{,x}^2$, and $(r_{,t}\phi_{,t})/(r_{,x}\phi_{,x})$ are all around 11.5. As discussed in Sec. 6.4.2, this is related to the slope of the singularity curve. This implies that the slope of the singularity curve at $x = 2.5$ is about $1/\sqrt{11.5} \approx 0.29$. Consequently, neglecting minor terms, we can approximately rewrite the original equations of motion for σ, ϕ and ψ only in terms of temporal derivatives. (a) The equation of motion for η (6.31) becomes $-\eta_{,tt} + \eta_{,xx} \approx 2e^{-2\sigma}$. (b) The equation of motion for σ (6.32) becomes $-\sigma_{,tt}+r_{,tt}/r+\phi_{,t}^2/2 \approx 0$. (c) The equation of motion for ϕ (6.33) becomes $\phi_{,tt}+2r_{,t}\phi_{,t}/r \approx 0$. (d) The equation of motion for ψ (6.34) becomes $\psi_{,tt} + 2r_{,t}\psi_{,t}/r \approx \sqrt{2/3}\kappa\phi_{,t}\psi_{,t}$. Note that $\phi_{,t}$ is negative. Therefore, the term $\sqrt{2/3}\kappa\phi_{,t}\psi_{,t}$ tries to stop the evolution of ψ. This is a dark energy effect.

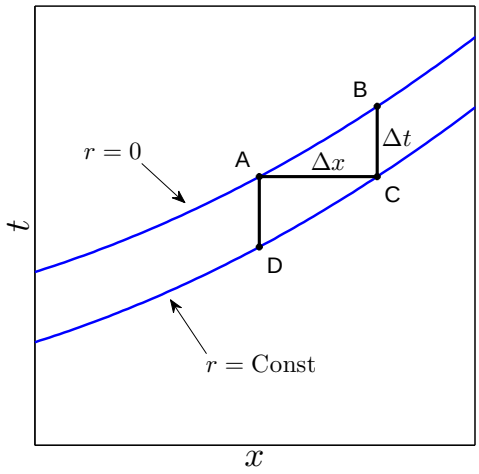

Figure 6.10: Spatial derivative vs temporal derivative near the singularity. Point A and point B are on one same hypersurface $r =$ Const, while point C is on another one. At point C, in first-order accuracy, $r_{,x} \approx (r_C - r_A)/\Delta x$ and $r_{,t} \approx (r_B - r_C)/\Delta t$. Since $r_A = r_B$ and the slope of the singularity curve, dt/dx, is less than 1, there is $|r_{,x}/r_{,t}| \approx |\Delta t/\Delta x| < 1$.

effective force term based on the first-order derivative of the potential with respect to the scalar field ϕ are the least important. The terms related to the scalar fields are intermediate. The field ϕ, transformed from the scalar degree of freedom f', dominates the competition between ϕ and the physical source field ψ [see Figs. 6.9(b)-(d)]. As discussed in the next paragraph, $|\psi_{,t}|$ is no less than $|\psi_{,x}|$. Then, in the equation of motion for ϕ (6.33), the contribution from ψ, $e^{-2\sigma}\kappa\tilde{T}^{(\psi)}/\sqrt{6}\left[=(\psi_{,t}^2 - \psi_{,x}^2)/(\sqrt{6}f')\right]$, is positive. Namely, ψ accelerates the evolution of ϕ. On the other hand, this contribution is tiny compared to gravity [see Fig. 6.9(c)]. The effective force term from the potential is even less than the contribution from ψ. This implies that, in the vicinity of the singularity, ϕ or f' becomes almost massless. Regarding the equation of motion for ψ (6.34), the contribution from ϕ, $\sqrt{2/3}\kappa\phi_{,t}\psi_{,t}$, is relatively important [see Fig. 6.9(d)]. In fact, $\phi_{,t}$ is negative. Therefore, the term $\sqrt{2/3}\kappa\phi_{,t}\psi_{,t}$ functions as a friction force for ψ. This is a dark energy effect. This effect can also be observed via comparison of Figs. 6.11(c) and (d). Because the dynamics of ϕ is mainly determined by gravity, $\phi[\equiv(\sqrt{3/2}\ln f')/\kappa]$ has a good linear relation with $\ln r$ [also refer to Eqs. (6.80) and (6.82)]. However, because of the suppression from ϕ, the field ψ does not have such a linear relation with $\ln r$.

The second statement of the BKL conjecture is that, near the singularity, the terms containing temporal derivatives are dominant over those containing spatial derivatives.

However, in double-null and Kruskal coordinates, temporal derivatives and spatial derivatives are connected by the slope of the singularity curve. We first take the variable r as an example. As illustrated in Fig. 6.10, point A and point B are on one same hypersurface $r =$ Const, while point C is on another one. At point C, in first-order accuracy, $r_{,x} \approx (r_C - r_A)/\Delta x$ and $r_{,t} \approx (r_B - r_C)/\Delta t$. Since $r_A = r_B$ and the slope of the singularity curve, dt/dx, is no greater than 1 [see Fig. 6.6(a)], there is

$$\left|\frac{r_{,x}}{r_{,t}}\right| \approx \left|\frac{\Delta t}{\Delta x}\right| < 1. \tag{6.62}$$

Namely, in the vicinity of the singularity curve, the ratio between spatial and corresponding temporal derivatives is defined by the slope of this singularity curve. (Similar results for a Schwarzschild black hole in Kruskal coordinates can be obtained analytically. Details are given in Appendix 6.8.) This can also be interpreted in the following way. In double-null and Kruskal coordinates, the time vector is not normal to the hypersurface of $r =$ Const. Then, the derivatives in the radial direction have nonzero projections on both hypersurfaces of $x =$ Const and $t =$ Const. With Eq. (6.62), along a certain slice $(x =$ Const$, t = t)$, near the singularity, the ratio between spatial and corresponding temporal derivatives is almost constant.

The fact that the ratios between temporal and spatial derivatives are related to the slope of the singularity curve is also valid for other quantities, e.g., σ, ϕ, and ψ. This can be explained as follows. We take the scalar field ϕ as an example. With the illustration of Fig. 6.10, as this scalar field moves toward the center $r = 0$ along the radial direction, two neighboring points on this scalar wave ϕ should take close values when they cross points C and D, respectively, on one same hypersurface $r =$ Const at two consecutive moments, because these two points on the scalar wave are neighbors and the "distances" AD and BC are more important for their values than the difference between these two neighboring points. In other words, in the vicinity of the singularity curve, gravity is more important than the difference between neighboring points on the scalar wave. These arguments are also supported by numerical results. Near the singularity, the evolution of ϕ is described by Eq. (6.82): $\phi \approx C \ln \xi$, where ξ is the distance between two hypersurfaces of $r =$ Const and $r = 0$. In Fig. 6.10, ξ means AD and BC. As shown in Fig. 6.13(f), the parameter C changes slowly along the singularity curve, compared to the dramatic running of $\ln \xi$ near the singularity. We also checked variations of C as ξ takes different scales on one same slice $(x =$ Const$, t = t)$. The results show that C also changes very slowly.

On the slice $(x = 2.5, t = t)$ that we study, near the singularity, the ratios between second-order temporal derivatives (or the squared/multiplication of first-order time derivatives) and the corresponding spatial derivatives present in Eqs. (6.31)-(6.34), e.g., $\sigma_{,tt}/\sigma_{,xx}$, $\phi_{,t}^2/\phi_{,x}^2$, and $(r_{,t}\phi_{,t})/(r_{,x}\phi_{,x})$, are all around 11.5. As argued in the above paragraph, this implies that the slope of the singularity curve at $x = 2.5$ is about $1/\sqrt{11.5} \approx 0.29$. In addition, as illustrated in Fig. 6.9, the term $2e^{-2\sigma}r^2V$ in Eq. (6.31) and the terms $e^{-2\sigma}[V'(\phi) + \kappa\tilde{T}^{(\psi)}/\sqrt{6}]$ in Eq. (6.33) are negligible. Consequently, we can approximately rewrite the original equation of motion for η (6.31) in the format of (6.63), and rewrite the original equations of motion for σ (6.32), ϕ (6.33), and ψ (6.34) only in terms of temporal derivatives as follows:

$$-\eta_{,tt} + \eta_{,xx} \approx 2e^{-2\sigma}, \tag{6.63}$$

$$-\sigma_{,tt} + \frac{r_{,tt}}{r} + \frac{1}{2}\phi_{,t}^2 \approx 0, \tag{6.64}$$

$$\phi_{,tt} + \frac{2r_{,t}\phi_{,t}}{r} \approx 0 \iff \phi_{,t} \approx \text{Const} \cdot r^{-2} + \text{Const}, \tag{6.65}$$

$$\psi_{,tt} + \frac{2r_{,t}\psi_{,t}}{r} \approx \sqrt{\frac{2}{3}}\,\kappa\phi_{,t}\psi_{,t}. \tag{6.66}$$

Note that $|\eta_{,xx}|$ is no greater than $|\eta_{,tt}|$. As the singularity is approached, $r_{,t}$ and $\phi_{,t}$ are both negative. (Refer to the above arguments at the beginning of this section.) Then, Eq. (6.65) implies that $\phi_{,tt} < 0$. Therefore, ϕ will be accelerated to $-\infty$. Correspondingly, f' approaches zero. Similar arguments can be applied to other equations above. Then, the dynamical system approaches an attractor $(r \to 0, \sigma = -\infty, f' \to 0, \psi = +\infty)$. Next, we will explore the asymptotic solutions based on Eqs. (6.63)-(6.65).

6.4.3 Kasner solution for Schwarzschild black holes

The third statement of the BKL conjecture is that the dynamics near the singularity is expressed by the universal Kasner solution.[82] The Kasner solution is an exact particular solution to Einstein field equations in vacuum, and can be described by Eq. (6.67) with $q = 0$. When a massless scalar field ζ is minimally coupled to gravity, the four-dimensional

homogeneous but anisotropic Kasner solution can be described as follows:[14,81,96]

$$\begin{aligned} ds^2 &= -d\tau^2 + \sum_{i=1}^{3} \tau^{2p_i} dx_i^2, \\ p_1 + p_2 + p_3 &= 1, \\ p_1^2 + p_2^2 + p_3^2 &= 1 - q^2, \\ \zeta &= q \ln \tau, \end{aligned} \tag{6.67}$$

where the parameter q describes the contribution from the field ζ. The parameter q^2 is constrained by Eq. (6.67) as

$$q^2 \leq \frac{2}{3}. \tag{6.68}$$

The Kasner exponents can be expressed in the following parametric form:

$$p_1 = \frac{-w}{1+w+w^2}, \tag{6.69}$$

$$p_2 = \frac{1+w}{1+w+w^2} \left\{ w - \frac{w-1}{2} \left[1 - (1-\alpha^2)^{\frac{1}{2}} \right] \right\}, \tag{6.70}$$

$$p_3 = \frac{1+w}{1+w+w^2} \left\{ 1 + \frac{w-1}{2} \left[1 - (1-\alpha^2)^{\frac{1}{2}} \right] \right\}, \tag{6.71}$$

$$\alpha^2 = \frac{2(1+w+w^2)^2 q^2}{(w^2-1)^2}. \tag{6.72}$$

The parameter α^2 is no greater than 1. The Kasner exponents are invariant under the transformation of $w \to 1/w$:

$$p_1\left(\frac{1}{w}\right) = p_1(w), \qquad p_2\left(\frac{1}{w}\right) = p_3(w), \qquad p_3\left(\frac{1}{w}\right) = p_2(w).$$

If $q^2 > 0$, there are combinations of positive Kasner exponents, satisfying Eq. (6.67). Moreover, all three Kasner exponents take positive values if $q^2 \geq 1/2$.[14,81] As will be demonstrated in the rest of this chapter, a Schwarzschild black hole and spherical collapse toward a black hole formation have special types of Kasner solution, in which p_2 and p_3 are equal.

The behavior of a test scalar field near the singularity in the spacetime of Oppenheimer-Snyder collapse[100] was simulated in Ref.[62] The spacetime is asymptotically flat. The

results confirmed one statement of the BKL conjecture: the temporal derivative terms are dominant over the spatial ones. In the scalar collapse in $f(R)$ gravity that we study in this thesis, two scalar fields are present. One of them, ψ, is massless, and the other one, ϕ, is very light although it has a mass. Moreover, the spacetime has an asymptotic de Sitter solution.

Due to the close connection between a Schwarzschild black hole and spherical collapse, it is instructive to review the dynamics near the singularity of a Schwarzschild black hole first. In Schwarzschild coordinates, the Schwarzschild metric can be expressed as

$$ds^2 = -\left(1-\frac{2m}{r}\right)dt^2 + \frac{1}{1-\frac{2m}{r}}dr^2 + r^2 d\Omega^2,$$

which, near the singularity, is reduced to

$$ds^2 \approx -\frac{r}{2m}dr^2 + \frac{2m}{r}dt^2 + r^2 d\Omega^2. \tag{6.73}$$

Inside the horizon, r is timelike, and t is spacelike. In this case,

$$\tau \approx \int_0^r \sqrt{\frac{r}{2m}}dr = \frac{\sqrt{2}}{3\sqrt{m}}r^{\frac{3}{2}}, \qquad r \approx \left(\frac{3\sqrt{2m}}{2}\tau\right)^{\frac{2}{3}}. \tag{6.74}$$

Considering Eqs. (6.67), (6.73), and (6.74), we have

$$p_1 = -\frac{1}{3}, \qquad p_2 = p_3 = \frac{2}{3}, \tag{6.75}$$

which clearly are Kasner exponents, satisfying Eq. (6.67), with q being equal to zero.

To be one more step closer to spherical collapse in double-null coordinates, we consider the Schwarzschild metric in Kruskal coordinates, which has the following form:

$$ds^2 = \frac{32m^3}{r}e^{-\frac{r}{2m}}(-dt^2 + dx^2) + r^2 d\Omega^2. \tag{6.76}$$

The Schwarzschild radius r is given by

$$t^2 - x^2 = \left(1-\frac{r}{2m}\right)e^{\frac{r}{2m}}. \tag{6.77}$$

In the vicinity of the singularity curve, we rewrite t as $t = t_0 - \xi$, where t_0 is the coordinate time on the singularity curve and $\xi \ll t_0$. With the spatial coordinate x being fixed, a perturbation expansion near the singularity curve directly yields

$$r \approx \left(16m^2 t_0 \xi\right)^{\frac{1}{2}}. \tag{6.78}$$

Consequently, the proper time is

$$\tau \approx \left(32m^3\right)^{\frac{1}{2}} \int_0^{\xi} r^{-\frac{1}{2}} d\xi \approx \frac{8\sqrt{2}m}{3(t_0)^{\frac{1}{4}}} \xi^{\frac{3}{4}} \approx \frac{\sqrt{2}}{3\sqrt{m}t_0} r^{\frac{3}{2}}.$$

Therefore,

$$r \approx \left(\frac{3\sqrt{2m}t_0}{2}\tau\right)^{\frac{2}{3}}. \tag{6.79}$$

Then, we obtain the same set of Kasner exponents as in Schwarzschild coordinates.

6.4.4 Kasner solution for spherical collapse

The reduced equations of motion, (6.63)-(6.65), numerical results for spherical collapse in $f(R)$ theory, and the analysis of dynamics near the singularity for a Schwarzschild black hole together show that the variables r, σ, and ϕ have the following asymptotic solutions:

$$r \approx A\xi^{\beta}, \tag{6.80}$$

$$\sigma \approx B \ln \xi, \tag{6.81}$$

$$\phi \approx C \ln \xi, \tag{6.82}$$

where ξ is defined in the same way as in the Kruskal case: $\xi = t_0 - t$, where t_0 is the coordinate time on the singularity curve. Substituting the above three expressions into Eq. (6.64) yields a relation between parameters β, B, and C:

$$B \approx \beta(1-\beta) - \frac{C^2}{2}. \tag{6.83}$$

We then put Eqs. (6.80), (6.81), and (6.83) into (6.63). Noting that the ratio $\eta_{,tt}/\eta_{,xx}$ has a certain value near a fixed singularity point, and neglecting minor terms, we obtain

$$\ln(1-2\beta) \approx \left[2(\beta-1)^2 + C^2\right] \ln \xi.$$

As ξ approaches zero, the parameter β needs to be close to $1/2$, so that the two sides of the equation are balanced. In this case, the above equation implies that

$$\beta \approx \frac{1 - \xi^{\frac{1}{2}+C^2}}{2}. \tag{6.84}$$

Therefore, as a function of ξ, r in spherical collapse has an exponent close to the one in a Schwarzschild black hole in Kruskal coordinates [see Eq. (6.78)]. Substitution of Eqs. (6.83) and (6.84) into (6.81) leads to the asymptotic solution for σ,

$$\sigma \approx \left(\frac{1-2C^2}{4}\right)\ln\xi. \tag{6.85}$$

Then, the proper time is

$$\tau = \int_0^{\xi} e^{-\sigma} d\xi \approx \frac{4}{3+2C^2}\xi^{\frac{3+2C^2}{4}}. \tag{6.86}$$

Consequently, one can obtain the expressions for the metric components and scalar field ϕ with respect to τ as follows:

$$r \approx A\xi^{\frac{1}{2}} \approx A\left(\frac{3+2C^2}{4}\tau\right)^{\frac{2}{3+2C^2}}, \tag{6.87}$$

$$e^{-\sigma} \approx \xi^{\frac{-1+2C^2}{4}} \approx \left(\frac{3+2C^2}{4}\tau\right)^{\frac{-1+2C^2}{3+2C^2}}, \tag{6.88}$$

$$\phi \approx C\ln\xi \approx \frac{4C}{3+2C^2}\ln\tau. \tag{6.89}$$

Comparing Eqs. (6.87)-(6.89) to (6.67), we extract

$$p_1 = \frac{-1+2C^2}{3+2C^2}, \qquad p_2 = p_3 = \frac{2}{3+2C^2}, \qquad q = \frac{4C}{3+2C^2}. \tag{6.90}$$

It can be verified that these parameters satisfy Eq. (6.67). It is noticeable that as the parameter C in Eq. (6.89) goes to zero, namely the field ϕ disappears, the Kasner exponents take the same values as in the Schwarzschild black hole case. The above analytic expressions are also supported by numerical results. On the slice that we study, the parameter C for ϕ is obtained by fitting the numerical results, $C = 0.24070 \pm 0.00003$ [see Fig. 6.12(a)]. Then, with Eq. (6.90), the values for the Kasner exponents and the parameter q are

$$p_1 = -0.28375 \pm 0.00001,$$

$$p_2 = p_3 = 0.641874 \pm 0.000006,$$

$$q = 0.308998 \pm 0.000003.$$

As shown in Figs. 6.12(b)-(d), the values for these quantities obtained via fitting the numerical results are

$$p_1 = -0.2650 \pm 0.0003,$$

$$p_2 = p_3 = 0.6475 \pm 0.0002,$$

$$q = 0.3038 \pm 0.0002.$$

The two sets of values are highly compatible. Therefore, we obtain the Kasner solution for spherical scalar collapse in $f(R)$ theory in double-null coordinates in the Einstein frame.

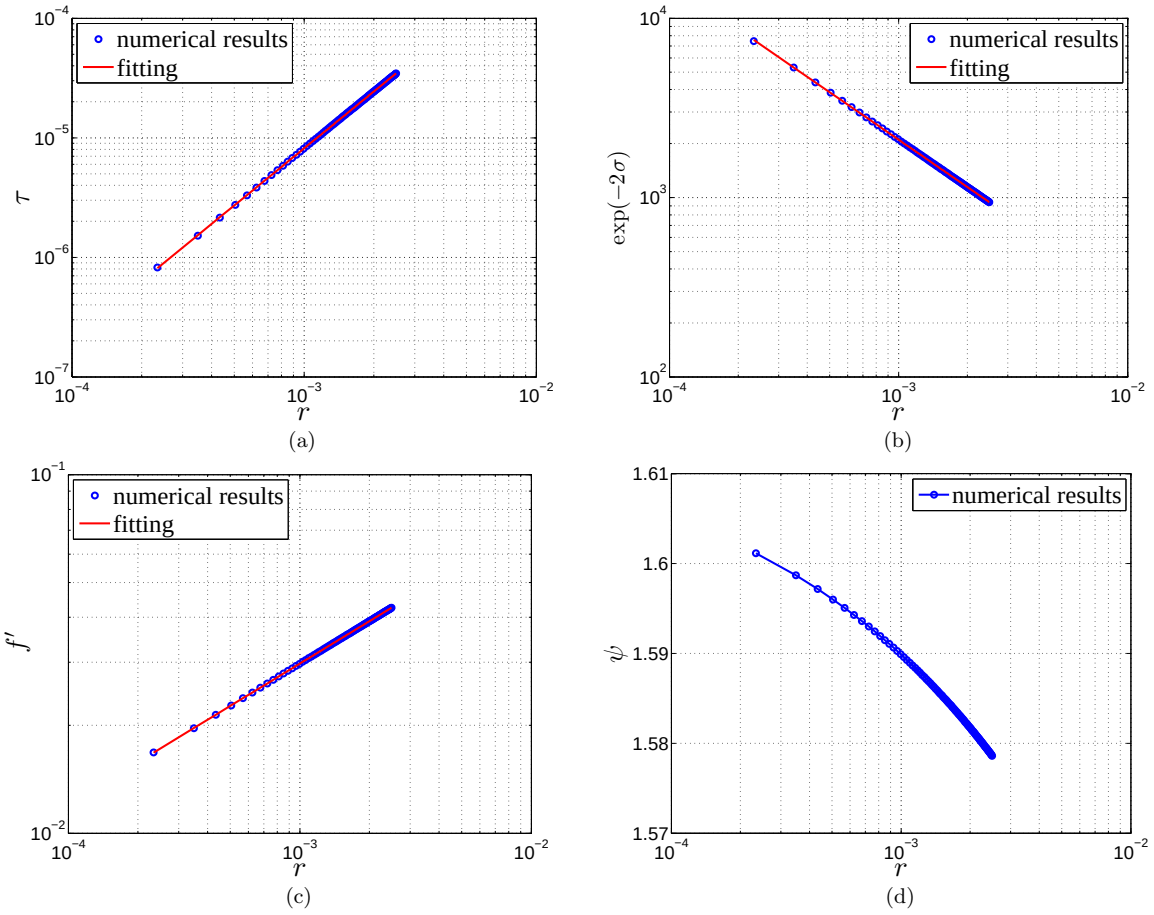

Figure 6.11: Evolutions of the metric components and scalar fields near the singularity obtained via mesh refinement. The range for the spatial coordinates is $x \in [0\ 22]$, and the results shown in this figure are for $(x = 2.5, t = t)$. We fit the results near the singularity as follows. (a) $\ln\tau = a + b\ln r$, $a = -0.774 \pm 0.004$, $b = 1.5843 \pm 0.0006$. (b) $\ln e^{-2\sigma} = -2\sigma = a + b\ln r$, $a = 1.575 \pm 0.003$, $b = -0.8797 \pm 0.0004$. $\ln e^{-2\sigma}(= -2\sigma)$ has an ideal linear relation with $\ln r$, which supports our statements on Eqs. (6.80) and (6.81). (c) $\ln f' = \sqrt{2/3}\kappa\phi = a + b\ln r$, $a = -0.8021 \pm 0.0002$, $b = 0.39288 \pm 0.00004$. Near the singularity, the dynamics of f' or ϕ is mainly determined by gravity. As a result, $\ln f'(= \sqrt{2/3}\kappa\phi)$ has an ideal linear relation with $\ln r$. f' approaches zero as r goes to zero. (d) ψ. Near the singularity, although the evolution of ψ is mainly determined and accelerated by gravity, it is considerably suppressed by ϕ. Consequently, ψ does not have an ideal linear relation with $\ln r$.

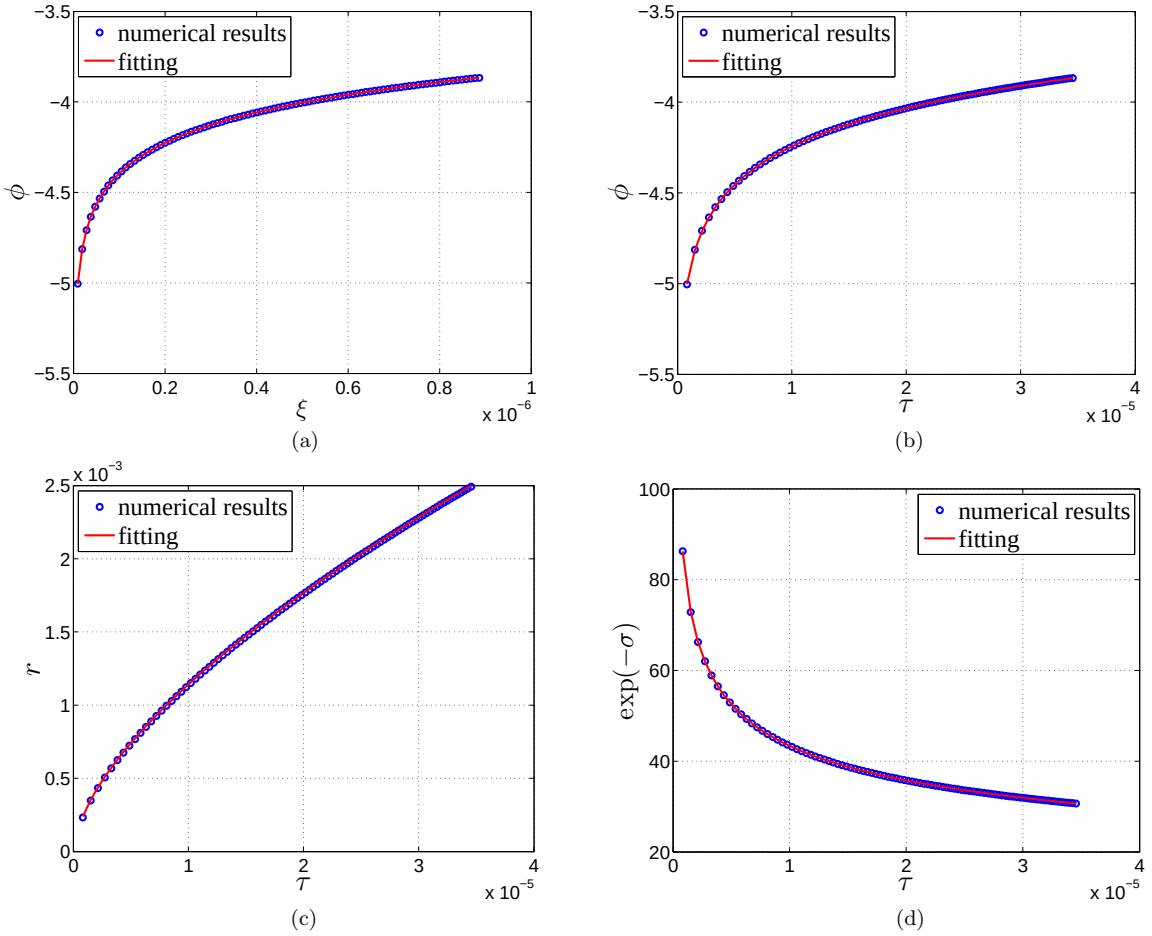

Figure 6.12: Verification of the Kasner solution near the singularity. The results shown in this figure are obtained via mesh refinement. These results are for $(x = 2.5, t = t)$, where t is equal to t_0 when the singularity is approached. We fit the results near the singularity as follows. (a) $\phi = a + b\ln(\xi + c)$, $a = -0.5118 \pm 0.0004$, $b = 0.24070 \pm 0.00003$, $c = (-1.735 \pm 0.008) \times 10^{-9}$. (b) $\phi = a + b\ln(\tau + c)$, $a = -0.747 \pm 0.002$, $b = 0.3038 \pm 0.0002$, $c = (-0.89 \pm 2.75) \times 10^{-9}$. (c) $r = a + b(\tau + c)^d$, $a = (6.00 \pm 0.06) \times 10^{-5}$, $b = 1.895 \pm 0.002$, $c = (-2.17 \pm 0.03) \times 10^{-7}$, $d = 0.6475 \pm 0.0002$. (d) $\exp(-\sigma) = a + b(\tau + c)^d$, $a = -1.98 \pm 0.05$, $b = 2.14 \pm 0.01$, $c = (-1.24 \pm 0.09) \times 10^{-8}$, $d = -0.2650 \pm 0.0003$.

6.4.5 Variations of Kasner parameters along the singularity curve

The Kasner solution described by Eq. (6.90) is a special case of the one expressed by Eqs. (6.69)-(6.72). The two sets of expressions are identical under the conditions

$$\alpha^2 = 1, \qquad |C| = \frac{1}{\sqrt{2}} \left| \frac{1-w}{1+w} \right|. \tag{6.91}$$

We study variations of the parameters A, β, B, and C present in Eqs. (6.80)-(6.82) along the singularity curve by fitting the numerical results to corresponding analytic expressions. The results are plotted in Fig. 6.13. The results imply that at places far away from the center $x = 0$, the contribution from the scalar field ϕ is negligible, and the spacetime is very similar to the one for a Schwarzschild black hole in Kruskal coordinates. Equation (6.78) reveals that $A = 4mt_0^{1/2}$ and $\beta = 1/2$ for a Schwarzschild black hole. In the collapse case, we plot the relation of A vs t_0 in Fig. 6.13(b), while an approximate analytic expression for A vs t_0 is unavailable yet. Figure 6.13(c) shows that β is very close to $1/2$. In Fig. 6.13(d), we plot results for B obtained both via fitting the numerical results and the analytic expression $B = (1 - 2C^2)/4$ [see Eq. (6.85)]. We also compute the relative errors between the two sets of results. The results from the two approaches are very close. They asymptote to $1/4$ at places far from the center $x = 0$. This is consistent with the Schwarzschild black hole case, in which $B = 1/4$.

As functions of C, the Kasner exponents and the parameter q are plotted in Fig. 6.13(e). Equation (6.67) constrains the parameter q as $q \leq \sqrt{2/3}$. This is verified in Fig. 6.13(e). When $C = \sqrt{3/2} \approx 1.22$, there are $q = \sqrt{2/3} \approx 0.82$ and $p_1 = p_2 = p_3 = 1/3$. By fitting the numerical results to Eq. (6.82), we obtain variations of C and q along the singularity curve, as plotted in Fig. 6.13(f). In the direction from $x = 5.5$ toward $x = 0$, q increases and approaches the maximum value, $\sqrt{2/3}$, near $x = 0.3$. Note that q describes the contribution of the scalar field ϕ. The variation of q can be interpreted in a straightforward way. During the collapse, ψ and ϕ move toward the center $x = 0$. Due to interactions between the scalar fields and spacetime, the major energy of ϕ arrives at the formed singularity near $x = 0.3$, and contributes most at this point.

One may wonder what the asymptotic values for A, β, B, and C are as x approaches zero along the singularity curve. Another issue is the running of these parameters with respect to the scale of ξ. Letting the spatial coordinate x take a fixed value, we implement mesh refinement with different iterations. Correspondingly, ξ reaches different scales. We

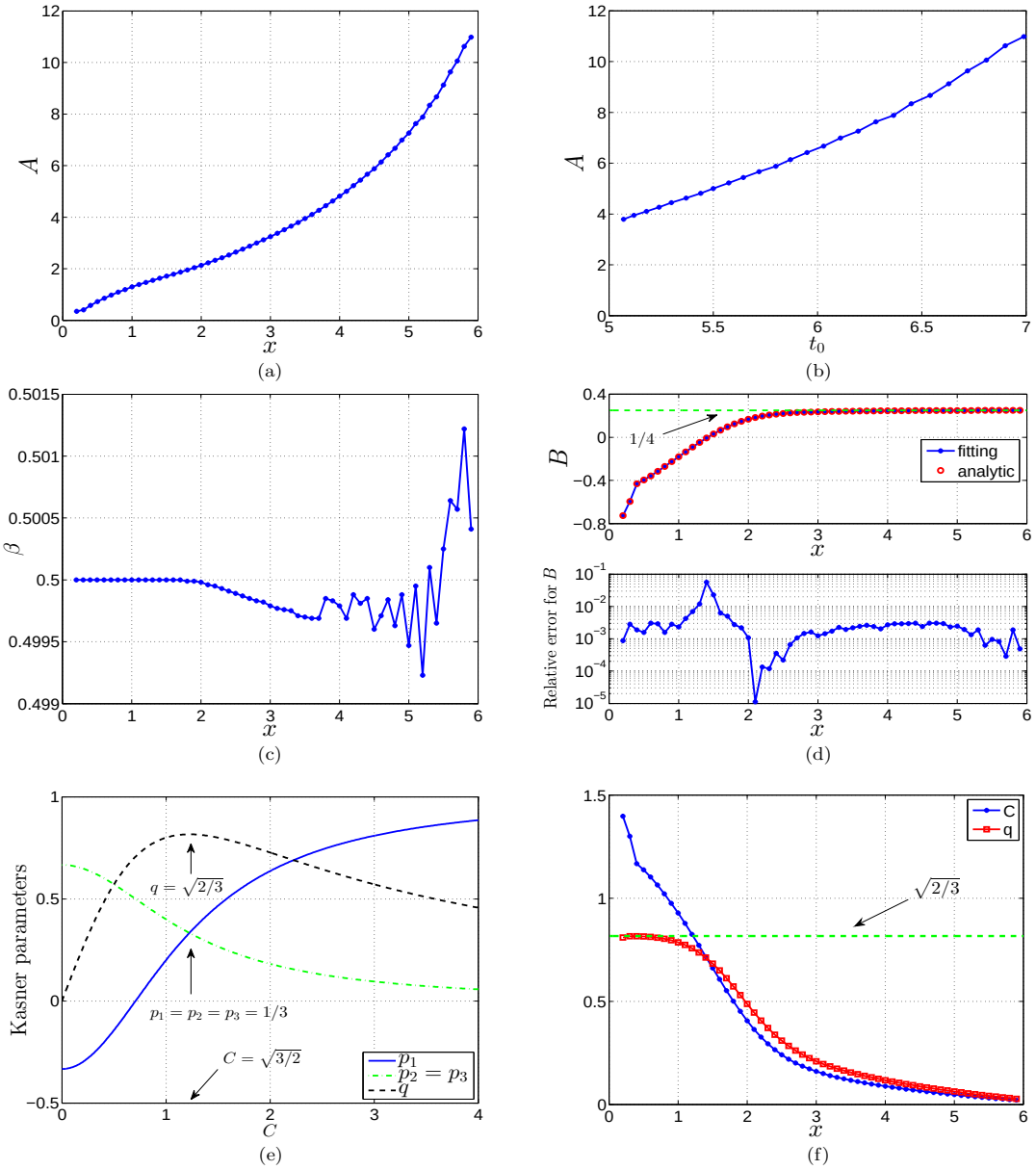

Figure 6.13: Variations of some parameters for the metric components and scalar field along the singularity curve. (a) A for Eq. (6.80): $r \approx A\xi^{\beta}$. (b) A vs t_0. (c) β for Eq. (6.80): $r \approx A\xi^{\beta}$. (d) B for Eq. (6.81): $\sigma \approx B \ln \xi$. (e) The Kasner exponents and the parameter q described by Eq. (6.90). (f) C for Eq. (6.89): $\phi \approx C \ln \xi$. $q = 4C/(3 + 2C^2)$. In the range of $0.2 \leq x \leq 3.7$, 20 iterations of mesh refinement are implemented. In order to make the fitting converge quickly, in the ranges of $3.8 \leq x \leq 5.5$ and $5.6 \leq x \leq 5.9$, 22 and 25 iterations of mesh refinement are implemented, respectively.

obtain C by fitting the numerical results to Eq. (6.82). We find that C is running with respect to the scale of ξ. For example, at $x = 2.5$, C decreases about three percent when the scale of ξ is reduced from 10^{-3} to 10^{-8}. However, detailed studies of such issues are beyond the scope of this thesis.

Note that we are working in the Einstein frame. In this frame, the gravitational theory is similar to general relativity. Two scalar fields, ϕ (or f') and ψ, are present. However, in the vicinity of the singularity, the contributions to the spacetime from the physical scalar field ψ and the potential for ϕ are negligible. The field ϕ is almost massless. The contribution from the almost-massless field ϕ is important. Therefore, this case is essentially the same as single massless scalar (spherical) collapse in general relativity. The Kasner solution we obtained for spherical scalar collapse in $f(R)$ theory is also the corresponding Kasner solution for single massless scalar collapse in general relativity.

The statement that spherical collapse in general relativity ends up with a Schwarzschild black hole has been verified by various numerical simulations. Hawking showed that stationary black holes as the final states of Brans-Dicke collapses are also the solutions of general relativity.[69] This conclusion has been numerically confirmed in Refs.[115,116,118] A static black hole in scalar-tensor theories [including $f(R)$ theory] has a de Sitter-Schwarzschild solution. In the $f(R)$ theory case, f' would stay at the minimum of the potential, $U(f')$. However, numerical simulations show that in the collapse process, f' crosses the minimum of the potential, and asymptotes to zero as the singularity is approached. Namely, the static and dynamical solutions are considerably different. One may wonder whether the collapse will lead to the static solution eventually. Preliminary explorations show that this may not be a trivial question. Further explorations of this problem are omitted in this thesis.

6.5 View from the Jordan frame

Originally, $f(R)$ gravity is defined in the Jordan frame. For computational convenience, we transform $f(R)$ gravity from the Jordan frame into the Einstein frame. After the results have been obtained in the Einstein frame, we convert these results back into the Jordan frame in this section. We examine the Ricci scalar, Weyl scalar, Weyl tensor, and Kasner solution in the Jordan frame.

6.5.1 Ricci scalar

First, using the asymptotic expressions for r (6.80) and σ (6.85), we compute the Ricci scalar in the Einstein frame as follows:

$$\begin{aligned} R_{\mathsf{EF}} &= 2e^{2\sigma}\left[-\sigma_{,tt} + \sigma_{,xx} + \frac{2(r_{,tt} - r_{,xx})}{r} + \frac{(r_{,t})^2 - (r_{,x})^2}{r^2} + \frac{e^{-2\sigma}}{r^2}\right] \\ &\approx (J^2-1)\cdot C^2 \cdot \xi^{-\frac{(3+2C^2)}{2}} \\ &\approx (J^2-1)\cdot C^2 \cdot \left(\frac{r_{\mathsf{EF}}}{A}\right)^{-3-2C^2}, \end{aligned} \tag{6.92}$$

where J is the slope of the singularity curve, and

$$J^2 \approx \frac{r_{,xx}}{r_{,tt}} \approx \frac{\sigma_{,xx}}{\sigma_{,tt}} \approx \frac{(r_{,x})^2}{(r_{,t})^2}. \tag{6.93}$$

Refer to arguments in Sec. 6.4.2 for details on the above equation. We use r and r_{EF} to denote the quantity r in the Einstein frame and r_{JF} in the Jordan frame. The numerical results and fitting results for R_{EF} in the vicinity of the singularity on the slice $(x = 2.5, t = t)$ are plotted in Fig. 6.14(a). We fit the numerical results according to $\ln|R_{\mathsf{EF}}| = a + b\ln(r_{\mathsf{EF}} + c)$. We fix a to -0.592, which is the modified analytic value for a as discussed below. The fitting results are

$$b = -3.1102 \pm 0.0009,$$

$$c = (-3.0 \pm 0.2)\times 10^{-6}.$$

The analytic results are

$$a_{\mathsf{analytic}} = \ln\left[(1-J^2)C^2A^{3+2C^2}\right] = 0.0922 \pm 0.0003,$$

$$b_{\mathsf{analytic}} = -3 - 2C^2 = -3.11587 \pm 0.00003,$$

$$c_{\mathsf{analytic}} = 0.$$

In the above computations, we have used the approximate expression for σ (6.81), $\sigma \approx B\ln\xi$. This expression is valid when r is close enough to zero. The fitting results for σ for the slice $(x = 2.5, t = t)$ are $\sigma = -0.34224 + 0.22108\ln\xi$. If we used this more accurate expression, the modified analytic value for a would be $a_{\mathsf{analytic\text{-}modify}} = -0.592 \pm 0.001$.

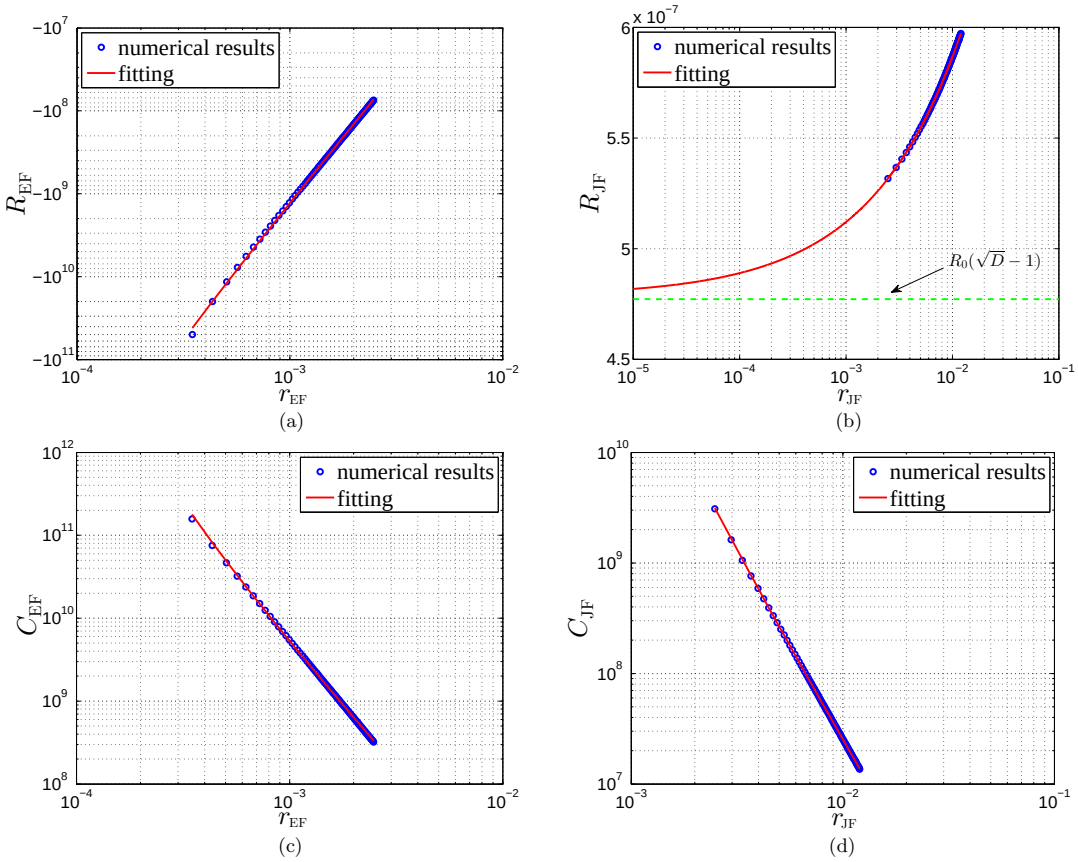

Figure 6.14: Curvature invariants near the singularity in the Einstein and Jordan frames in the collapse of the Hu-Sawicki model expressed by Eq. (6.13). The results are for $(x = 2.5, t = t)$. We fit the results as follows. (a) $\ln|R_{\rm EF}| = a + b\ln(r_{\rm EF} + c)$. We fix a to -0.592, which is the modified analytic value for a. $b = -3.1102 \pm 0.0009$, $c = (-3.0 \pm 0.2) \times 10^{-6}$. $R_{\rm EF}$ diverges in the vicinity of the singularity, due to contributions from the scalar field, $\phi[\equiv (\sqrt{3/2}\ln f')/\kappa]$. (b) $R_{\rm JF} = a + b(r_{\rm JF})^c$, $a = (4.7869 \pm 0.0001) \times 10^{-7}$, $b = (1.1294 \pm 0.0002) \times 10^{-6}$, $c = 0.50983 \pm 0.00006$. As shown in Fig. 6.11(c), when the singularity is approached, f' asymptotes to zero. Consequently, with Eq. (6.94), $R_{\rm JF}$ will approach to a constant: $R_0(\sqrt{D}-1)$. (c) $\ln C_{\rm EF} = a + b\ln(r_{\rm EF} + c)$. We fix a to 2.072, which is the modified analytic value for a. $b = -2.9117 \pm 0.0008$, $c = (7.0 \pm 0.2) \times 10^{-6}$. (d) $\ln C_{\rm JF} = a + b\ln(r_{\rm JF} + c)$, $a = 1.93 \pm 0.03$, $b = -3.265 \pm 0.007$, $c = (2.6 \pm 0.1) \times 10^{-4}$.

The Ricci scalar in the Jordan frame for the Hu-Sawicki model can be obtained from Eq. (6.15). In the vicinity of the singularity, $f' \ll 1$. Then Eq. (6.15) becomes

$$R_{\mathsf{JF}} = R_0 \left[\sqrt{\frac{D}{1-f'}} - 1 \right] \approx R_0(\sqrt{D}-1) + \frac{R_0\sqrt{D}}{2} \left(\frac{r_{\mathsf{JF}}}{A} \right)^{\frac{2\sqrt{2/3}C}{1-\sqrt{2/3}C}}, \tag{6.94}$$

where we have used

$$f' \equiv \chi = e^{\sqrt{\frac{2}{3}}\phi} = \xi^{\sqrt{\frac{2}{3}}C}, \tag{6.95}$$

$$r_{\mathsf{JF}} = r_{\mathsf{EF}} \cdot \chi^{-\frac{1}{2}} \approx A\xi^{\frac{1-\sqrt{2/3}C}{2}}. \tag{6.96}$$

Note that in this chapter we have set $8\pi G = \kappa^2 = 1$. Equation (6.94) reveals that as r_{JF} asymptotes to zero, R_{JF} will approach a constant: $R_0(\sqrt{D}-1)$. The numerical results and fitting results for R_{JF} are shown in Fig. 6.14(b). The numerical results are fit according to $R_{\mathsf{JF}} = a + b(r_{\mathsf{JF}})^c$. The fitting results are

$$a = (4.7869 \pm 0.0001) \times 10^{-7},$$

$$b = (1.1294 \pm 0.0002) \times 10^{-6},$$

$$c = 0.50983 \pm 0.00006.$$

The corresponding analytic results are

$$a_{\mathsf{analytic}} = R_0(\sqrt{D}-1) = 4.77 \times 10^{-7},$$

$$b_{\mathsf{analytic}} = \frac{R_0\sqrt{D}}{2} A^{-\frac{2\sqrt{2/3}C}{1-\sqrt{2/3}C}} = (1.7014 \pm 0.0001) \times 10^{-6},$$

$$c_{\mathsf{analytic}} = \frac{2\sqrt{2/3}C}{1-\sqrt{2/3}C} = 0.48920 \pm 0.00008.$$

In the above computations, we have used the approximate expression for ϕ (6.82), $\phi \approx C \ln \xi$. This expression is valid when r is close enough to zero. The fitting results for ϕ for the slice $(x = 2.5, t = t)$ are $\phi = -0.5118 + 0.2407 \ln \xi$ [see Fig. 6.12(a)]. If we used this more accurate expression, the modified analytic value for b would be $b_{\mathsf{analytic\text{-}modify}} = (1.0114 \pm 0.0004) \times 10^{-6}$.

6.5.2 Weyl scalar

The Ricci tensor and Ricci scalar include information on the traces of the Riemann tensor, while the trace-free parts are described by the Weyl tensor and Weyl scalar. We consider the Weyl scalar and Weyl tensor in this and the next subsections, respectively. It is convenient to define

$$A_W = \sigma_{,xx} - \sigma_{,tt} + \frac{r_{,xx} - r_{,tt}}{r} + \frac{(r_{,t})^2 - (r_{,x})^2}{r^2} + \frac{e^{-2\sigma}}{r^2}. \tag{6.97}$$

Then in the Einstein frame, the Weyl scalar is

$$\begin{aligned} C_{\mathsf{EF}} &\equiv \sqrt{C_{\alpha\beta\mu\nu}C^{\alpha\beta\mu\nu}} = \sqrt{\frac{4}{3}}e^{2\sigma}A_W \\ &\approx \frac{3-2C^2}{2\sqrt{3}}(1-J^2)\xi^{-\frac{3+2C^2}{2}} \\ &\approx \frac{3-2C^2}{2\sqrt{3}}(1-J^2)\left(\frac{r_{\mathsf{EF}}}{A}\right)^{-3-2C^2}, \end{aligned} \tag{6.98}$$

where $C_{\alpha\beta\mu\nu}$ is the Weyl tensor. The numerical and fitting results for C_{EF} are plotted in Fig. 6.14(c). We fit the numerical results according to $\ln C_{\mathsf{EF}} = a + b\ln(r_{\mathsf{EF}} + c)$. We fix a to 2.072, which is the modified analytic value for a as discussed below. The results are

$$b = -2.9117 \pm 0.0008,$$

$$c = (7.0 \pm 0.2) \times 10^{-6}.$$

The analytic results are

$$a_{\mathsf{analytic}} = \ln\left[\tfrac{3-2C^2}{2\sqrt{3}}(1-J^2)A^{3+2C^2}\right] = 2.7574 \pm 0.0001,$$

$$b_{\mathsf{analytic}} = -3 - 2C^2 = -3.11587 \pm 0.00003,$$

$$c_{\mathsf{analytic}} = 0.$$

If we used the more accurate expression for σ, $\sigma = -0.34224 + 0.22108\ln\xi$, the modified analytic value for a would be $a_{\mathsf{analytic\text{-}modify}} = 2.072 \pm 0.001$.

The Weyl scalar in the Jordan frame is[137]

$$C_{\mathsf{JF}} = f' \cdot C_{\mathsf{EF}} \approx \frac{3-2C^2}{2\sqrt{3}}(1-J^2)\left(\frac{r_{\mathsf{JF}}}{A}\right)^{-\frac{3+2C^2-2\sqrt{2/3}C}{1-\sqrt{2/3}C}}. \tag{6.99}$$

We fit the numerical results according to $\ln C_{\text{JF}} = a + b\ln(r_{\text{JF}} + c)$. The results are

$$a = 1.93 \pm 0.03,$$

$$b = -3.265 \pm 0.007,$$

$$c = (2.6 \pm 0.1) \times 10^{-4}.$$

The analytic results are

$$a_{\text{analytic}} = 3.0230 \pm 0.0001,$$

$$b_{\text{analytic}} = -3.3888 \pm 0.0001,$$

$$c_{\text{analytic}} = 0.$$

If we used the more accurate expressions for ϕ and σ, $\phi = -0.5118 + 0.2407\ln\xi$, and $\sigma = -0.34224 + 0.22108\ln\xi$, the modified analytic value for a would be $a_{\text{analytic-modify}} = 2.6247 \pm 0.0002$.

6.5.3 Weyl tensor

The Weyl tensor in the format of $C^{\alpha}_{\beta\mu\nu}$ is invariant under conformal transformations. We compute one component of the Weyl tensor,

$$C^{t}_{xtx} = \frac{1}{3}A_W \approx \frac{1}{3}\left[(1-J^2)\frac{3-2C^2}{4}\xi^{-2} + A^{-2}\xi^{-\frac{3-2C^2}{2}}\right]. \tag{6.100}$$

We also compute the metric components in the Jordan frame in the vicinity of the singularity curve using the transformation relation, $g^{(\text{EF})}_{\mu\nu} = \chi \cdot g^{(\text{JF})}_{\mu\nu}$:

$$r_{\text{JF}} = r_{\text{EF}} \cdot \chi^{-\frac{1}{2}} \approx A\xi^{\frac{1-\sqrt{2/3}C}{2}}, \tag{6.101}$$

$$e^{-\sigma}\big|_{\text{JF}} = e^{-\sigma}\big|_{\text{EF}} \cdot \chi^{-\frac{1}{2}} \approx \xi^{\frac{-1+2C^2-2\sqrt{2/3}C}{4}}. \tag{6.102}$$

Equations (6.100)-(6.102) show that $C = \sqrt{3/2}$ is a special point. As ξ approaches zero, when $0 < C < \sqrt{3/2}$, C^{t}_{xtx} and $e^{-\sigma}|_{\text{JF}}$ become positive infinity, and r_{JF} asymptotes to zero. However, when $C > \sqrt{3/2}$, C^{t}_{xtx} becomes negative infinity, r_{JF} becomes positive infinity, and $e^{-\sigma}|_{\text{JF}}$ asymptotes to zero. Further explorations of these issues are beyond the

scope of this thesis. Since the Weyl tensor is invariant under conformal transformations, C^t_{xtx} will also become positive infinity in the Jordan frame in the case of $0 < C < \sqrt{3/2}$. Moreover, the radius of the apparent horizon for the black hole in the Jordan frame can be obtained from Eq. (6.101). Consequently, a black hole can also be formed in the Jordan frame. The scalar degree of freedom f' will approach zero as r_{JF} asymptotes to zero.

6.5.4 Kasner solution in the Jordan frame

In the Jordan frame, the proper time for the case of $0 < C < \sqrt{3/2}$ is

$$\tau_{\mathsf{JF}} = \int_0^{\xi} e^{-\sigma}\big|_{\mathsf{JF}}\, d\xi \approx \frac{4}{3+2C^2-2\sqrt{2/3}C}\xi^{\frac{3+2C^2-2\sqrt{2/3}C}{4}}. \tag{6.103}$$

Therefore, r_{JF}, $e^{-\sigma}|_{\mathsf{JF}}$, and ϕ can be written in terms of τ_{JF} as follows:

$$r_{\mathsf{JF}} \approx A\left(\frac{3+2C^2-2\sqrt{2/3}C}{4}\tau_{\mathsf{JF}}\right)^{\frac{2\left(1-\sqrt{2/3}C\right)}{3+2C^2-2\sqrt{2/3}C}}, \tag{6.104}$$

$$e^{-\sigma}\big|_{\mathsf{JF}} \approx \left(\frac{3+2C^2-2\sqrt{2/3}C}{4}\tau_{\mathsf{JF}}\right)^{\frac{-1+2C^2-2\sqrt{2/3}C}{3+2C^2-2\sqrt{2/3}C}}, \tag{6.105}$$

$$\phi \approx \frac{4C}{3+2C^2-2\sqrt{2/3}C}\ln\tau_{\mathsf{JF}}. \tag{6.106}$$

Comparing Eqs. (6.104)-(6.106) to (6.67), we have

$${}^{(\mathsf{JF})}p_1 = \frac{-1+2C^2-2\sqrt{2/3}C}{3+2C^2-2\sqrt{2/3}C}, \tag{6.107}$$

$${}^{(\mathsf{JF})}p_2 = {}^{(\mathsf{JF})}p_3 = \frac{2(1-\sqrt{2/3}C)}{3+2C^2-2\sqrt{2/3}C}, \tag{6.108}$$

$${}^{(\mathsf{JF})}q = \frac{4C}{3+2C^2-2\sqrt{2/3}C}. \tag{6.109}$$

Obviously, ${}^{(\mathsf{JF})}p_1$, ${}^{(\mathsf{JF})}p_2$, ${}^{(\mathsf{JF})}p_3$, and ${}^{(\mathsf{JF})}q$ do not satisfy ${}^{(\mathsf{JF})}p_1 + {}^{(\mathsf{JF})}p_2 + {}^{(\mathsf{JF})}p_3 = 1$ and ${}^{(\mathsf{JF})}p_1{}^2 + {}^{(\mathsf{JF})}p_2{}^2 + {}^{(\mathsf{JF})}p_3{}^2 = 1 - {}^{(\mathsf{JF})}q^2$. This is because in the Jordan frame, the scalar degree of freedom, f', is not minimally coupled to gravity, while that is the case in the Einstein frame or general relativity.

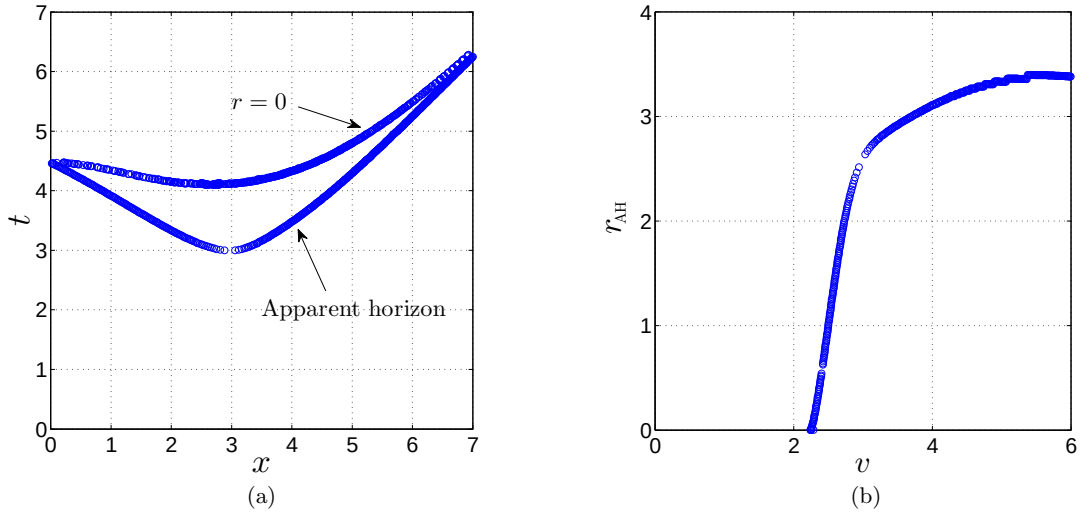

(a) (b)

Figure 6.15: Black hole formation from spherical collapse for the Hu-Sawicki model described by Eq. (6.13), with $D = 1.05$ and $R_0 = 5 \times 10^{-6}$. (a) Global structure of spacetime for the collapse. (b) Growth of the apparent horizon. $v = (x + t)/2$.

6.6 Collapses in more general models

We have studied spherical collapse for one of the simplest versions of the Hu-Sawicki model in the Einstein frame. In this section, we will discuss collapses in more general cases. We will examine how the parameter D in the Hu-Sawicki model (6.13) affects the results. Spherical collapse for another typical dark energy model, the Starobinsky model, will be explored.

6.6.1 Collapse for the Hu-Sawicki model in general cases

In one of the simplest versions of the Hu-Sawicki model, described by Eq. (6.13), the parameter D is set to 1.2. Now we let D take a smaller value, 1.05. This means that the dark energy will play a less important role. The results in this configuration are plotted in Fig. 6.15. Not surprisingly, in comparison to Fig. 6.6 with $D = 1.2$, in this new case, it takes less time to form a black hole, and the radius of the apparent horizon of the formed black hole is larger. In the case of $D = 1.2$, the apparent horizon starts to form at $t = 3.6$, and the radius of the black hole is about 2.2. In the case of $D = 1.05$, the apparent horizon starts to form at $t = 3.0$, and the radius of the black hole is about 3.4.

6.6.2 Collapse for the Starobinsky model

We consider spherical collapse for the Starobinsky model, which can be expressed as follows:[126]

$$f(R) = R + DR_0 \left[\left(1 + \frac{R^2}{{R_0}^2} \right)^{-n} - 1 \right], \tag{6.110}$$

where D and n are positive parameters, and R_0 has the same order of magnitude as the currently observed effective cosmological constant. In the simulations, we set R_0 to 5×10^{-6}.

We simulate collapses with $n = 1$ and $n = 2$. Note that the case of $n = 1$ for the Starobinsky model (6.110) is identical to the case of $n = 2$ for the Hu-Sawicki model (2.43). The results with $n = 1$ and $n = 2$ for the Starobinsky model are similar, and we only present results of the $n = 2$ case in Fig. 6.16. The potentials in Figs. 6.16(a) and (b) are for $D = 2$ and $D = 1.1$, respectively. The results of these two cases are also similar, and only those for $D = 1.1$ are plotted in Figs. 6.16(c) and (d). These results are close to those for the Hu-Sawicki model. Since the potential is not important in the vicinity of the singularity, f' asymptotes to zero as the singularity is approached, no matter what the potential looks like near $f' = 0$. [See Figs. 6.16(a) and (b).]

6.7 Conclusions

Spherical scalar collapse in $f(R)$ gravity was simulated in this chapter. Two typical dark energy $f(R)$ models, the Hu-Sawicki model and Starobinsky model, were taken as example models. A black hole formation was obtained. The dynamics of the metric components, the scalar degree of freedom f', and a physical scalar field during the collapse process, including near the singularity, were studied. The results confirmed the BKL conjecture.

This work concludes by examining both its numerical and physical findings.

6.7.1 Conclusions on numerical issues

In order to achieve certain objectives, one needs to choose proper coordinates. In numerical simulations, stability is a core issue. Most, if not all, efforts are made to improve the stability of the simulations.

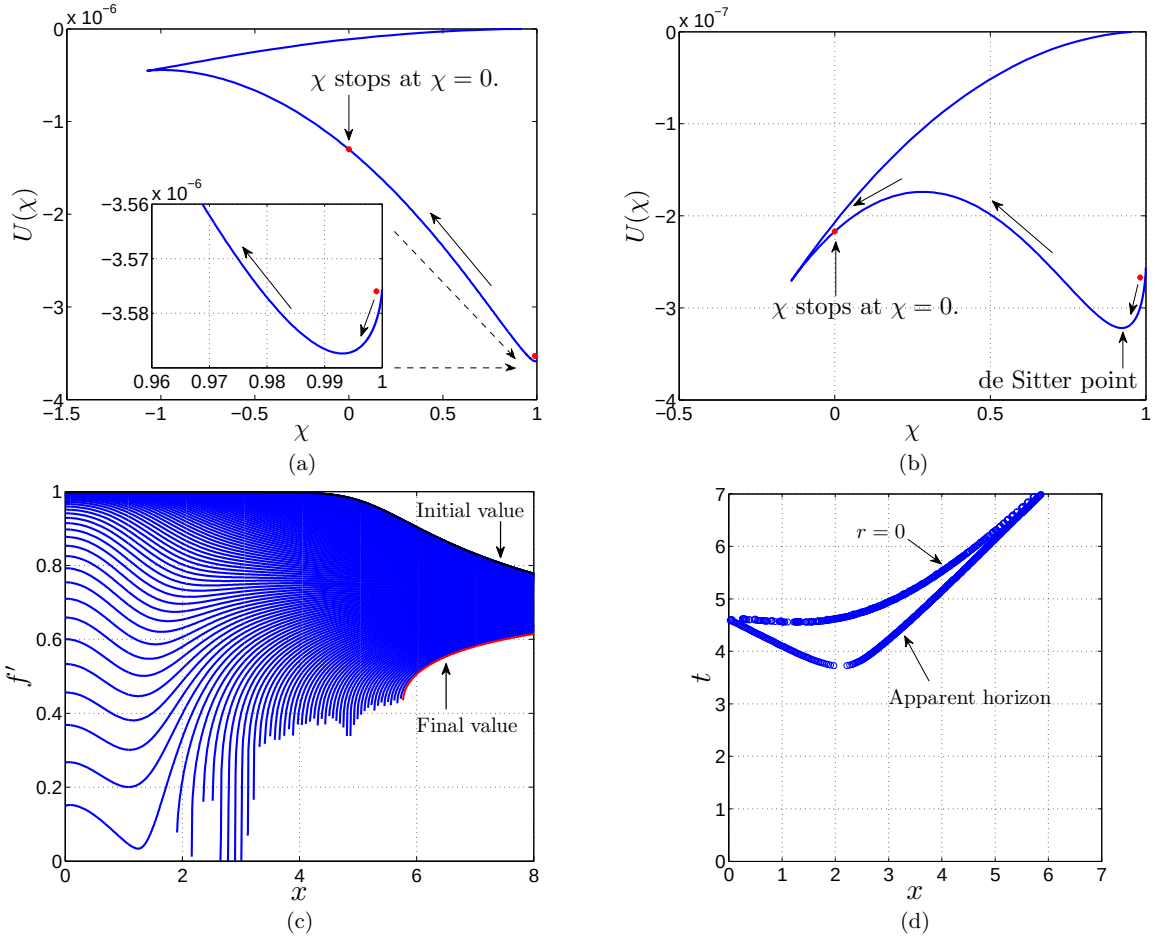

Figure 6.16: Spherical collapse in the Starobinsky model (6.110), with $n = 2$ and $R_0 = 5 \times 10^{-6}$. (a) is for $D = 2$, and (b)-(d) for $D = 1.1$. The results are similar to those in the Hu-Sawicki model. Since the potential is not important in the vicinity of the singularity, $\chi(\equiv f')$ asymptotes to zero as the singularity is approached, no matter what the potential looks like near $\chi = 0$.

- *Coordinates.* The double-null coordinates were employed, which enabled us to study the dynamics both inside and outside the horizon of the formed black hole.

- *Mesh refinement and asymptotic analysis.* Mesh refinement and asymptotic analysis were applied to study the dynamics in the vicinity of the singularity of the formed black hole. Mesh refinement significantly helped us to reveal the dynamics near the singularity, and hence was specially enlightening in seeking approximate analytic solutions. A combination of mesh refinement and asymptotic analysis effectively helped us to obtain the asymptotic analytic solutions near the singularity.

- *Scalar field vs dust field.* A massless scalar field was taken as the matter field for the collapse. A scalar field is much stiffer than a dust field. This helped to make the simulations more stable.

- *Jordan frame vs Einstein frame.* Originally, $f(R)$ gravity was built in the Jordan frame. For computational convenience, we transformed $f(R)$ gravity from the Jordan frame into the Einstein frame, in which the gravitational theory is similar to general relativity. Moreover, in the Einstein frame, the second-order derivatives of f' are absent in the equations of motion for the metric components. This makes the formalism simpler and makes the simulations easier.

- *Choosing proper evolution equations.* In the equations of motion for r (6.30) and σ (6.32), some terms are susceptible to discretization errors at small r. We avoided this problem by rewriting Eq. (6.30) in terms of $\eta \equiv r^2$, and using the constraint equation and defining a new variable $g[= -2\sigma - \ln(-r_{,u})]$ instead. At the mesh refinement stage, where the refinement region is usually a bit far from the center $x = r = 0$, we switch back to Eq. (6.32).

- *First- vs second-order accurate initial conditions.* The leapfrog integration scheme was used in this paper. This scheme needs the initial data at the first two time levels. We obtained the initial data at the first level $t = 0$ by setting the variables to be time-symmetric and then solving the field equations. We computed the initial data at the second level $t = \Delta t$ via a second-order Taylor series expansion. This approach helped to make the simulations second-order accurate. More importantly, it was found that this approach greatly helped to stabilize the simulations in $f(R)$ theory, especially at the center $x = r = 0$.

6.7.2 Conclusions on physical results

The dark energy $f(R)$ theory is a modification of general relativity at the low-curvature scale. Inside a sphere whose matter density is much greater than the dark energy density and whose radius is large enough, f' is coupled to the matter density and is close to 1. Accordingly, $f(R)$ gravity is reduced to general relativity and the modification term is negligible. However, during the collapse, the matter moves to the center of the scalar sphere, which forms a black hole at a later stage. Then, f' loses the coupling and becomes almost massless. Due to the strong gravity from the singularity and the low mass of f', f' crosses its de Sitter value and asymptotes to zero as the singularity is approached. Simultaneously, the modification term in the function $f(R)$ takes effect and even becomes dominant. A static black hole in $f(R)$ theory has a de Sitter-Schwarzschild solution. Therefore, the solution of the dynamical collapse is significantly different from the static one.

In the vicinity of the singularity, in the equations of motion for the metric components and scalar fields, the metric component terms are more important than the scalar field ones. The field ϕ, transformed from the scalar degree of freedom f', dominates the competition between ϕ and the physical field ψ. The field ϕ contributes more to the dynamics of the metric components than ψ does. In the equations of motion for the metric components and ϕ, the contributions of ψ are negligible. However, the effect of ϕ on the evolution of ψ is visible. The field ϕ or effective dark energy tries to stop the collapse of ψ. The metric components and the scalar field ϕ are described by the Kasner solution. These results supported the BKL conjecture well.

Near the singularity, the field ψ can be omitted; while the field ϕ remains, with the potential being negligible. Then the Kasner solution for spherical scalar collapse in $f(R)$ theory that we obtained is also the Kasner solution for collapse in general relativity.

In studies of cosmological dynamics and local tests of $f(R)$ theory, much attention has been given to the right side and the minimum area of the potential as plotted in Fig. 6.1.[57] In the early Universe, the scalar field f' is coupled to the matter density and is close to 1. In the later evolution, f' goes down toward the minimum of the potential, oscillates, and eventually stops at the minimum. In the oscillation epoch, f' does not deviate too far from the minimum. However, in the collapse toward a black hole formation, the strong gravity from the black hole pulls f' in the left direction to a place far away from the minimum. Consequently, the left side of the potential needs more attention in the collapse problem.

6.8 Appendix: Spatial and temporal derivatives near the singularity curve for a Schwarzschild black hole

In this appendix, we derive the analytic expressions for the spatial and temporal derivatives near the singularity curve for a Schwarzschild black hole in Kruskal coordinates. Due to the similarity between Kruskal coordinates and double-null coordinates, these results can provide an intuitive understanding of the relation between the spatial and temporal derivatives near the singularity curve for the collapse in double-null coordinates.

For a Schwarzschild black hole in Kruskal coordinates, the expression for r can be obtained from Eq. (6.77):

$$\frac{r}{2m} = 1 + W(z), \tag{6.111}$$

where

$$z = \frac{x^2 - t^2}{e},$$

and W is the Lambert W function defined by[42]

$$Y = W(Y)e^{W(Y)}. \tag{6.112}$$

Y can be a negative or a complex number. On the hypersurface of $r =$ Const, $z = (x^2 - t^2)/e =$ Const. Then, in the two-dimensional spacetime of (t, x), the slope for the curve $r =$ Const, J, can be expressed as

$$J \equiv \frac{dt}{dx} = \frac{x}{t}. \tag{6.113}$$

The first- and second-order derivatives of W are

$$\frac{dW}{dz} = \frac{W}{z(1+W)}, \qquad \text{for } z \neq \left\{0, -\frac{1}{e}\right\}. \tag{6.114}$$

$$\frac{d^2W}{dz^2} = -\frac{W^2(2+W)}{z^2(1+W)^3}, \qquad \text{for } z \neq \left\{0, -\frac{1}{e}\right\}. \tag{6.115}$$

Consequently, with Eqs. (6.111), (6.114), and (6.115), one can obtain the first- and second-order derivatives of r with respect to x:

$$\frac{1}{2m} \cdot \frac{dr}{dx} = \frac{dW}{dz} \cdot \frac{2x}{e}, \tag{6.116}$$

$$\frac{1}{2m} \cdot \frac{d^2r}{dx^2} = \frac{d^2W}{dz^2}\left(\frac{2x}{e}\right)^2 + \frac{dW}{dz} \cdot \frac{2}{e}. \tag{6.117}$$

Near the singularity curve, $z[=(x^2-t^2)/e]$ approaches $-1/e$, and W asymptotes to -1. Consequently, the second-order derivative of r with respect to x can be approximated as follows:

$$\frac{1}{2m}\cdot\frac{d^2r}{dx^2}\approx-\frac{4x^2}{(1+W)^3}\approx\frac{d^2W}{dz^2}\left(\frac{2x}{e}\right)^2. \tag{6.118}$$

Similarly, one can obtain the first- and second-order derivatives of r with respect to t near the singularity curve:

$$\frac{1}{2m}\cdot\frac{dr}{dt}=-\frac{dW}{dz}\cdot\frac{2t}{e}, \tag{6.119}$$

$$\frac{1}{2m}\cdot\frac{d^2r}{dt^2}\approx-\frac{4t^2}{(1+W)^3}\approx\frac{d^2W}{dz^2}\left(\frac{2t}{e}\right)^2. \tag{6.120}$$

Therefore, with Eqs. (6.116) and (6.118)-(6.120), the ratios between the spatial and temporal derivatives can be expressed by the slope of the singularity curve, J:

$$\frac{\frac{dr}{dx}}{\frac{dr}{dt}}=-\frac{x}{t}=-J, \tag{6.121}$$

$$\frac{\frac{d^2r}{dx^2}}{\frac{d^2r}{dt^2}}\approx\left(\frac{x}{t}\right)^2=J^2. \tag{6.122}$$

As discussed in Sec. 6.4.2, in spherical collapse in double-null coordinates, the ratios between the spatial and temporal derivatives are also defined by the slope of the singularity curve, J.

Chapter 7

Conclusions

7.1 Summary

In this thesis we have studied $f(R)$ model building, cosmological dynamics, Solar System tests of $f(R)$ gravity, and spherical collapse in $f(R)$ gravity.

We explored the running coupling concept in gravity, and discussed the modified gravity models generated from this idea. Two logarithmic models were analyzed. These two models can produce a large hierarchy between the Planck scale and the cosmological constant scale. However, the price is that, at the high-curvature scale, the considerable running of the modification terms with the Ricci scalar makes these two models deviate from general relativity nonnegligibly. Therefore, it is challenging for these two models to generate a viable cosmological evolution and avoid the Solar system tests.

We studied the cosmological viability conditions, phase-space dynamics, and cosmological evolution of $f(R)$ gravity. We developed a set of techniques for the cosmological analysis. We presented generic features of the phase-space dynamics in $f(R)$ cosmology.

We investigated the Solar System tests of $f(R)$ gravity in the Jordan frame. We studied the spacetime of the Solar System where the Sun sits in a vacuum background. We discussed the chameleon mechanism, and also explored the implications of this mechanism for the form of the function $f(R)$. In addition to analytical methods, numerical computations were implemented, which provide an efficient way to study how the scalar field f' behaves in the effective potential.

We simulated spherical scalar collapse in $f(R)$ theory. The results show that a black

hole can be formed. We found that, during the collapse, the major energy of the physical scalar field moves to the center of the sphere. Consequently, f' is released from the coupling to the matter density and becomes light. Due to the strong gravity from the singularity and the low mass of f', f' crosses the minimum of the potential and approaches zero. The static solution of a black hole in $f(R)$ gravity is a de Sitter-Schwarzschild solution. Therefore, the dynamical solution for spherical collapse is significantly different from the static one. In the vicinity of the singularity, spacetime is more important than matter fields. The competition between f' and the physical scalar field was studied. f' suppresses the collapse of the physical scalar field noticeably, while the physical scalar field affects the evolution of f' negligibly. We obtained the Kasner solution for the spherical scalar collapse in $f(R)$ theory. These results verify the Belinskii-Khalatnikov-Lifshitz conjecture in the context of black hole physics.

7.2 Perspectives

Black hole physics is a unique playground to explore gravity and quantum physics. This thesis only considered neutral spherical scalar collapse in $f(R)$ gravity. In fact, a large number of other interesting issues could be explored. Some of them are listed below.

- *Final state of collapse.* In this thesis, we studied the dynamics throughout the collapse, including in the vicinity of the singularity of the formed black hole. However, the final state of the collapse remains unexplored yet. Because of couplings between scalar fields and spacetime, this seems not a trivial issue and deserves to be investigated. The dynamics of a free cosmological scalar field near the horizon of a small black hole was explored analytically in Ref.[76] The generalized circumstances of both lightly and heavily massive scalar fields were analyzed in Ref.[53] An exact solution for a slowly rolling scalar field accreting onto a black hole was found in Ref.[33]

- *Critical collapse.* Critical phenomena of collapse in modified gravity may be another interesting subject to explore. Gravitational collapse shows critical phenomena when a black hole is on the edge of being or not being formed.[35] The mass of the black hole in this critical collapse has a scaling relation with respect to a parameter of the source field. The collapse also shows a discrete self-similarity. These critical

phenomena have also been found in other cases, e.g., gauge field collapse,[36] Brans-Dicke collapse,[93] and Einstein-Gauss-Bonnet collapse.[63] However, critical collapse in $f(R)$ theory has not been studied yet.

- *Charge collapse.* An electrically charged black hole has a more complicated spacetime structure. Therefore, it would be worthwhile to simulate a charge collapse in $f(R)$ theory. In Ref.,[75] charge collapse in $f(R)$ theory was briefly discussed. However, a detailed analysis of the dynamics of (and interactions between) the physical source field, charge, Ricci scalar, and f' has not been done yet. Mass inflation[106,107] and asymptotic solutions near the singularity deserve to be explored.

- *Quantum effects.* In this thesis, we discussed collapses in classical general relativity. It may be exciting to take into account quantum effects. In Refs.,[55,56] the semiclassical geometry of charged black holes was studied in two-dimensional dilaton gravity, and quantum effects were included in the form of pair-production of charged particles. Quantum evaporation of Callan-Giddings-Harvey-Strominger black holes within the mean-field approximation was analyzed in Refs.[6,7]

To unify gravity and quantum field theory and to address certain cosmological problems, people have considered possible gravitational theories beyond general relativity. Confrontations between these theories and the observations imply that more efforts need to be invested, and that the basic principles of classical general relativity and quantum mechanics need to be rethought. More experimental data and observations are required.

Attracted by the possibilities, people have been working toward connecting gravity with quantum physics for several decades. As of yet, a viable and complete quantum theory of gravity has not been constructed. However, the explorations will continue as people are driven to discover new worlds and extend the boundaries of our current knowledge.

Bibliography

[1] P. A. R. Ade *et al.* [Planck Collaboration], *"Planck 2013 results. XXII. constraints on inflation,"* arXiv:1303.5082 [astro-ph.CO] 2, 11, 15

[2] P. A. R. Ade *et al.* [Planck Collaboration] *"Planck 2013 results. I. Overview of products and scientific results,"* arXiv:1303.5062 [astro-ph.CO] 2

[3] L. Amendola, R. Gannouji, D. Polarski, and S. Tsujikawa, *"Conditions for the cosmological viability of f(R) dark energy models,"* Phys. Rev. D **75**, 083504 (2007). [arXiv:gr-qc/0612180] 4, 31, 35

[4] N. Arkani-Hamed, S. Dimopoulos, and G. R. Dvali, *"The hierarchy problem and new dimensions at a millimeter,"* Phys. Lett. **429B**, 263 (1998). [arXiv:hep-ph/9803315] 18

[5] A. Ashtekar, A. Henderson, and D. Sloan, *"A Hamiltonian Formulation of the BKL Conjecture,"* Phys. Rev. D **83**, 084024 (2011). [arXiv:1102.3474 [gr-qc]] 84

[6] A. Ashtekar, F. Pretorius and F. M. Ramazanoglu, "Surprises in the Evaporation of 2-Dimensional Black Holes," Phys. Rev. Lett. **106**, 161303 (2011) [arXiv:1011.6442 [gr-qc]] 134

[7] A. Ashtekar, F. Pretorius and F. M. Ramazanoglu, "Evaporation of 2-Dimensional Black Holes," Phys. Rev. D **83**, 044040 (2011) [arXiv:1012.0077 [gr-qc]] 134

[8] D. Bailin and A. Love, *"Kaluza-Klein theories,"* Rept. Prog. Phys. **50**, 1087 (1987). 1

[9] K. Bamba, C.-Q. Geng, and C.-C. Lee, *"Cosmological evolution in exponential gravity,"* J. Cosmol. Astropart. Phys. **08** (2010) 021. [arXiv:1005.4574 [astro-ph]] 55, 57

[10] A. Barreira, B. Li, C. Baugh, and S. Pascoli, *"Spherical collapse in Galileon gravity: fifth force solutions, halo mass function and halo bias,"* J. Cosmol. Astropart. Phys. **11** (2013) 056. [arXiv:1308.3699 [astro-ph.CO]] 84

[11] T. W. Baumgarte and S. L. Shapiro, *Numerical Relativity: Solving Einstein's Equations on the Computer* (Cambridge University Press, Cambridge, UK, 2010). 98

[12] J. D. Bekenstein, *"Novel 'no-scalar-hair' theorem for black holes,"* Phys. Rev. D **51**, R6608 (1995). 2, 83

[13] V. A. Belinskii, I. M. Kalathnikov, and E. M. Lifshitz, *"Oscillatory Approach to a Singular Point in the Relativistic Cosmology,"* Adv. Phys. **19**, 525 (1970). 84

[14] V. A. Belinskii and I. M. Khalatnikov, *"Effect of scalar and vector fields on the nature of the cosmological singularity,"* Zh. Eksp. Teor. Fiz. **63**, 1121 (1972) [Sov. Phys. JETP **36**, 591 (1973)]. 84, 109

[15] V. A. Belinskii, *"On the cosmological singularity,"* arXiv:1404.3864 [gr-qc] 83

[16] B. K. Berger, D. Garfinkle, J. Isenberg, V. Moncrief, and M. Weaver, *"The Singularity in Generic Gravitational Collapse Is Spacelike, Local, and Oscillatory,"* Mod. Phys. Lett. **A13**, 1565 (1998). [arXiv:gr-qc/9805063] 84

[17] B. K. Berger, *"Numerical Approaches to Spacetime Singularities,"* Living Rev. Relativity **5**, 1 (2002). [arXiv:gr-qc/0201056] 83

[18] P. G. Bergmann, *"Comments on the scalar tensor theory,"* Int. J. Theor. Phys. **1**, 36 (1968). 1, 9

[19] C. P. L. Berry and J. R. Gair, *"Linearized $f(R)$ gravity: Gravitational radiation and Solar System tests,"* Phys. Rev. D **83** (2011) 104022. [arXiv:1104.0819v4 [gr-qc]] 62, 66

[20] E. Berti, V. Cardoso, L. Gualtieri, M. Horbatsch, and U. Sperhake, *"Numerical simulations of single and binary black holes in scalar-tensor theories: circumventing the no-hair theorem,"* Phys. Rev. D **87**, 124020 (2013). [arXiv:1304.2836 [gr-qc]] 83

[21] B. Bertotti, L. Iess, and P. Tortora, *"A test of general relativity using radio links with the Cassini spacecraft,"* Nature **425** (2003) 374. 9, 60

[22] N. D. Birrell and P. C. W. Davies, *Quantum Fields in Curved Space* (Cambridge University Press, Cambridge, UK, 1982). 14

[23] H. Bondi, *"Spherically symmetrical models in general relativity,"* Mon. Not. R. Astron. Soc. **107**, 410 (1947). 83

[24] A. Borkowska, M. Rogatko, and R. Moderski, *"Collapse of Charged Scalar Field in Dilaton Gravity,"* Phys. Rev. D **83**, 084007 (2011). [arXiv:1103.4808 [gr-qc]] 84, 85

[25] C. H. Brans and R. H. Dicke, *"Mach's principle and a relativistic theory of gravitation,"* Phys. Rev. **124**, 925 (1961). 1, 9

[26] C. H. Brans, *"Roots of scalar-tensor theories,"* arXiv:gr-qc/0506063 1

[27] T. S. Bunch and P. C. W. Davies, *"Conditions for the cosmological viability of f(R) dark energy models,"* Proc. R. Soc. London A **356**, 569 (1977). 14

[28] Z. Cao, P. Galaviz, and L.-F. Li, *"Binary black hole mergers in f(R) theory,"* Phys. Rev. D **87**, 104029 (2013). 84

[29] S. M. Carroll, *"The Cosmological Constant,"* Living Rev. Relativity **4**, 1 (2001). [arXiv:astro-ph/0004075] 2

[30] S. M. Carroll, V. Duvvuri, M. Trodden, and M. S. Turner, *"Is Cosmic Speed-Up Due to New Gravitational Physics?"* Phys. Rev. D **70**, 043528 (2004). [arXiv:astro-ph/0306438] 2, 21

[31] S. Carroll, *Spacetime and Geometry: An Introduction to General Relativity* (Addison-Wesley, 2003). 8, 9, 10

[32] J. A. R. Cembranos, A. de la Cruz-Dombriz, and B. M. Nunez, *"Gravitational collapse in f(R) theories,"* J. Cosmol. Astropart. Phys. **04** (2012) 021. [arXiv:1201.1289 [gr-qc]] 84

[33] S. Chadburn and R. Gregory *"Time dependent black holes and scalar hair,"* arXiv:1304.6287 [gr-qc] 133

[34] T. Chiba, T. L. Smith, and A. L. Erickcek, *"Solar System constraints to general f(R) gravity,"* Phys. Rev. D **75**, 124014 (2007). [arXiv:astro-ph/0611867] 62, 63, 66

[35] M. W. Choptuik, *"Universality and scaling in gravitational collapse of a massless scalar field,"* Phys. Rev. Lett. **70**, 9 (1993). 3, 133

[36] M. W. Choptuik, T. Chmaj, and P. Bizon *"Critical behaviour in gravitational collapse of a Yang-Mills field,"* Phys. Rev. Lett. **77**, 424 (1996). [arXiv:gr-qc/9603051] 134

[37] D. Christodoulou, *"Bounded Variation Solutions of the Spherically Symmetric Einstein-Scalar Field Equations,"* Commun. Pure Appl. Math. **46**, 1131 (1993). 5, 85, 88

[38] T. Clifton, *"The Parameterised Post-Newtonian Limit of Fourth-Order Theories of Gravity,"* Phys. Rev. D **77** 024041 (2008). [arXiv:0801.0983 [gr-qc]] 66

[39] T. Clifton, P. G. Ferreira, A. Padilla, and C. Skordis, *"Modified gravity and cosmology,"* Physics Reports **513** (2012) 1. [arXiv:1106.2476 [astro-ph]] 8, 9, 10

[40] G. Cognola, E. Elizalde, S. Nojiri, S. D. Odintsov, L. Sebastiani, and S. Zerbini, *"Class of viable modified f(R) gravities describing inflation and the onset of accelerated expansion,"* Phys. Rev. D **77**, 046009 (2008). [arXiv:0712.4017 [hep-th]] 55

[41] S. Coleman, *"Fate of the false vacuum: Semiclassical theory,"* Phys. Rev. D **15** 2929 (1977). 70, 71

[42] R. M. Corless, G. H. Gonnet, D. E. G. Hare, D. J. Jeffrey, and D. E. Knuth, *"On the Lambert W function,"* Adv. Comput. Math. **5**, 329 (1996). 28, 130

[43] P. Csizmadia and I. Racz, *"Gravitational collapse and topology change in spherically symmetric dynamical systems,"* Classical Quantum Gravity **27**, 015001 (2010). [arXiv:0911.2373 [gr-qc]] 93, 98

[44] P. C. W. Davies, S. A. Fulling, S. M. Christensen and T. S. Bunch, *"Conditions for the cosmological viability of f(R) dark energy models,"* Ann. Phys. **109**, 108 (1977). 14

[45] A. D. Dolgov and M. Kawasaki, *"Can modified gravity explain accelerated cosmic expansion?"* Phys. Lett. **573B**, 1 (2003). [arXiv:astro-ph/0307285] 12, 20, 23

[46] J. F. Donoghue, *"General relativity as an effective field theory: The leading quantum corrections,"* Phys. Rev. D **50**, 3874 (1994). [arXiv:gr-qc/9405057] 1

[47] G. R. Dvali, G. Gabadadze, and M. Porrati, *"4D gravity on a brane in 5D Minkowski space,"* Phys. Lett. **485B**, 208 (2000). [arXiv:hep-ph/0005016] 1, 18

[48] E. Elizalde, S. Nojiri, S. D. Odintsov, L. Sebastiani, and S. Zerbini, *"Non-singular exponential gravity: a simple theory for early- and late-time accelerated expansion,"* Phys. Rev. D **83**, 086006 (2011). [arXiv:1012.2280 [hep-th]] 55

[49] T. Faulkner, M. Tegmark, E. F. Bunn, and Y. Mao, *"Constraining f(R) Gravity as a Scalar Tensor Theory,"* Phys. Rev. D **76** (2007) 063505. [arXiv:astro-ph/0612569v1] 37, 63, 66

[50] A. D. Felice and S. Tsujikawa, *"f(R) Theories,"* Living Rev. Relativity **13**, 3 (2010). [arXiv:1002.4928 [gr-qc]] 2, 13, 66

[51] M. Fierz and W. Pauli, *"On relativistic wave equations for particles of arbitrary spin in an electromagnetic field,"* Proc. Roy. Soc. Lond. **A173**, 211 (1939). 1

[52] E. Fradkin and M. A. Vasiliev, *"On the Gravitational Interaction of Massless Higher Spin Fields,"* Phys. Lett. **189B**, 89 (1987). 8

[53] A. V. Frolov and L. Kofman, *"Inflation and de Sitter Thermodynamics,"* J. Cosmol. Astropart. Phys. **05** (2003) 009. [arXiv:hep-th/0212327] 133

[54] A. V. Frolov, *"Is It Really Naked? On Cosmic Censorship in String Theory,"* Phys. Rev. D **70**, 104023 (2004). [arXiv:hep-th/0409117] 85, 90, 91, 93

[55] A. V. Frolov, K. R. Kristjansson, L. Thorlacius, *"Semi-classical geometry of charged black holes,"* Phys. Rev. D **72**, 021501 (2005). [arXiv:hep-th/0504073] 84, 85, 134

[56] A. V. Frolov, K. R. Kristjansson, L. Thorlacius, *"Global geometry of two-dimensional charged black holes,"* Phys. Rev. D **73**, 124036 (2006). [arXiv:hep-th/0604041] 84, 85, 134

[57] A. V. Frolov, *"A Singularity Problem with f(R) Dark Energy,"* Phys. Rev. Lett. **101**, 061103 (2008). [arXiv:0803.2500 [astro-ph]] 24, 129

[58] A. V. Frolov and J.-Q. Guo, *"Small cosmological constant from running gravitational coupling,"* arXiv:1101.4995 [astro-ph.CO] 19, 26

[59] Y. Fujii and K.-I. Maeda, *The Scalar-Tensor Theory of Gravitation* (Cambridge University Press, Cambridge, UK, 2007). 10

[60] D. Garfinkle, *"Choptuik scaling in null coordinates,"* Phys. Rev. D **51**, 5558 (1995). [arXiv:gr-qc/9412008] 98

[61] D. Garfinkle, *"Numerical Simulations of Generic Singularities,"* Phys. Rev. Lett. **93**, 161101 (2004). [arXiv:gr-qc/0312117] 84

[62] R. Saotome, R. Akhoury, and D. Garfinkle, *"Examining Gravitational Collapse With Test Scalar Fields,"* Classical Quantum Gravity **27**, 165019 (2010). [arXiv:1004.3569 [gr-qc]] 84, 109

[63] S. Golod and T. Piran, *"Choptuik's Critical Phenomenon in Einstein-Gauss-Bonnet Gravity,"* Phys. Rev. D **85**, 104015 (2012). [arXiv:1201.6384 [gr-qc]] 85, 92, 93, 100, 134

[64] J.-A. Gu and W.-T. Lin, *"Solar-System Constraints on f(R) Chameleon Gravity,"* arXiv:1108.1782 [gr-qc] 37

[65] J.-Q. Guo and A. V. Frolov, *"Cosmological dynamics in f(R) gravity,"* Phys. Rev. D **88**, 124036 (2013). [arXiv:1305.7290 [astro-ph.CO]] 30

[66] J.-Q. Guo, *"Solar system tests of f(R) gravity,"* Int. J. Mod. Phys. D**23**, 1450036 (2014). [arXiv:1306.1853 [astro-ph.CO]] 37, 56, 60

[67] J.-Q. Guo, D. Wang, and A. V. Frolov, *"Spherical collapse in $f(R)$ gravity and BKL conjecture,"* arXiv:1312.4625 [gr-qc] 82

[68] T. Harada, T. Chiba, K.-I. Nakao, and T. Nakamura, *"Scalar gravitational wave from Oppenheimer-Snyder collapse in scalar- tensor theories of gravity,"* Phys. Rev. D **55**, 2024 (1997). [arXiv:gr-qc/9611031] 84

[69] S. W. Hawking, *"Black holes in the Brans-Dicke theory of gravitation,"* Comm. Math. Phys. **25**, 167 (1972). 2, 83, 118

[70] M. Henneaux, D. Persson, and P. Spindel, *"Spacelike Singularities and Hidden Symmetries of Gravity,"* Living Rev. Relativity **11**, 1 (2008). [arXiv:0710.1818 [hep-th]] 83

[71] T. Hertog, *"Towards a Novel no-hair Theorem for Black Holes,"* Phys. Rev. D **74**, 084008 (2006). [arXiv:gr-qc/0608075] 83

[72] W. Hu and I. Sawicki, *"Models of f(R) Cosmic Acceleration that Evade Solar-System Tests,"* Phys. Rev. D **76**, 064004 (2007). [arXiv:0705.1158 [astro-ph]] 1, 2, 16, 22, 25, 26, 37, 63, 79

[73] D.-i. Hwang and D.-h. Yeom, *"Responses of the Brans-Dicke field due to gravitational collapses,"* Classical Quantum Gravity **27**, 205002 (2010). [arXiv:1002.4246 [gr-qc]] 84, 85, 104

[74] D.-i. Hwang, H. Kim, and D.-h. Yeom, *"Dynamical formation and evolution of (2+1)-dimensional charged black holes,"* Classical Quantum Gravity **29**, 055003 (2012). [arXiv:1105.1371 [gr-qc]] 85

[75] D.-i. Hwang, B.-H. Lee, and D.-h. Yeom, *"Mass inflation in f(R) gravity: A conjecture on the resolution of the mass inflation singularity,"* J. Cosmol. Astropart. Phys. **12** (2011) 006. [arXiv:1110.0928 [gr-qc]] 84, 134

[76] T. Jacobson, *"Primordial black hole evolution in tensor-scalar cosmology,"* Phys. Rev. Lett. **83**, 2699 (1999). [arXiv:astro-ph/9905303] 133

[77] P. S. Joshi, *Gravitational Collapse and Spacetime Singularities* (Cambridge University Press, Cambridge, UK, 2007). 83

[78] P. S. Joshi, *"Recent developments in gravitational collapse and spacetime singularities,"* Int. J. Mod. Phys. D**20**, 2641 (2011). [arXiv:1201.3660 [gr-qc]] 83

[79] K. Kainulainen, J. Piilonen, V. Reijonen, and D. Sunhede, *"Spherically symmetric spacetimes in f(R) gravity theories,"* Phys. Rev. D **76**, 024020 (2007). [arXiv:0704.2729 [gr-qc]] 63

[80] T. Kaluza, *"On the Problem of Unity in Physics,"* Sitzungsber. Preuss. Akad. Wiss. Berlin (Math. Phys.) **1921**, 966 (1921). 1, 17

[81] A. Yu. Kamenshchik, *"The problem of singularities and chaos in cosmology,"* Phys. -Usp. **53**, 301 (2010). [arXiv:1006.2725 [gr-qc]] 83, 109

[82] E. Kasner, *"Geometrical theorems on Einsteins cosmological equations,"* Am. J. Math, **43**, 217 (1921). 84, 108

[83] A. Kehagias, A. Moradinezhad Dizgah, A. Riotto, *"Comments on the Starobinsky model of inflation and its descendants,"* arXiv:1312.1155 [hep-th] 2, 11, 15

[84] J. Khoury and A. Weltman, *"Chameleon Cosmology,"* Phys. Rev. D **69**, 044026 (2004). [arXiv:astro-ph/0309411] 5, 37, 61, 66

[85] J. Khoury and A. Weltman, *"Chameleon Fields: Awaiting Surprises for Tests of Gravity in Space,"* Phys. Rev. Lett. **93**, 171104 (2004). [arXiv:astro-ph/0309300] 5, 37, 61, 66

[86] O. Klein, *"Quantentheorie und funfdimensionale Relativitatstheorie,"* Zeitschrift fur Physik **37**, 895 (1926). 17

[87] R. A. Knop *et al.* [The Supernova Cosmology Project], *"New Constraints on Ω_M, Ω_Λ, and w from an Independent Set of 11 High-Redshift Supernovae Observed with HST,"* Astrophys. J. **598**, 102 (2003). [arXiv:astro-ph/0309368] 2

[88] T. Kobayashi and K. I. Maeda, *"Relativistic stars in f(R) gravity, and absence thereof,"* Phys. Rev. D **78**, 064019 (2008). [arXiv:0807.2503 [astro-ph]] 62, 63

[89] E. Komatsu *et al.* [WMAP Collaboration], *"Seven-year Wilkinson Microwave Anisotropy Probe (WMAP) Observations: Cosmological Interpretation,"* Astrophys. J. Suppl. **192**, 18 (2011). [arXiv:1001.4538 [astro-ph.CO]] 47, 49

[90] M. Kopp, S. A. Appleby, I. Achitouv, and J. Weller, *"Spherical collapse and halo mass function in f(R) theories,"* Phys. Rev. D **88**, 084015 (2013). [arXiv:1306.3233 [astro-ph.CO]] 84

[91] L. D. Landau and E. M. Lifshitz, *The Classical Theory of Fields*, Course of Theoretical Physics Series Vol.2 (Pergamon Press, Oxford, UK 1971), 4th ed. 84

[92] G. Lemaître, *"The Expanding Universe,"* Annales Soc. Sci. Brux. Ser. I Sci. Math. Astron. Phys. A **53**, 51 (1933). Reprint: Gen. Rel. Grav. **29**, 641 (1997). 83

[93] S. L. Liebling and M. W. Choptuik, *"Black hole criticality in the Brans-Dicke model,"* Phys. Rev. Lett. **77**, 1424 (1996). [arXiv:gr-qc/9606057] 134

[94] E. V. Linder, *"Exponential Gravity,"* Phys. Rev. D **80**, 123528 (2009). [arXiv:0905.2962 [astro-ph]] 55

[95] D. Lovelock, *"The Einstein tensor and its generalizations,"* J. Math. Phys. **12**, 498 (1971). 1, 18

[96] H. Nariai, *"Hamiltonian approach to the dynamics of expanding homogeneous universes in the Brans-Dicke cosmology,"* Prog. Theor. Phys. **47**, 1824 (1972). 109

[97] I. Navarro and K. V. Acoleyen, *"f(R) actions, cosmic acceleration and local tests of gravity," J. Cosmol. Astropart. Phys.* **0702** (2007) 022. [arXiv:gr-qc/0611127] 37

[98] M. Niedermaier, *"The asymptotic safety scenario in quantum gravity: An introduction,"* Classical Quantum Gravity **24**, R171 (2007). [arXiv:gr-qc/0610018] 20

[99] A. Nunez and S. Solganik, *"The content of f(R) gravity,"* arXiv:hep-th/0403159 20, 23

[100] J. R. Oppenheimer and H. Snyder, *"On Continued Gravitational Contraction,"* Phys. Rev. **56**, 455 (1939). 83, 109

[101] P. J. E. Peebles, B. Ratra, *"The cosmological constant and dark energy,"* Rev. Mod. Phys. **75**, 559 (2003). [arXiv:astro-ph/0207347] 20

[102] R. Percacci, *"Asymptotic safety,"* In "Approaches to Quantum Gravity: Towards a New Understanding of Space, Time and Matter", ed. D. Oriti, Cambridge University Press, Cambridge, UK, 111-128 (2009). [arXiv:0709.3851 [hep-th]] 20

[103] S. Perlmutter *et al.* [Supernova Cosmology Project Collaboration], *"Measurements of Ω and Λ from 42 high redshift supernovae,"* Astrophys. J. **517**, 565 (1999). [arXiv:astro-ph/9812133] 2

[104] M. E. Peskin and D. V. Schroeder, *An Introduction to Quantum Field Theory* (Westview Press, Boulder, U.S.A., 1995). 19

[105] L. Pogosian and A. Silvestri, *"The pattern of growth in viable f(R) cosmologies,"* Phys. Rev. D **77** 023503 (2008). [arXiv:0709.0296 [astro-ph]] 13

[106] E. Poisson and W. Israel, *"Inner-horizon instability and mass inflation in black holes,"* Phys. Rev. Lett. **63**, 1663 (1989). 134

[107] E. Poisson and W. Israel, *"Internal structure of black holes,"* Phys. Rev. D **41**, 1796 (1990). 134

[108] F. Pretorius, *"Numerical Relativity Using a Generalized Harmonic Decomposition,"* Classical Quantum Gravity **22**, 425 (2005). [arXiv:gr-qc/0407110] 97

[109] L. Randall and R. Sundrum, *"A large mass hierarchy from a small extra dimension,"* Phys. Rev. Lett. **83**, 3373 (1999). [arXiv:hep-th/9905221] 1, 18

[110] L. Randall and R. Sundrum, *"An alternative to compactification,"* Phys. Rev. Lett. **83**, 4690 (1999). [arXiv:hep-th/9906064] 1, 18

[111] C. de Rham and G. Gabadadze, *"Generalization of the Fierz-Pauli Action,"* Phys. Rev. D **82**, 044020 (2010). arXiv:1007.0443 [hep-th] 1

[112] C. de Rham, G. Gabadadze, and A. J. Tolley, *"Resummation of Massive Gravity,"* Phys. Rev. Lett. **106**, 231101 (2011). arXiv:1011.1232 [hep-th] 1

[113] A. G. Riess *et al.* [Supernova Search Team Collaboration], *"Observational evidence from supernovae for an accelerating universe and a cosmological constant,"* Astron. J. **116**, 1009 (1998). [arXiv:astro-ph/9805201] 2

[114] A. G. Riess *et al.* [Supernova Search Team Collaboration], *"Type Ia Supernova Discoveries at $z > 1$ From the Hubble Space Telescope: Evidence for Past Deceleration and Constraints on Dark Energy Evolution,"* Astrophys. J. **607**, 665 (2004). [arXiv:astro-ph/0402512] 2

[115] M. A. Scheel, S. L. Shapiro, and S. A. Teukolsky, *"Collapse to Black Holes in Brans-Dicke Theory: I. Horizon Boundary Conditions for Dynamical Spacetimes,"* Phys. Rev. D **51**, 4208 (1995). [arXiv:gr-qc/9411025] 83, 118

[116] M. A. Scheel, S. L. Shapiro, and S. A. Teukolsky, *"Collapse to Black Holes in Brans-Dicke Theory: II. Comparison with General Relativity,"* Phys. Rev. D **51**, 4236 (1995). [arXiv:gr-qc/9411026] 83, 118

[117] J. M. M. Senovilla, *"Junction conditions for f(R) gravity and their consequences,"* Phys. Rev. D **88**, 064015 (2013). [arXiv:1303.1408 [gr-qc]] 84

[118] M. Shibata, K. Nakao, and T. Nakamura, *"Scalar-type gravitational wave emission from gravitational collapse in Brans-Dicke theory: Detectability by a laser interferometer,"* Phys. Rev. D **50**, 7304 (1994). 83, 118

[119] S. S. Shapiro, J. L. Davis, D. E. Lebach, and J. S. Gregory, *"Measurement of the Solar Gravitational Deflection of Radio Waves using Geodetic Very-Long-Baseline Interferometry Data, 19791999,"* *Phys. Rev. Lett.* **92**, 121101 (2004). 60, 63

[120] E. Sorkin and T. Piran, *"Effects of Pair Creation on Charged Gravitational Collapse,"* Phys. Rev. D **63**, 084006 (2001). [arXiv:gr-qc/0009095] 85, 100

[121] E. Sorkin and Y. Oren, *"On Choptuik's scaling in higher dimensions,"* Phys. Rev. D **71**, 124005 (2005). [arXiv:hep-th/0502034] 92

[122] H. Sotani, *"Scalar gravitational waves from relativistic stars in scalar-tensor gravity,"* Phys. Rev. D **89**, 064031 (2014). [arXiv:1402.5699 [astro-ph]] 84

[123] T. P. Sotiriou and V. Faraoni, *"f(R) Theories Of Gravity,"* Rev. Mod. Phys. **82**, 451 (2010). [arXiv:0805.1726 [gr-qc]] 2, 63, 66

[124] T. P. Sotiriou and V. Faraoni, *"Black holes in scalar-tensor gravity,"* Phys. Rev. Lett. **108**, 081103 (2012). [arXiv:1109.6324 [gr-qc]] 3, 83

[125] A. A. Starobinsky, *"A new type of isotropic cosmological models without singularity,"* Phys. Lett. **91B**, 99 (1980). 1, 2, 11, 14, 21

[126] A. A. Starobinsky, *"Disappearing cosmological constant in f(R) gravity,"* JETP Lett. **86**, 157 (2007). [arXiv:0706.2041 [astro-ph]] 1, 2, 16, 25, 49, 89, 126

[127] K. S. Stelle, *"Renormalization of higher-derivative quantum gravity,"* Phys. Rev. D **16**, 953 (1977). 11

[128] T. Tamaki and S. Tsujikawa, *"Revisiting chameleon gravity - thin-shells and no-shells with appropriate boundary conditions,"* Phys. Rev. D **78**, 084028 (2008). [arXiv:0808.2284 [gr-qc]] 37

[129] R. C. Tolman, *"Effect of Inhomogeneity on Cosmological Models,"* Proc. Natl. Acad. Sci. U.S.A. **20**, 169 (1934). Reprint: Gen. Relativ. Gravit. **29**, 935 (1997). 83

[130] S. Tsujikawa, *"Observational signatures of f(R) dark energy models that satisfy cosmological and local gravity constraints,"* Phys. Rev. D **77**, 023507 (2008). [arXiv:0709.1391 [astro-ph]] 49, 55

[131] S. Tsujikawa, T. Tamaki, and R. Tavakol, *"Chameleon scalar fields in relativistic gravitational backgrounds,"* J. Cosmol. Astropart. Phys. **05** (2009) 020. [arXiv:0901.3226 [gr-qc]] 37

[132] R. Utiyama and B. S. Dewitt, *"Renormalization of a Classical Gravitational Field Interacting with Quantized Matter Fields,"* J. Math. Phys. **3**, 608 (1962). 11

[133] M. A. Vasiliev, *"Consistent equation for interacting gauge fields of all spins in (3+1)-dimensions,"* Phys. Lett. **243B**, 378 (1990). 8

[134] A. Vilenkin, *"Classical and quantum cosmology of the Starobinsky inflationary model,"* Phys. Rev. D **32**, 2511 (1985). 14

[135] R. V. Wagoner, *"Scalar-tensor theory and gravitational waves,"* Phys. Rev. D **1**, 3209 (1970). 1, 9

[136] J. Wainwright and A. Krasinski, *"Republication of: Geometrical theorems on Einsteins cosmological equations (By E. Kasner),"* Gen. Relativ. Gravit. **40**, 865 (2008). 84

[137] R. M. Wald, *General Relativity* (The University of Chicago Press, Chicago, U.S.A., 1984). 122

[138] S. Weinberg, *Gravitation and Cosmology: Principles and Applications of the General Theory of Relativity* (John Wiley & Sons, Inc. New York · London · Sydney · Toronto, 1972). 62, 63

[139] S. Weinberg, *"The cosmological constant problem,"* Rev. Mod. Phys. **61**, 1 (1989). 20

[140] S. Weinberg, *"Effective field theory, past and future,"* PoS **CD09**, 001 (2009) [arXiv:0908.1964 [hep-th]] 19

[141] S. Weinberg, *"Asymptotically safe inflation,"* Phys. Rev. D **81**, 083535 (2010). [arXiv:0911.3165 [hep-th]] 19

[142] R. Ruffini and J. A. Wheeler, *"Introducing the black hole,"* Phys. Today **24**, No. 1, 30 (1971). 2, 83

[143] C. M. Will, *Theory and experiment in gravitational physics*, revised ed. (Cambridge University Press, Cambridge, UK, 1993). 62, 63

[144] C. M. Will, *"The Confrontation between General Relativity and Experiment," Living Rev. Relativity* **9**, 3 (2006). [arXiv:gr-qc/0510072] 60, 63

[145] P.-J. Zhang, *"The behavior of f(R) gravity in the solar system, galaxies and clusters,"* Phys. Rev. D **76**, 024007 (2007). [arXiv:astro-ph/0701662] 63

[146] J. Zinn-Justin, *Quantum Field Theory and Critical Phenomena*, (Clarendon Press, Oxford, UK, 2002). 4th ed. 19

[147] http://wwwf.imperial.ac.uk/metric/metric_public/differential_equations/second_order/qualitative_methods_1.html 59